

Coronal dynamics driven by magnetic flux emergence

Dissertation

zur Erlangung des mathematisch-naturwissenschaftlichen Doktorgrades

“Doctor rerum naturalium”

der Georg-August-Universität Göttingen

im Promotionsprogramm PROPHYS

der Georg-August University School of Science (GAUSS)

vorgelegt von

Feng Chen

aus Shandong, China

Göttingen, 2015

Betreuungsausschuss

Prof. Dr. Hardi Peter

Max-Planck-Institut für Sonnensystemforschung, Göttingen, Germany

Prof. Dr. Ansgar Reiners

Institut für Astrophysik, Georg-August-Universität Göttingen, Germany

Prof. Dr. Manfred Schüssler

Max-Planck-Institut für Sonnensystemforschung, Göttingen, Germany

Mitglieder der Prüfungskommission

Referent: Prof. Dr. Hardi Peter

Max-Planck-Institut für Sonnensystemforschung, Göttingen, Germany

Korreferent: Prof. Dr. Ansgar Reiners

Institut für Astrophysik, Georg-August-Universität Göttingen, Germany

Weitere Mitglieder der Prüfungskommission:

Prof. Dr. Stefan Dreizler

Institut für Astrophysik, Georg-August-Universität Göttingen, Germany

Prof. Dr. Wolfgang Glatzel

Institut für Astrophysik, Georg-August-Universität Göttingen, Germany

Prof. Dr. Jens Niemeyer

Institut für Astrophysik, Georg-August-Universität Göttingen, Germany

Prof. Dr. Manfred Schüssler

Max-Planck-Institut für Sonnensystemforschung, Göttingen, Germany

Tag der mündlichen Prüfung: 03. Juni 2015

Contents

Abstract	7
1 Introduction	9
2 Modelling the corona: from scaling laws to realistic 3D models	17
2.1 Basics of magnetohydrodynamics	17
2.2 Coronal energy balance	20
2.3 Concept of coronal loops	21
2.4 Scaling laws	23
2.5 One dimensional loop models	26
2.6 Three dimensional models	27
2.6.1 Reduced MHD models of coronal loops	28
2.6.2 Magneto-frictional models of active regions	28
2.6.3 Realistic active region models	28
2.6.3.1 Models with parametrised heating	29
2.6.3.2 Models accounting for magnetic braidings	30
2.7 Formation of active regions through the magnetic flux emergence	33
2.8 Motivation and aim of this study	34
3 Coronal simulations driven through the bottom boundary	37
3.1 Numerical method	37
3.1.1 Governing equations	37
3.1.2 Time step constraint	39
3.1.3 Sub-cycle for the heat conduction	40
3.1.4 Super time stepping in the sub-cycle	40
3.2 Model setup	42
3.2.1 The flux emergence simulation	42
3.2.2 Setup of the coronal model	44
3.2.2.1 Computation domain	44
3.2.2.2 Initial conditions	44
3.2.2.3 Boundary conditions	45
3.2.3 Coupling of the flux emergence and corona model	45
3.2.3.1 Preparing the vector potential	46
3.2.3.2 Time dependent update	47

4	Coronal loops formed in an emerging solar active region	51
4.1	Introduction	51
4.2	Coronal loops appearing in an emerging active region	51
4.2.1	Magnetic expansion into the corona	51
4.2.2	Appearance of a coronal loop	53
4.3	The 3D loop collapsed to one dimension	55
4.3.1	Thermal structure and dynamics of the loop	55
4.3.2	Energetics in the emerging loop	57
4.3.2.1	Initiation phase	58
4.3.2.2	Formation phase	58
4.3.2.3	Cooling phase	60
4.3.2.4	Perpendicular compression	61
4.4	The 3D nature of the loop	62
4.4.1	Evolution of the magnetic envelope	62
4.4.2	Fragmentation of the loop	63
4.5	What triggers the loop formation?	65
4.6	Summary	69
5	Relation of EUV loops to magnetic field lines	71
5.1	Introduction	71
5.2	Following (a bundle of) magnetic field lines and an EUV loop in time	73
5.2.1	Axis of a magnetic tube	73
5.2.2	Axis of an EUV loop	74
5.2.3	Evolution of the EUV loop and fieldlines	74
5.3	Thermal evolution and coronal emission along individual fieldlines	76
5.3.1	Heat input for individual fieldlines	76
5.3.2	Hot spot of Energy input	77
5.3.2.1	Magnetic braiding in the photosphere	78
5.3.2.2	Hot spot at the coronal base	79
5.3.3	Temperature and density along individual fieldlines	80
5.3.4	EUV emission along individual fieldlines	82
5.3.5	Magnetic fieldlines moving through stationary EUV loop	83
5.3.6	Summary of the mechanism	84
5.4	Conclusions	85
6	Oscillation of the coronal loop in a realistic coronal model	87
6.1	Introduction	87
6.2	Oscillation in the synthetic observation	89
6.2.1	Trigger of the oscillation	89
6.2.2	Synthetic spectral and the sit-and-stare observation	90
6.2.3	Measurement of the transverse loop oscillation	91
6.3	Estimate of the magnetic field strength	94
6.4	Comparison with the actual magnetic field strength	95
6.5	Discussion and summary	96
7	Summary and outlook	99

Bibliography	103
Acknowledgements	109
Publications	111
Curriculum vitae	113

Abstract

The corona is the Sun's outer atmosphere which is more than 100 times hotter than the solar surface. It can be brilliantly observed in the extreme-ultraviolet (EUV) and soft X-ray passbands. What heats the corona is one of the fundamental questions in solar and plasma physics. The answer must address the origin of the energy input into the corona and how the observed coronal features form and evolve as the consequence of the energy input.

To understand the built-up of the corona during the formation of the active region through magnetic flux emergence in the photosphere, we use the output of a magnetic flux emergence simulation to drive a magnetohydrodynamics (MHD) simulation for the corona. The braiding of magnetic fieldlines in the photosphere induces currents in the corona. The Ohmic dissipation of the induced currents heats the coronal plasma to over 1 MK. The proper treatment on the energy balance, as in the real corona, allows the model to synthesise EUV emission directly comparable to observations.

In the coronal model numerous bright coronal EUV loops form during the formation of a sunspot pair in the model photosphere. The coronal loops are rooted at the outer edge of the sunspots, where an enhanced upward Poynting flux is produced by the interaction of flows and magnetic field structures. The thermal dynamics and energetics of the plasma in individual magnetic fieldlines are consistent with the expectation of traditional one dimensional loop models with prescribed heat input.

At each instance of time, EUV loops are along magnetic field lines. However, their temporal evolution can be radically different, because the EUV emission is governed by the convolution of the temperature and density of the coronal plasma. When the footpoints of emerging magnetic fieldlines consecutively move through a spot of enhanced energy input at the outer edge of the sunspot, an apparently static EUV structure is created by the plasma in the emerging magnetic fieldlines. This gives an essentially new view on the relation of EUV loops to magnetic fieldlines.

Moreover, transverse oscillations of coronal loops triggered in the model can be clearly identified in synthetic observations. For observations of the Sun, the technique of coronal seismology is used to deduce the physical properties in an oscillating loop. We apply the same technique to our synthetic data to derive the average field strength in the loop and compare it to the actual value in the simulation. It is close to the average field strength that would give an identical total wave travel time through the coronal loop. This result can serve as a benchmark for coronal seismology.

The results in this thesis shed new light on dynamics during the built-up of coronal loop structures in response to the emergence of magnetic flux in the photosphere. This model highlights the power of realistic three dimensional models to resemble features in the real corona. It also emphasises the essential necessity of treating the plasma and the magnetic field at the same time, in order to self-consistently model dynamics of the coronal plasma.

1 Introduction

The corona is the outer atmosphere of the Sun. The name "corona" actually refers to the crown of the Sun. Having a brightness in the visible light similar to that of the full Moon, it is still too faint compared to the glaring disk of the Sun. But in a total solar eclipse, when the light from the disk of the Sun is shaded by the Moon, the corona is visible by the naked eyes, as a halo around the Sun. An example of the brightness and shape of the corona in a total solar eclipse is shown in Fig. 1.1. The sky lit by the corona is so dark that Mercury and Venus are clearly visible nearby the Sun.

The most mysterious nature of the corona is that it is extremely hot, more than 100 times hotter than the surface of the Sun. The first hint on the temperature of the corona comes from the spectral lines (e.g. the "green line" at 5030 Å and the "red line" at 6374 Å) that was observed since the solar eclipse in 1869. These spectral lines could not be understood until Grotrian (1939) and Edlén (1943) identified them as the forbidden lines from highly ionized ion, which are Fe ix for the "red line" and Fe xiv for the "green line". Although from present point of view, this is a very direct evidence of the high temperature of the corona, neither Grotrian nor Edlén gave a clear statement about the temperature of the corona. Alfvén (1941) first argued that the corona is hot (Peter and Dwivedi 2014).

Modern models has been able to draw a much clearer picture on the stratifications of the solar atmosphere, as shown in Fig. 1.2. The corona is filled with tenuous plasma (density $< 10^{-12} \text{ kg m}^{-3}$) that is million-degree hot. The corona is connected with the lower atmosphere, i.e. the photosphere and the chromosphere, by the transition region that is suggested to have thickness of only a few hundred kilometres (Mariska 1992). In the transition region, the temperature steeply rises by more than one order of magnitude, and the density also drops significantly because the pressure need to be continuous in general. Therefore, the transition region separates two worlds with extremely different thermal properties: the hot and tenuous corona, and the cool and relatively dense chromosphere. The transition region is usually consider as the base of the corona.

In such a hot and tenuous coronal environment, hydrogen, the richest element in the solar atmosphere, is fully ionized. Heavier elements, for example the iron, are also highly ionized. They give rise to emission in the extreme-ultraviolet (EUV) passband. Meanwhile the solar surface does not contribute any EUV emission. Therefore, space-based EUV imaging telescopes and spectrometers become the best way to observe the corona and the only way for the corona in the solar disk.

The imaging telescopes use filters to collect the photon at a particular range of wavelength that covers a target emission line. An EUV emission line is mainly contributed by plasma at a characteristic temperature, which is referred as its formation temperature. Thus the observation by a certain filter can samples the plasma at the formation temperature of the target line. For instance, the 171 Å filter used by several telescopes samples the



© Feng Chen

Figure 1.1: A photo taken at the moment of a total solar eclipse in 2008, at Jiuquan/Gansu, China. Credit: Feng Chen

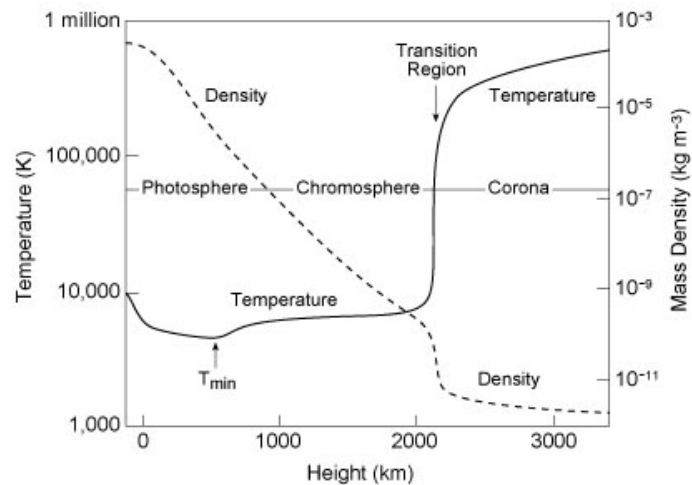


Figure 1.2: Sketch of the density and temperature profiles in height from the photosphere to the corona based on the VAL (Vernazza-Avrett-Loeser) model (Vernazza et al. 1981). Image courtesy of Eugene H. Avrett.

Fe IX line emission dominated by the plasma at a temperature *around* 1 MK (e.g. a range of 0.3 in $\log_{10} T[K]$). Spectrometers use a slit to obtain the profile of EUV spectral lines, from which we can derive the intensity, shift of the line center (the Doppler shift), and line width. The line-of-sight motions of coronal plasma can be deduced straightforward from the Doppler shift of spectral lines. The non-thermal width of a spectral line, in addition to its width determined by the thermal motions of electrons, are suggested as a clue of the stochastic motion of the coronal plasma on unresolved scales. Thus the imaging and spectroscopic observation are complementaries to each other.

The high resolution EUV images reveal an astonishing look of the corona. The corona is highly inhomogeneous. Above the quiescent Sun that covers a large area of the solar disk, the corona appears quite diffused, despite of some bright patches that are usually co-spatial with small magnetic structures in the lower atmosphere. However, the corona in active regions, which are the areas with large and strong magnetic flux concentrations, is much brighter and highly structured. In Fig. 1.3 we show an EUV image of a very common active region taken in the 171 Å channel of the Atmosphere Imaging Assembly (AIA, Lemen et al. 2012), together with the line-of-sight (LOS) magnetic field in the photosphere. The most prominent structures in the active region corona are the numerous elongated loop-like structures that arch over the solar surface (see also Fig. 2.1) and connect opposite magnetic polarities in the photosphere.

These EUV structures, known as the coronal (EUV) loops, are considered as the emission from the hot plasma confined by the magnetic fieldlines (see detailed discussions in Sect. 2.3). The EUV loops are supposed to outline the coronal magnetic field, as how the magnetic field of a magnet is visualized by iron filings.

A individual coronal loop is a relative stable structure in a time period of hours. While we can still get some impression on the dynamics of the coronal plasma by following moving patterns in a time series of EUV images. But the dynamical nature of the corona is better revealed by spectroscopic observations. As a general character over the full solar

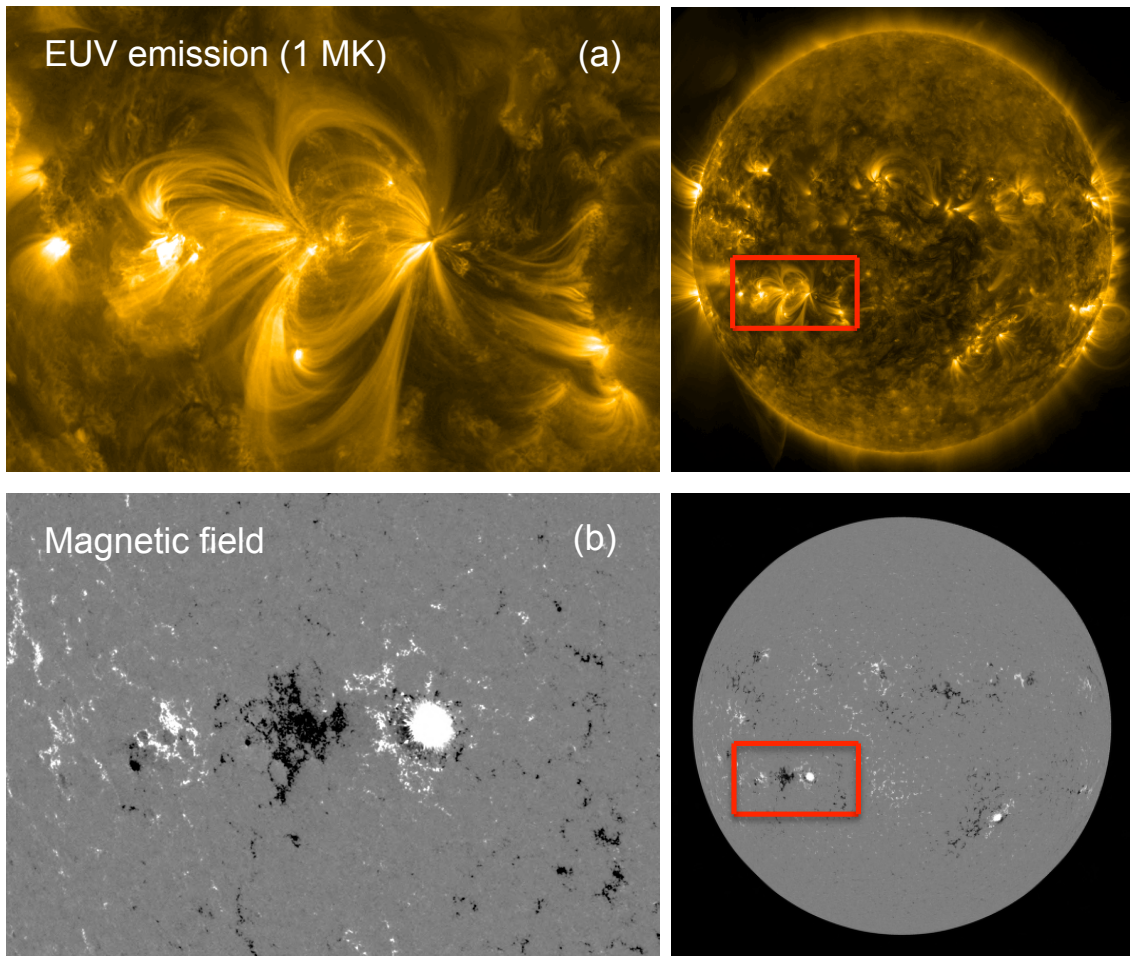


Figure 1.3: EUV loops and magnetogram in an active region on the Sun. Panel (a): An image in the AIA 171 Å channel that has mainly contribution of 1 MK hot plasma. Panel (b): The line-of-sight component of the magnetic field in the photosphere in the same field of view of (a). Right panels are the full disk EUV image and magnetogram, where the red boxes indicate the field-of-view of (a) and (b). Images are produced by the heliowviewer project. Credits: SDO (NASA)

disk, redshift is found in the spectral lines formed at transition region temperatures (i.e. of the order of 10^5 K), while the spectral lines formed at temperatures above 1 MK show blueshift. This suggests a systematic flow pattern in the transition region and the corona (Peter and Judge 1999). When zooming into an active region, a map of the Doppler velocity can capture various flow patterns in the loop system, such as the siphon flows that travel from one side of a loop to the other side, upflows that bring materials to fill the loop, and downflows showing the drainage of materials to the loop footpoints. At the outer boundary of active regions, blueshifted coronal spectral lines with a significantly enhanced non-thermal line width are observed (Doschek et al. 2008). This spectral feature is suggested to be turbulent outflows of plasma along open magnetic fieldlines, which may contribute to the solar wind.

Heating of the corona

When the high temperature of the coronal plasma is accepted as a solid truth, the question of what heats the corona rises. The fundamental energy source of the Sun is the nuclear fusions in its core. The energy is transport outwards by radiations and convective motions. Thus the average temperature is known to decrease monotonically from the core to the surface. However the outer atmosphere, i.e. the corona, is hotter than the surface.

The high temperature of corona is a mystery from the conventional point of view. In natural thermodynamic process, heat can only flow from high temperature materials to low temperature ones. The corona is at least 100 times hotter than the solar surface. Direct transport of heat from the solar surface to the corona would violate the second law of thermodynamics.

Moreover, the corona is optically thin, which means that the mean free path of photons is much larger than the spatial scale of the corona. The photons from either the corona itself or the solar surface can travel through the corona almost freely. Even though the amount of energy needed to heat the corona is only a very small portion of the total radiation flux at the solar surface, the coronal plasma can not be heated by the radiation from below.

Therefore, there must be a source of heating that balances the loss by the radiation and heat conduction, and maintains the high temperature of the coronal plasma. The heating mechanism remains a puzzle. This is known as the *coronal heating problem*. The solution must present a mechanism that is able to produce an energy budget in the corona sufficient to maintain its high temperature. More importantly, one has to describe the spatial distribution and the temporal variation of the heating, which can properly interpret the formation and evolution of the structures observed in the corona.

Present understanding on the heating mechanism

Although many attempts were made to reveal the heating mechanism of the corona, few of them were close to the success. While the debate are still ongoing, people in general agree that the energy needed to heat the corona is essentially from the lower atmosphere, and the magnetic field plays a very important role in transporting the energy from the solar surface to the corona (Schrijver and Zwaan 2000, Aschwanden 2004). The most

plausible heating mechanisms have a similar basic scenario, in which the interaction of the ubiquitous convective motions and magnetic field in the photosphere gives rise to a energy flux that is transported by the magnetic field into the corona. Eventually the Ohmic dissipation converts the (free) energy of coronal magnetic field to the internal energy of the coronal plasma.

Based on the relation of the time scale of the driving motions to the Alfvén time scale, which measures the time needed for a disturbance to propagate through a coronal magnetic fieldline, the present heating mechanisms fall into two categories, i.e. the alternative current (AC) heating and the direct current (DC) heating.

AC heating

Waves are ignited ubiquitously in the lower solar atmosphere by the interaction of granular motions and the magnetic field. The upward propagating waves, albeit partly reflected at the transition region, are still expected to take a significant amount energy into the corona. The energy flux of the waves are converted into the internal energy of the coronal plasma by the Ohmic dissipation of the currents induced by the magnetic disturbances of the waves. These currents change their directions on a time scale smaller than the Alfvén time scale in a magnetic fieldline. Therefore this type of heating is referred as the *alternative current* heating.

One of the difficulties for the AC heating was that in classical theories the Alfvén wave is very non-dissipative. This led to a problem that even though enough waves energy flux may enter the corona, few is converted to the internal energy of the coronal plasma. The phase mixing (Heyvaerts and Priest 1983) and resonance absorption (Ionson 1978) effect, which allow the wave to convert their energy more efficiently, are considered as the likely ways to cope with this problem.

The presence of the ubiquitous waves were confirm by a large scale spectroscopic observation on the corona at the solar limb (Tomczyk et al. 2007). While this observation found that the wave energy flux is not yet enough to heat the corona. However, the waves in smaller scales may still contribution a significant energy flux. Theoretical works on the wave excitation, propagating and dissipation in a magnetic flux tube rooted in the photosphere (van Ballegooijen et al. 2011, 2014, see also Sect. 2.6.1) showed that the Alfvénic waves are able to transport and deposit enough energy to heat the corona.

DC heating

The stochastic granular motions in the photosphere can twine the footpoints of the magnetic fieldlines or magnetic flux tubes as illustrated in Fig. 1.4. This is usually referred as magnetic fieldline braiding. The braiding gives rise to tangling of magnetic fieldlines that induces currents in the corona (Parker 1983). The time scale of the braiding is typically much longer than the Alfvén time scale, thus, the induced currents are *direct currents*. Parker (1988) further suggested that the magnetic energy can be released by reconnections between entangled magnetic fieldlines, which is known as nanoflares. The dissipation process in nanoflares can be considered as the Ohmic dissipation of the currents induced by the entangled magnetic fieldlines.

The flux tube tectonics mechanism proposed by Priest et al. (2002) is also based on

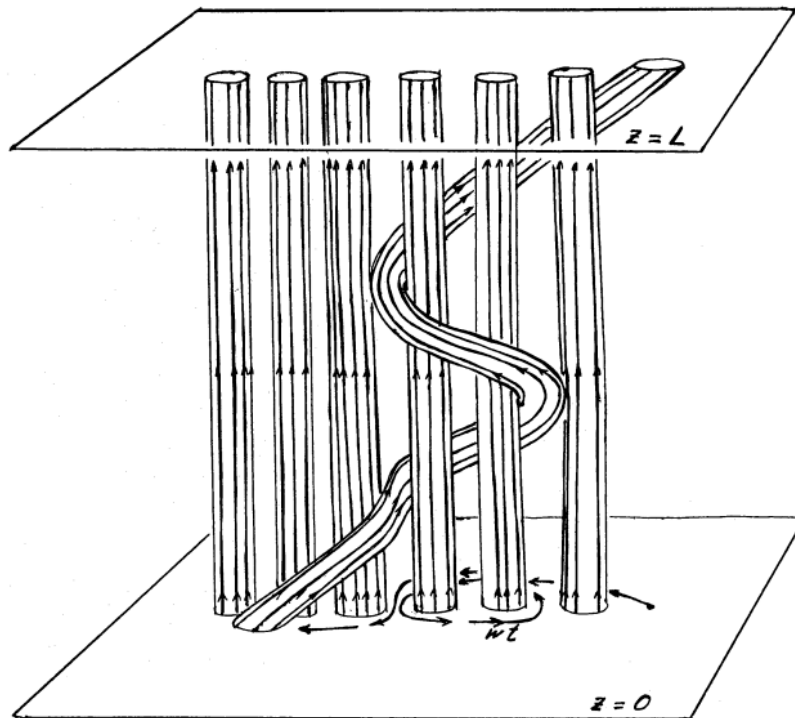


Figure 1.4: Sketch for the braiding of the magnetic field by footpoint motions. The planes $z=0$ and $z=L$ present the solar photosphere, where a group of magnetic flux tubes of a length of L are rooted. The space between the two planes is the corona. The stochastic motion in "one" photosphere (i.e. $z=0$) takes the footpoint of a flux tube and braids it around the other flux tubes. This figure is taken from Parker (1983).

magnetic braidings. They suggested that (shearing) motions in the photosphere can build magnetic separatrix surfaces in the corona, and currents are induced at these surfaces. According to the authors, the name of "flux tube tectonics" is an analogy to geophysical plate tectonics, where energy is also built up and dissipated along shape boundaries (as in the separatrix surfaces with induced currents).

A recent high resolution observation in the EUV passband found interlaced thin and bright structures near the footpoints of coronal loops (Cirtain et al. 2013). These structures are interpreted as an observational evidence of the magnetic braiding. Theoretical investigations on the energy budget provided by the braiding (e.g. van Ballegoijen 1986, Galsgaard and Nordlund 1996, Rappazzo et al. 2008) also suggest it to be a very likely mechanism to heat the corona.

Summary of the heating mechanisms

Both the AC and DC heating has been extensively studied in many observations and theoretical analysis (see Sect. 2.6.1 and Sect. 2.6.3.2). Still they remain to be the most likely candidates to solve the mystery of the coronal heating. Meanwhile new suggestions on the origin of hot plasma come out with the continuous refinements on observations

(De Pontieu et al. 2011). Finally the heating of the coronal plasma probably does not rely on a single mechanism.

People generally agree that the energy budget in the lower atmosphere is more than sufficient to heat corona, and the magnetic fieldlines is the important agent responsible for the transport and dissipation of the energy. While the dissipation process, which determines the conversion rate of the magnetic energy to the internal energy of the coronal plasma, remains not fully clear.

The distribution and variation of the heat input in the corona eventually drive the formation of coronal structures and dynamics. Conversely, Investigations on the response of the corona to the heating can give us constraints and clues on the heat deposition in the real corona. Great efforts have been made on building coronal models, in which the heat input is either given by (semi)empirical parametrisation, or self-consistently produced based on certain mechanisms (e.g. braiding or waves), as introduced in the next chapter.

2 Modelling the corona: from scaling laws to realistic 3D models

2.1 Basics of magnetohydrodynamics

Magnetohydrodynamics (MHD) is a general tool to study the dynamics of the magnetized fluid, such as the plasma in the solar atmosphere. Detailed introduction on the MHD theory and its validity in the solar atmosphere are available in some classical text books (e.g. Priest 2014). Here, we briefly describe the equations governing the evolution of the coronal plasma.

MHD equations

MHD equations consider the basic conservation laws for mass, momentum and energy. The form of the MHD equations would depend on the choice of primary variables and physical ingredients in a model.

By choosing ρ the density, \mathbf{u} the velocity, \mathbf{B} the magnetic field, and e_{th} the thermal energy density, the equations governing the evolution of resistive plasma can be written as

$$\frac{\partial \rho}{\partial t} + \nabla \cdot (\rho \mathbf{u}) = 0, \quad (2.1)$$

$$\frac{\partial \mathbf{u}}{\partial t} + (\mathbf{u} \cdot \nabla) \mathbf{u} = \frac{1}{\rho} \left[-\nabla p + \rho \mathbf{g} + \mathbf{j} \times \mathbf{B} + \nabla \cdot \underline{\underline{\tau}} \right], \quad (2.2)$$

$$\frac{\partial \mathbf{B}}{\partial t} = \nabla \times (\mathbf{u} \times \mathbf{B}) - \nabla \times (\eta \nabla \times \mathbf{B}), \quad (2.3)$$

$$\frac{\partial e_{\text{th}}}{\partial t} + (\mathbf{u} \cdot \nabla) e_{\text{th}} = -\frac{\gamma}{\gamma - 1} p (\nabla \cdot \mathbf{u}) + H - L_{\text{rad}} - \nabla \cdot \mathbf{q}. \quad (2.4)$$

Here p is pressure and \mathbf{j} the current that is related to \mathbf{B} by $\mu_0 \mathbf{j} = \nabla \times \mathbf{B}$, where μ_0 is the vacuum permeability. \mathbf{g} is the gravitational acceleration, τ the viscous stress tensor, η the resistivity, γ the adiabatic index (or heat capacity ratio), H the volumetric heating rate, L_{rad} the radiative loss (rate), and \mathbf{q} the heat conduction flux.

The continuity equation (Eq. (2.1)) reflects that the mass of a plasma parcel is a constant, because there is no mass generation or annihilation. The equation of motion (Eq. (2.2)) describes the change of the velocity of a plasma parcel by external forces including the pressure gradient, the Lorentz force, the viscous force and the gravity. The energy equation (Eq. (2.4)) accounts for the change of the thermal energy due to mechanical works, heat conduction, as well as direct heatings and the loss through radiation.

Assuming η to be a constant in space, the induction equation (Eq. (2.3)) can be rewritten as

$$\frac{\partial \mathbf{B}}{\partial t} = \nabla \times (\mathbf{u} \times \mathbf{B}) + \eta \nabla^2 \mathbf{B}. \quad (2.5)$$

The first term on the right hand side is the induction of magnetic field, while the second term is the diffusion of magnetic field due to a non-vanishing resistivity of the coronal plasma.

Finally the equations above are closed by the equation of state. For an ideal polytropic gas, the equation of state is written as

$$p = \frac{\rho}{\tilde{\mu} m_p} k_B T, \quad (2.6)$$

where k_B is the Boltzmann constant, m_p the proton mass, and $\tilde{\mu}$ mean atomic weight (e.g. unity fully neutral hydrogen and 0.5 for fully ionized hydrogen).

Magnetic energy and the Poynting flux

The energy density of a magnetic field is evaluated by

$$e_{\text{mag}} = \frac{B^2}{2\mu_0}.$$

Its temporal evolution can be obtained by the dot product of \mathbf{B}/μ_0 to both sides of Eq. (2.3), which leads to

$$\frac{\partial e_{\text{mag}}}{\partial t} + \nabla \cdot \mathbf{S} = -\mathbf{u} \cdot (\mathbf{j} \times \mathbf{B}) - \mu_0 \eta \mathbf{j}^2, \quad (2.7)$$

where \mathbf{S} is the Poynting flux evaluated by

$$\mathbf{S} = \eta \mathbf{j} \times \mathbf{B} - \frac{1}{\mu_0} (\mathbf{u} \times \mathbf{B}) \times \mathbf{B}. \quad (2.8)$$

The left hand side of Eq. (2.7) shows the change of the magnetic energy in a finite volume due to the flux of electromagnetic energy, i.e. the Poynting flux, at the surface of this volume.

The right hand side of Eq. (2.7) accounts for the exchange of magnetic energy with other forms of energy. The first term is the exchange with the kinetic energy through the work done by the Lorentz force (a decrease of e_{mag}) or the work done by plasma against the Lorentz force (a increase of e_{mag}). The second term evaluates the loss of magnetic energy by Ohmic dissipation, which is added to the thermal energy of the plasma. This is known as the Ohmic heating.

Alfvén's frozen-in theorem

In a perfectly conductive fluid, where the electric conductivity, $\sigma=1/(\mu_0\eta)$, is infinite, the fluid and magnetic fieldlines must move together in the direction perpendicular to the magnetic fieldlines. Therefore the magnetic fieldlines are frozen in the fluid. This is a consequence of the induction part in Eq. (2.5).

The frozen-in theorem inspires a common method in practical analysis to follow magnetic fieldlines, which are imaginary objects. A magnetic fieldline passing through a particle (a infinitely small fluid element in continuum material) will be frozen to this particle in later time. Therefore one can follow the motion of this particle and calculate the magnetic fieldline through this particle at each instant of time. This reveals the evolution of a magnetic fieldline. Similarly, one can depict the evolution of a magnetic flux tube, i.e. a bundle of magnetic fieldlines, by tracing the particles on a curve enclosing the cross section of the flux tube.

When the electric conductivity is not infinitely large, the diffusion effect allows magnetic field to move through fluid. The diffusion time scale (τ_d) for the magnetic field to diffuse through a length scale L is evaluated by

$$\tau_d = \frac{L^2}{\eta}. \quad (2.9)$$

If the diffusion time scale is much larger than the time scales of other processes in the system (e.g. most of the astrophysical objects), the frozen-in theorem can still be applied.

Plasma β

Plasma β is an important parameter in MHD. It indicates the predomination of the magnetic field or the plasma. It is commonly defined as the ratio of the gas pressure (p_{gas}) to the magnetic pressure (p_{mag}), i.e.

$$\beta = \frac{p_{\text{gas}}}{p_{\text{mag}}}, \quad (2.10)$$

where the magnetic pressure is defined as $\mathbf{B}^2 / (2\mu_0)$. From the point of view of the energy density, we can use the relations $e_{\text{th}} = p_{\text{gas}} / (\gamma - 1)$ and $e_{\text{mag}} = p_{\text{mag}}$ and rewrite β as

$$\beta = \frac{1}{\gamma - 1} \frac{e_{\text{th}}}{e_{\text{mag}}}. \quad (2.11)$$

Similarly, It can also be rewritten by definitions of the sound speed (c_s) and the Alfvén speed (v_A) as

$$\beta = \frac{2}{\gamma} \frac{c_s^2}{v_A^2}. \quad (2.12)$$

When β is below unity, the magnetic field takes the dominance. The frozen-in theorem is expressed in a way that the plasma is confined by the magnetic field. In the solar corona, where β is typically less than 10^{-2} , the plasma motion perpendicular to the magnetic field is only subject to the movement of the magnetic fieldlines. For example, the eruption of a magnetic structure will take the material confined in the magnetic field.

In contrast, when β is well above unity, plasma motions are predominately determined by the pressure gradient force. Consequently, the magnetic field frozen in the plasma has to passively follow the motion of the plasma. For instance, in the solar photosphere (not in/around strong magnetic flux concentrations) the magnetic field is passively pushed by the granular motions into the granular lanes.

2.2 Coronal energy balance

Although the evolution of the coronal plasma is governed by the full MHD equations, what essentially determines the density and temperature in a coronal model is the energy balance. The most important ingredients are the heating, radiation, and thermal conduction in Eq. (2.4).

Structures in the corona are relatively stable. Even if the heating ceases, a bright structure in the corona can still sustain for about half an hour (Klimchuk 2006). This is known as the coronal cooling time scale. Furthermore, the typical flow speed in a non-erupting active region is smaller than the coronal sound speed. Therefore, as the first step to understand the energy balance in corona structures, we can assume a hydrostatic equilibrium, i.e. the time derivatives and velocities in the MHD equations vanish. With this assumption, the energy conservation (Eq. (2.4)) reads,

$$0 = H - L_{\text{rad}} - \nabla \cdot \mathbf{q}. \quad (2.13)$$

If we integrate Eq. (2.13) over the volume of the corona and assume that the heat conduction flux vanishes at the surface of the volume, the total energy input by the heating must be balanced with the total energy loss through the radiation. While the heat conduction plays a role to redistribute the thermal energy in space.

Radiation

The energy loss through the optically thin radiation, L_{rad} , is evaluated by

$$L_{\text{rad}} = n_e^2 \Lambda(T), \quad (2.14)$$

where, n_e is the electron number density, and $\Lambda(T)$ a function of temperature (T) that accounts for the contributions from coronal emission lines (Mariska 1992). This function peaks around $T=10^5$ K, which corresponds to the temperature in the transition region. As a result of the gravity, the number density at the transition region is also considerably higher than that in the corona. Therefore the transition region, as the corona base, contributes the most optically thin radiation.

Heat conduction

Spitzer (1962) derived that the heat conduction flux in fully ionized plasma, \mathbf{q} can be written as

$$\mathbf{q} = -\kappa_0 T^{5/2} \mathbf{b} (\mathbf{b} \cdot \nabla T), \quad (2.15)$$

where $\kappa_0=1.8 \times 10^{-10} \text{ W m}^{-1} \text{ K}^{-7/2}$ is the coefficient given by Spitzer (1962), T the temperature, \mathbf{b} the unit vector of the magnetic field. The heat conduction, known as the Spitzer heat conduction, depends strongly on the temperature. At typical coronal temperatures (e.g. more than 1 MK), the Spitzer heat conduction is extremely efficient to transport thermal energy. However this characteristic put a severe challenge to numerical experiments, as discussed later in Sect. 3.1.2.

Furthermore, the heat conduction flux shown above is parallel to the magnetic field. In the solar corona the thermal conduction perpendicular to the magnetic field is weaker

than the parallel conduction by many orders of magnitude. Therefore the perpendicular heat conduction is usually neglected for studies on the corona.

Heating rate

The form of the heating rate remains unknown, until the coronal heating problem would be solved. It is the most important ingredient of the energy balance (Eq. (2.13)). When an equilibrium is established in the corona, the heat conduction must be able to transport the heat input, which consequently sets the temperature profile. Meanwhile the radiation loss must eliminate the energy brought down by the heat conduction, which sets the density at the coronal base, as well as the density profile in the corona.

In real practice of coronal modelling, the heating has to be either assumed (Sect. 2.4, Sect. 2.5 and Sect. 2.6.3.1), or produced self-consistently through proposed mechanisms (Sect. 2.6.1 and Sect. 2.6.3.2).

2.3 Concept of coronal loops

Coronal EUV loops, the thin and bright structures seen in EUV images, are the most common building blocks in the solar corona, particularly in active regions (e.g. in Fig. 1.3). They are considered to represent the hot plasma confined in coronal magnetic field. This widely accepted interpretation is based on the following characteristic physical conditions in the corona.

- *High electric conductivity*

The electric conductivity in the solar corona is sufficiently high, thus the frozen-in theorem can be well applied. This insures that the plasma can not move *across* magnetic fieldlines, while it may still move parallel to magnetic fieldlines. A magnetic flux tube can be an analogy to a water pipe, in which water (as the plasma in confined in the magnetic field) can only flow along the pipe.

- *Low plasma β*

The plasma β in the corona is usually below 10^{-2} . Therefore a magnetic flux tube is a rigid structure. The material confined in a magnetic tube has to follow the shape of the magnetic fieldlines that arch over solar surface (Fig. 2.1) and are rooted at opposite magnetic polarities on the solar surface (Fig. 1.3).

The other important implication is that a large pressure gradient can be built across magnetic fieldlines. This means that even neighbouring magnetic fieldlines may have very different density and temperature. The corresponding pressure gradient has almost no impact on the magnetic field structure.

- *Highly anisotropic heat conduction*

The heat conduction in the corona is predominantly along magnetic fieldlines. The heat transport across the magnetic fieldline is very inefficient compared to the parallel transport. Therefore a coronal magnetic flux tube can be considered as an adiabatic pipe that has no heat exchange with its neighbours.

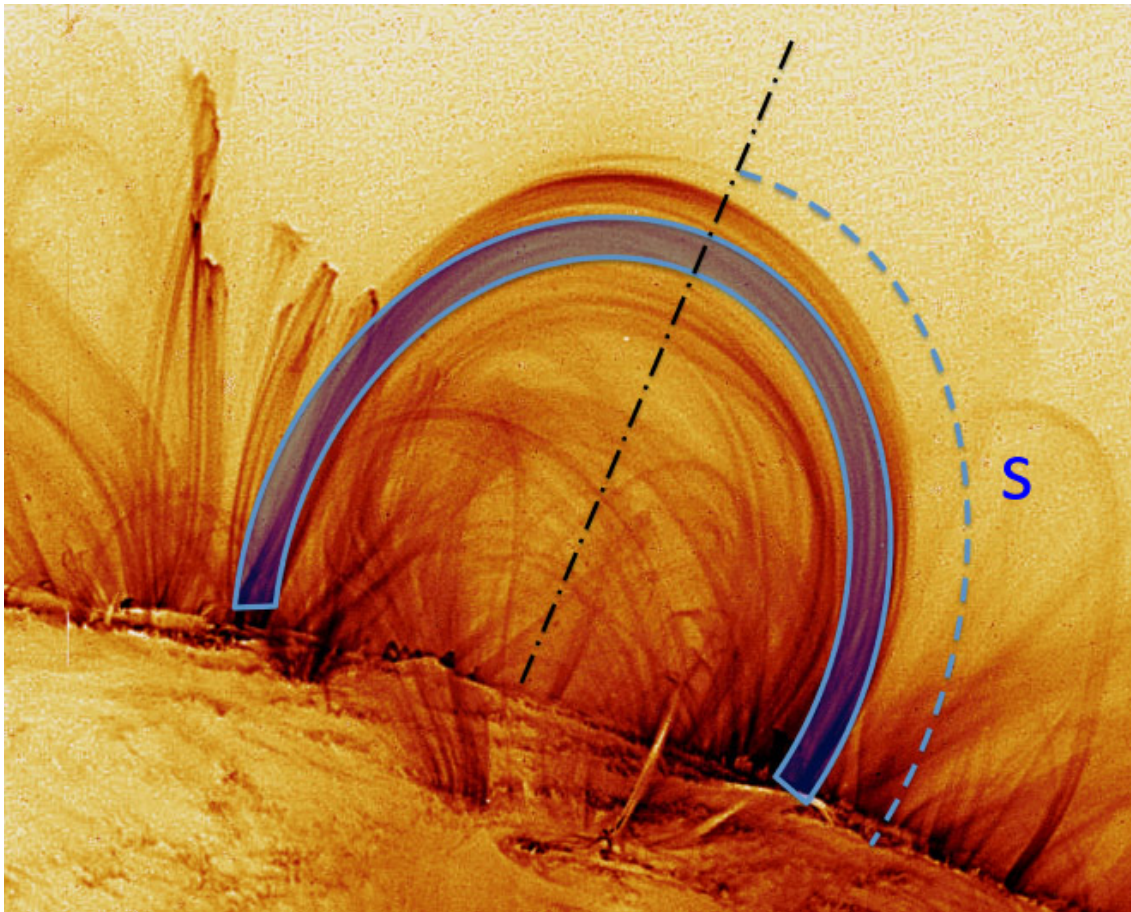


Figure 2.1: Illustration of a coronal loop model. The background is an EUV image in the 171 \AA channel of Transition Region And Coronal Explorer (TRACE) sampling emission from 1 MK hot plasma. It shows numerous coronal loops arching over the solar surface. The arched blue band illustrates a loop model with a uniform cross section. S is the coordinate along the loop. Figure is taken from Reale (2014). Background image is from TRACE, credit: NASA/LMSAL.

In together, a magnetic flux tube in the corona can be treated as a rigid and adiabatic pipe. The density and temperature of the hosted plasma are almost only determined by the thermal dynamics along the pipe. This leads to the term "coronal loop". A coronal loop refers to a *coronal magnetic loop* that hosts a *coronal plasma loop*, which appears as a *coronal EUV loop* in observations.

Coronal loops are the most important object in a coronal model. The concept of coronal loops was widely used to construct of analytical models (Sect. 2.4) or one/three dimensional numerical models (Sect. 2.5 and Sect. 2.6.1). In Fig. 2.1 we show an illustration of the one dimension loop models. These model solve a hydrodynamic problem in a coordination (S in Fig. 2.1) along magnetic fieldlines in the corona.

Models enclosing a full active region (Sect. 2.6.2 and Sect. 2.6.3) must still demonstrate how coronal loops are formed in the model. Fig. 2.2 shows an example of 3D active region models in which a coronal loop is self-consistently formed (see the model strategy in Sect. 2.6.3 and Sect. 3.2). In Fig. 2.2 the magnetic flux tube outlined by group of mag-

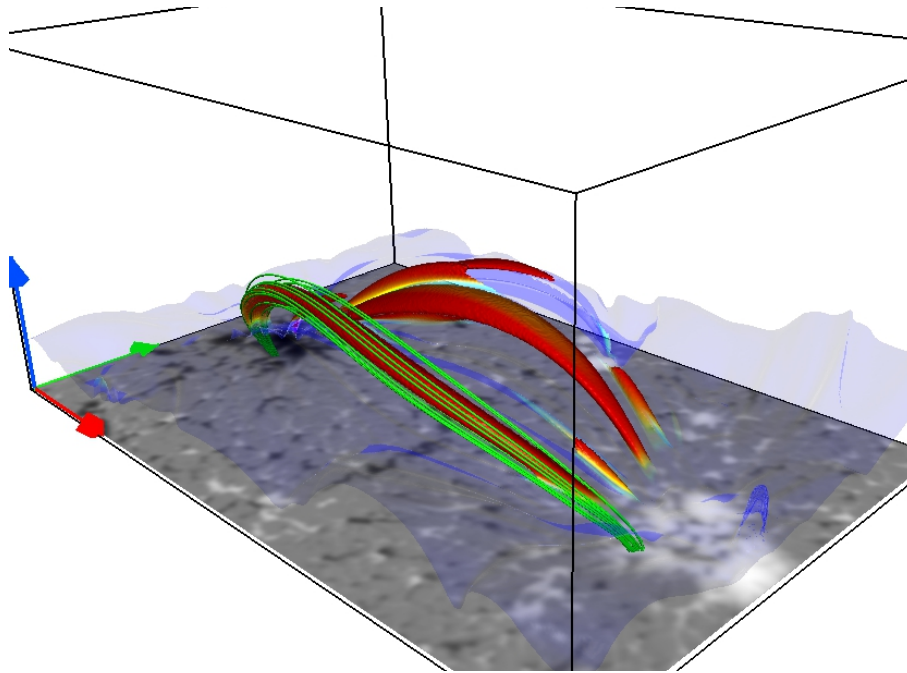


Figure 2.2: A coronal loop identified in a 3D active region model. The image at the bottom (corresponding to the photosphere) shows the vertical magnetic field. Blue surface is for the temperature of 10^5 K, which represents the transition region, i.e. the coronal base. Red surface, showing loop filled with plasma, is for the number density of 10^9 cm^{-3} . Green lines are the magnetic fieldlines that host the plasma loop. The domain is part of a 3D simulation (Sect. 3.2.2: *high resolution run*). The distance between the two sunspots is about 40 Mm. The visualization is produced by VAPOR.

netic fieldlines connects two sunspots in the photosphere and hosts hot coronal plasma of a density of 10^9 cm^{-3} , as usually observed on the Sun.

2.4 Scaling laws

Scaling laws show the general relations of the fundamental parameters of the corona, such as its length scale, heat input, density, temperature. The scaling laws derived by Rosner, Tucker, and Vaiana (Rosner et al. 1978, hereafter RTV), which is based on the coronal energy balance in a hydrostatic equilibrium (Eq. (2.13)), has been extensively exploited to understand the basic features of the corona.

The basic assumption includes that

- the loop (as a thin magnetic tube) has a uniform cross section,
- the temperature peaks at the loop apex, and the temperature gradient vanishes at the apex,
- the density is uniform, which is validated by the large density scale height at coronal temperatures,

- the volumetric heat rate is a constant.

The corresponding energy balance for this constant cross-section loop (magnetic tube) can be written as

$$0 = H_0 - n_e^2 \Lambda(T) + \frac{d}{ds} \left(\kappa_0 T^{5/2} \frac{dT}{ds} \right), \quad (2.16)$$

where s is the coordinate along the loop, and H_0 the constant heating rate.

We can derive the scaling relations of the density and temperature to the heat input in an more simplified scenario. Given that the transition region contribute the most radiative loss (Sect. 2.2), we further assume that the radiation is negligible in the majority of the coronal loop, and concentrated at the footpoint (at the coronal base). This implies that the heat input is balanced by the heat conduction in the loop part above its footpoint. While at the footpoint of the loop, the radiation is equal to the heat conduction. The amount of the energy transferred by the heat conduction to the footpoint is exactly the total heat deposited in the loop.

Relation of the temperature to the heating rate

Above the loop footpoint, the volumetric heating rate is balanced by the heat conduction. The integral of the energy balance from a position s in the loop to the loop apex is written as

$$\int_s^L H_0 ds' = - \int_s^L d \left[\kappa_0 T^{5/2}(s') \frac{dT(s')}{ds'} \right], \quad (2.17)$$

where L is the half length of the loop. The integral yields

$$H_0(L - s) = - \left[\kappa_0 T^{5/2}(s') \frac{dT(s')}{ds'} \right] \Big|_{s'=s}^{s'=L}. \quad (2.18)$$

By the boundary condition that the gradient of temperature vanishes at the loop apex, we obtain

$$H_0(L - s) = \kappa_0 T^{5/2}(s) \frac{dT(s)}{ds}. \quad (2.19)$$

We integrate Eq. (2.19) along the loop and obtain

$$\frac{H_0 L^2}{2} = \frac{2\kappa_0}{7} T^{7/2}(s) \Big|_{s=0}^{s=L}. \quad (2.20)$$

The temperature at the loop footpoint, $T(0)$, is much smaller than that at the apex, i.e. the peak temperature (T_{\max}) of the loop. Therefore, by neglecting $T(0)$, the scaling relation of the peak temperature to the heating rate and the loop length is

$$T_{\max} \propto H_0^{2/7} L^{4/7}. \quad (2.21)$$

Relation of the density to the heating rate

At the footpoint of the loop, the radiative loss is balanced mostly by the heat conduction that transports the heat deposited in the loop to the footpoint, while the local heating can be neglected. The energy balance is written as

$$n_e^2 \lambda T^{-1/2} = - \frac{dq}{ds}, \quad (2.22)$$

where the contribution function for the radiative loss, $\Lambda(T)$, can be approximated by $\lambda T^{-1/2}$, and q is the heat conduction flux. We multiply $\kappa_0 T^{5/2}$ to this equation and obtain

$$\kappa_0 \lambda n_e^2 T^2 = -\kappa_0 T^{5/2} \frac{dT}{ds} \frac{dq}{dT} = \frac{1}{2} \frac{dq^2}{dT}. \quad (2.23)$$

The integral of Eq. (2.23) over the temperature reads

$$\frac{2\kappa_0 \lambda}{3} n_e^2 [T^3(L) - T^3(0)] = q^2(L) - q^2(0). \quad (2.24)$$

The heat conduction flux at the apex, $q(L)$, is zero, because the gradient of temperature vanishes at the loop apex. The apex temperature, $T(L)$, is T_{\max} . From these conditions, we obtain

$$\sqrt{\frac{2\kappa_0 \lambda}{3}} n_e T_{\max}^{3/2} = -q(0), \quad (2.25)$$

which gives the relation of the density to the heat conduction flux at the coronal base. From Eq. (2.19), we can derive

$$q(0) = \left[-\kappa_0 T^{5/2}(s) \frac{dT(s)}{ds} \right]_{s=0} = -H_0 L, \quad (2.26)$$

which is consistent with the concept that the heat conduction transfers all the heat input in the loop to the footpoint. By substituting $q(0)$ into Eq. (2.25), the density can be related to H_0 by

$$n_e T_{\max}^{3/2} \propto H_0 L. \quad (2.27)$$

We can use Eq. (2.21) to eliminate T and obtain

$$n_e \propto H_0^{4/7} L^{1/7}. \quad (2.28)$$

Implications of the scaling laws

First of all, the scaling laws show that for a given loop (i.e. a fixed L) the peak temperature and the density in the loop increase with the volumetric heat rate. This can be understood by putting an extra heating into an equilibrium loop. The heat conduction has to increase to transport the extra heat, which leads to a larger temperature gradient along the loop and a higher peak temperature. The radiation also has to increase to balance the extra energy input, which leads to a higher density at the base. Together with the larger density scale high, the whole loop gets a higher density when a new equilibrium is established.

Furthermore, the scaling relation for the temperature shows that the peak temperature only *weakly* depends on the heating rate. For example, when the heating rate is enhanced by an order of magnitude, the peak temperature only increases by about a factor of 2. In comparison, the density, as well as the coronal emission, has a stronger dependency on the heating rate. Thus the most important issue in coronal heating problem is actually not to sustain a high temperature, but to sustain a proper density that can produce the correct amount of emission at the coronal temperatures.

For a fixed heating rate, one may get an impression from Eq. (2.21) and Eq. (2.28) that longer loops have a higher temperature and density than shorter loops for the same amount

of heat input. However, it is not true. This can be better understood if we consider the energy input flux, F_H , which is defined in general as

$$F_H(s) = \frac{1}{A(s)} \int_s^L H(s) A(s) ds, \quad (2.29)$$

where A is the area of the cross section of the loop. This definition shows that the total heat input in the volume of the loop comes from an energy flux (e.g. produced by waves or magnetic braidings) that goes through the base of the loop. The increase in either the volumetric heating rate or in the volume (i.e. length) of the loop would require a higher energy flux through the base (assuming the base area unchanged). In the case considered by the RTV scaling laws, the energy flux through the loop base is evaluated by

$$F_H(0) = H_0 L.$$

Therefore, Eq. (2.21) and Eq. (2.28) are rewritten as,

$$T_{\max} \propto F_H^{2/7}(0) L^{-2/7}, \quad (2.30)$$

$$n_e \propto F_H^{4/7}(0) L^{-3/7}. \quad (2.31)$$

It is clear that longer loops would have lower peak temperature and density for a given energy flux into the loop, because the energy flux has to be distributed in a larger volume, which means that the volumetric heating rate would decrease.

2.5 One dimensional loop models

One dimensional (1D) loop models have a similar base as the scaling laws. They also consider a 1D structure that is shaped by the magnetic field (as in Fig. 2.1). However, 1D loop models are usually beyond the regime of hydrostatic equilibrium. A typical 1D loop model numerically solves the full hydrodynamic problem, i.e. the conservations of mass, momentum and energy, in a coordinate along the magnetic fieldline. The magnetic field usually does not explicitly play a role. While the area of the loop cross-section, which is related to the inverse of the magnetic field strength along the loop, can be included 1D models.

Although 1D loop models seem to have a rather simple setup, it has many clear advantages. A few of them are summarised as the following.

- 1D model is the most simple model that can give the distributions of the plasma properties (and velocities for non-static solutions) along the loop. In contrast the scaling laws only consider the peak temperature and a characteristic density.
- 1D loop models can solve a time-dependent problem, which allows people to study the evolution of the density, temperature and velocity in the loop. This stimulates comparisons with the temporal evolution observed on the Sun.
- When solved numerically, 1D loop models can achieve high resolutions with a more affordable computational demand, compared to multi dimensional models. Actually even with the computation power at nowadays, only 1D loop models are able to use a grid spacing that resolves the steep temperature gradient in the transition region well.

Therefore 1D models was the most popular modelling approach on corona dynamics in the last three decades. They were used to study the flow patterns that are driven by various distributions of the heating rate and different geometries of the loop (Boris and Mariska 1982, Mariska and Boris 1983). Hansteen (1993) studied the response of the loop plasma to an episodic heating that would be given by nanoflares (Parker 1988). These models properly treated the corona energy balance, albeit with a prescribed heating rate, and were able to produce synthetic spectra that are comparable to actual spectroscopic observations. They found interpretations to the systematic red shift (i.e. downward motion of plasma) observed in the transition region spectral lines at that moment. Müller et al. (2003, 2004) studied the condensation of plasma in coronal loops. These models aimed to understand the dynamics in coronal rains where cool materials were observed to fall back to the solar surface. These models showed that the insufficient heating versus the energy loss at the loop apex can trigger the catastrophic cooling of the loop plasma. Recently, Mikić et al. (2013) investigated 1D loop models with non-uniform or asymmetric cross sections that are derived from a more realistic magnetic configuration. They demonstrated the impacts of cross section profile to the behaviour of the loop plasma. Numerous studies are summarized comprehensively in the up-to-date reviews by Reale (2010, 2014), which show many successes of 1D models on propelling our understandings on the structures and dynamics of coronal loops.

1D models also have shortages that can not be essentially eliminated. The most critical one is that the heating rate in a 1D model must be prescribed, because in a purely 1D setup, most of the heating mechanisms can not be modelled in a fully self-consistent manner. To self-consistently produce a heat input to a loop, the cross section of the loop has to be spatially resolved, as in 3D reduced MHD models (see details in Sect. 2.6.1).

They also have difficulties on directly modelling loops in evolving magnetic structures. One might cope with this by a collection of 1D models with different geometry setups which would depict the change of the magnetic structure. However this method still have the problem of no self-consistency.

Such problems can be handled in 3D models introduced in the next section.

2.6 Three dimensional models

The 3D nature of the corona can only be self-consistently reproduced by 3D models. Depending on the aims of the studies and availability of resources, difference models may include different ingredients. Some may focus on the characters of the heat input, thus disregard the plasma properties that probably does not impact the heat input much. While some may aim to study the dynamical response of the coronal plasma to a prescribe heating rate.

In Sect. 2.6.1 and Sect. 2.6.2 we introduce several typical simplified 3D models, which often focus on modelling one particular properties of the corona. Then Sect. 2.6.3 gives a review on more sophisticated realistic models that can give a comprehensive description on the plasma and magnetic field in the corona.

2.6.1 Reduced MHD models of coronal loops

Reduced MHD models (Strauss 1976) are 3D models for a loop structure. They assume a very strong time-independent longitudinal background magnetic field that corresponds to a magnetic flux tube. These models only solve the velocity and magnetic disturbances transverse to the background magnetic. Such setups intend to model the energy input into a loop by interactions of the velocity field and magnetic fieldlines at the footpoint of loop. The driving velocity field still has to be given empirically. These models have been used to test the energy input from the Alfvén wave turbulence (van Ballegoijen et al. 2011, 2014) and the fieldline braiding (Rappazzo et al. 2008). A reduced MHD model can produce a relation of the heating rate to the loop parameters. Such a relation can be used as a parametrisation of the heating in other models to study the coronal structure are formed in response to the heat input (Sect. 2.6.3.1).

2.6.2 Magneto-frictional models of active regions

Magneto-frictional models solve the induction equation by assuming that the velocity in the induction equation is proportional to the Lorentz force. This is motivated by the low β of the corona. The evolution of the coronal magnetic field is determined by motions perpendicular fieldlines. These motions is primarily driven by the Lorentz force. The magnetic field in the magneto-frictional models will finally relax to a force-free state, because a vanishing velocity requires a vanishing Lorentz force.

In a magneto-frictional model Cheung and DeRosa (2012) followed the evolution of a growing active region. They used a time series of observed vertical magnetic field (lower panels in Fig. 2.3) as the bottom boundary and investigated how the coronal magnetic field relaxes to a force-free state. In each individual fieldline they evaluated an artificial emission that is defined as a function of the integral of \mathbf{j}^2 along the fieldline. The synthetic images (upper panels in Fig. 2.3), obtained by integrating the emission along a chosen line-of-sight, appear similar to the actual EUV observation sampling emission from 1 MK hot plasma, as shown in Fig. 2.3. This result may suggest that the magneto-frictional models, albeit highly simplified, still provide some valuable information on the heating distribution in the active region corona. Magneto-frictional models are usually less computationally demanding (compared to Sect. 2.6.3 in the following). Thus they can model the evolution of active regions on a time scale of days and on a spatial scale of several hundred Mm, with relatively affordable computations.

2.6.3 Realistic active region models

Realistic models intend to have a more comprehensive description on the physical processes in the corona, which include at least a fully compressible MHD problem with the coronal energy balance. The model parameters are set to match with the solar corona as closely as possible. The highest Reynolds number achieved in these models has to compromise to the limit of computation powers, as what also happens to most of the numerical experiments on astrophysical plasma. Nonetheless, these models are able to produce very realistic density and temperature structures that are consistent with typical values derived from observations. One can use the density and temperature in the model to synthesise

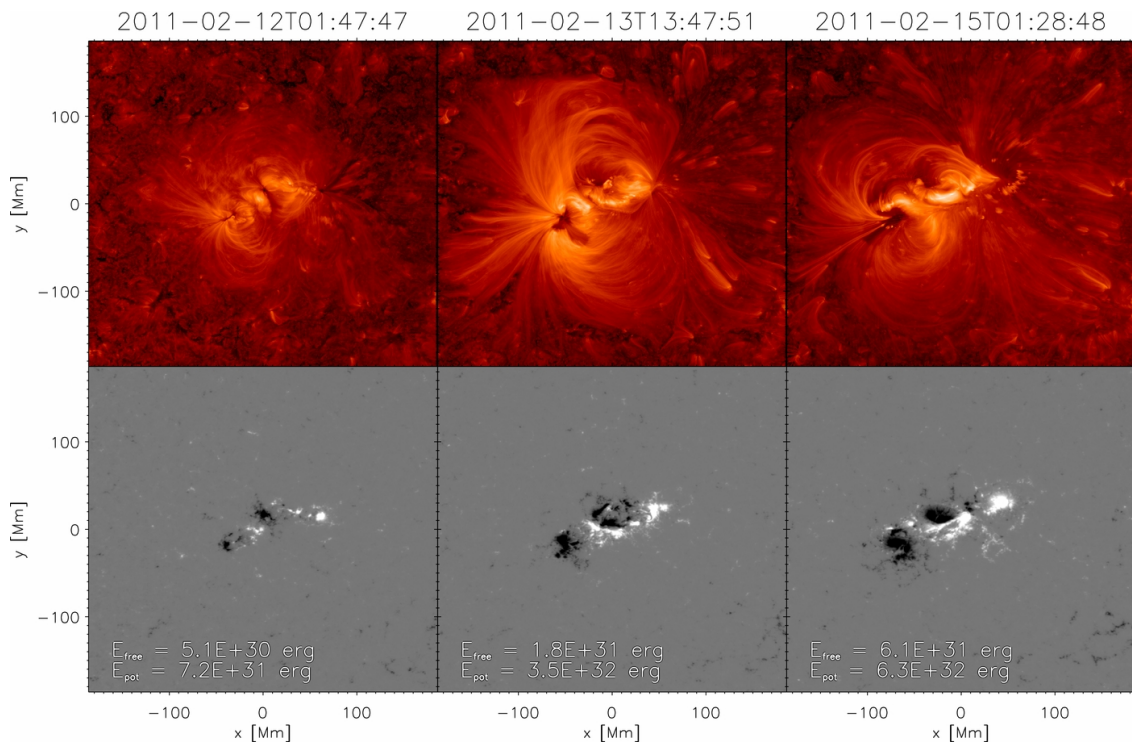


Figure 2.3: Artificial emission produced by a magneto-frictional model driven by the observed magnetic field in the photosphere. Upper panels show the artificial emission that is assumed to be related to the heating along individual fieldlines (see Sect. 2.6.2 for details). Lower panels are the observed line-of-sight magnetic field in an emerging active region, which drives the evolution of the coronal magnetic field in the magneto-frictional model. This figure is taken from Cheung and DeRosa (2012).

observations in the EUV and X-ray passbands. These synthetic observations can be directly compared with actual observations. From these comparisons, we can investigate the physical processes responsible for the consistency or inconsistency between the models and the reality. In this way, these models can shed light on the natures of the heat input, thermal properties and dynamics in the real corona.

2.6.3.1 Models with parametrised heating

The heat input in this type of models is described by either empirical parametrisations (Mok et al. 2008) or the relations derived by reduced MHD models (Lionello et al. 2013). In either case the heating rate is related to the magnetic field, which implies that the heating should be essentially from the interact of the fluid motion and the magnetic field in the lower solar atmosphere, as proposed by the DC or AC heating mechanisms. Despite of using a parametrised heating rate, these models solve the MHD problem with a proper coronal energy balance. Thus they are still suitable for studies on the dynamical response of the active region corona to a certain heat input. The plasma properties in the model can be used to synthesise coronal emission that is directly comparable to observations. A nice

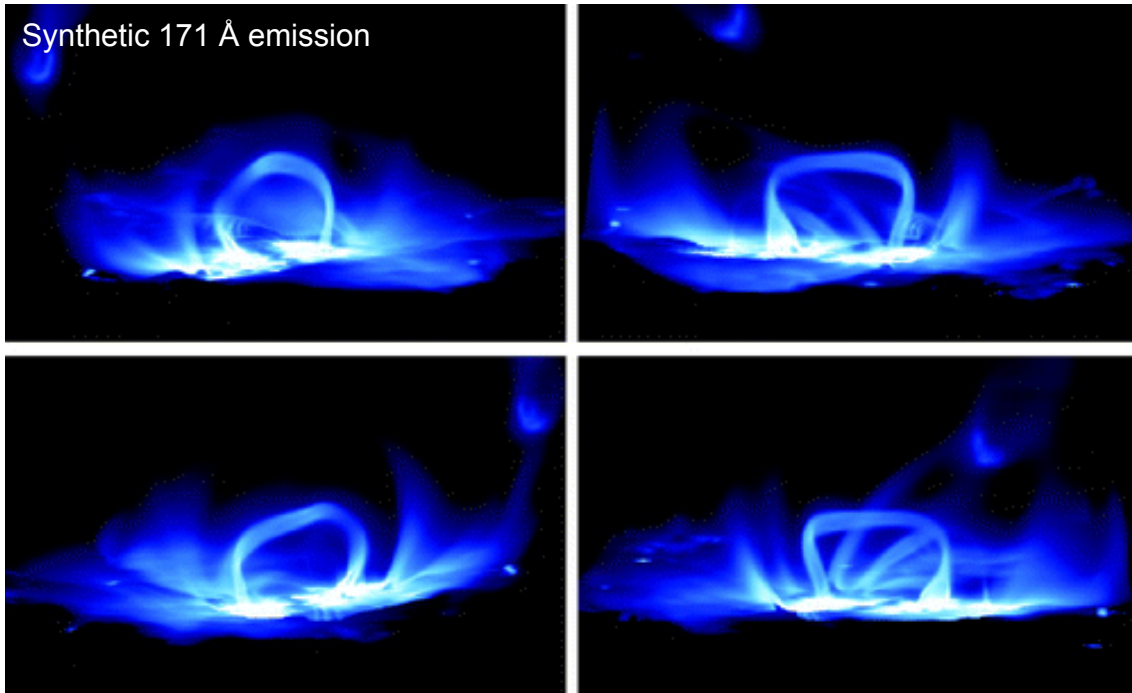


Figure 2.4: Synthetic 171 Å emission seen from four different viewpoints. The synthetic loop shows an almost constant cross section along the loop. This figure is taken from Mok et al. (2008).

example of the synthetic emission is shown in Fig. 2.4. Mok et al. (2008) synthesised the emission at 171 Å, which is mainly from the plasma at 1 MK, and integrated the emission along four different lines-of-sight (the four panels of Fig. 2.4). From all four viewpoints, the loop found in the synthetic observation shows a non-expanding cross section, which is a well-known feature of real loops observed in X-ray and EUV passbands.

2.6.3.2 Models accounting for magnetic braidings

Some more sophisticated active region models consider the heating from the field-line braiding (Parker 1972, 1983) and the flux tube tectonics (Priest et al. 2002) self-consistently in the full MHD problem. A series of models under the same strategy has been very successful in investigating the formation of coronal loops and various dynamics in the loops.

Gudiksen and Nordlund (2002, 2005a,b) firstly showed that the Ohmic dissipation from the currents induced by the braiding of magnetic fieldlines is sufficient to maintain a coronal temperature of over 1 MK. The synthetic coronal emission from the model is similar to observations (Fig. 2.5a,b). In their model (hereafter Gudiksen model), the magnetic field is based on a potential field extrapolated from an observed magnetogram of a real active region (Fig. 2.5c). They implemented an artificial horizontal velocity driver in the photosphere of the model. The velocity driver reproduces the general characters of the granular motions on the Sun. The footpoints of magnetic fieldlines are twined around each other by the velocity field, as proposed by Parker (1972, 1983) and Priest et al. (2002). The magnetic energy is converted to the internal energy of the coronal plasma in

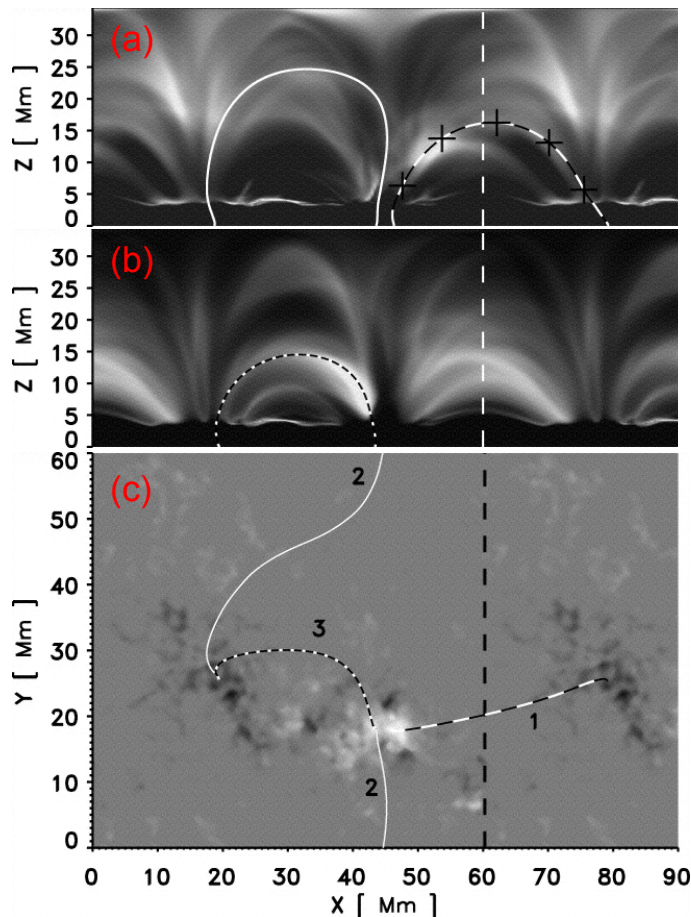


Figure 2.5: Synthetic emission showing the coronal loops in the Gudiksen model. Panel (a): Synthetic emission in the 171 Å channel. Panel (b): Synthetic emission in the 195 Å channel that is mainly from the 1.5 MK plasma, which is slight hotter than that sampled by the 171 Å images. Panel (c): Vertical magnetic field at the bottom of the simulation domain, i.e. the photosphere. Line 1 and line 2, which are magnetic fieldlines, indicate two loops identified in the 171 Å image, and line 3 shows a loop identified in the 195 Å image. Note that line 2 connects through the outside of the domain, due to the periodical lateral boundary. This figure is taken from Gudiksen and Nordlund (2005b).

a rate proportional $\eta \mathbf{j}^2$, where η is the resistivity and \mathbf{j} is the current. The magnetic field in their model photosphere and the synthetic EUV images are shown in Fig. 2.5. The synthetic 171 Å and the 195 Å images (showing the emission from plasma at a temperature of 1.5 MK) show a highly structured corona. The emission structures are found generally in line with magnetic fieldlines, as indicated by the three lines in Fig. 2.5.

As a key parameter of this type of model, η is typically determined by the relation

$$R_m^{\text{grid}} = \frac{U \Delta x}{\eta}, \quad (2.32)$$

where R_m^{grid} is *grid* magnetic Reynolds number, when choosing the grid spacing, Δx , as the length scale, and U is the characteristic speed. In this type of model R_e^{grid} should be

about unity, so that the dissipation is only efficient at the smallest spacial scale resolved by the model. If we choose the typical sound speed in the corona (100 km s^{-1}) as U and $\delta x \approx 100 \text{ km}$, the corresponding η is of the order of $10^{10} \text{ m}^2 \text{ s}^{-1}$. This resistivity seems to be much larger than the value suggested by the classical transport theory (e.g. $10 \text{ m}^2 \text{ s}^{-1}$). A larger η would yield a more diffused structure for the current. However the total amount of dissipated energy is expected to be unchanged, as long as η is determined by Eq. (2.32). This is supported by previous studies on the energy input through the Ohmic dissipation of induced currents (Hendrix et al. 1996, Galsgaard and Nordlund 1996, Rappazzo et al. 2008). Therefore, although present numerical experiments are still far from resolving the dissipation scale in the real corona, these models are expected to dissipate the same amount of energy as on the Sun.

In the models, the heating rate drops exponentially in height with a scale height ranging from 5 to 10 Mm. This generally applies to the averaged heating rate (Gudiksen and Nordlund 2002) and that along individual fieldlines (van Wettum et al. 2013). This scale height is in between the pressure scale height in the chromosphere and that in the corona. Consequently, the heating per particle, which is defined as the volumetric heating rate over the number density, peaks at the transition region (Bingert and Peter 2011). When following the temporal variation of the heating rate in a magnetic fieldline, Bingert and Peter (2011) found evidences for both continuous and intermittent heating. By discretising the Ohmic heating in the coronal into individual events, Bingert and Peter (2013) showed that the amount of energy released by a single event is mainly about 10^{17} J , which is consistent with nanoflares proposed by Parker (1988).

Peter et al. (2004, 2006) investigated the properties of the spectral lines synthesised from the Gudiksen model. They found that the synthetic spectral lines at transition region temperatures have a systematic redshift as observed on the Sun (Peter and Judge 1999). Furthermore the temporal variations in the line intensities and the Doppler velocities also show a good match with observations. In another model, Hansteen et al. (2010) found an interpretation for the blueshift generally observed in coronal spectral lines. Peter and Bingert (2012) showed that the appearance and temporal variations of the loop, which identified in the synthetic EUV observations, are similar to those in observations modern EUV imaging telescope. The analysis on the temperature and density distributions in the model coronal sheds new light on the long-known puzzle of the apparently non-expanding cross section of the loops observed EUV and X-ray passbands.

The result discuss above is not tuned to fit a particular active region, but to studies the general behaviours of the corona. Bourdin et al. (2013) built a model that is based on a magnetogram and a horizontal velocity field from actual observations. The geometry of the loop structures in the model active region is well consistent with the stereoscopic observations to the same active region. The Doppler velocity patterns in the active region is reproduced by the synthetic spectra from the model as well.

The realistic 3D models are a big step forwards from previous modelling approaches. They capture the essential physics underlying the observational features. When more details are revealed by the high quality observation, the realistic models serve as the best tool to investigate the heating of the corona and the dynamics in coronal structures.

2.7 Formation of active regions through the magnetic flux emergence

Most of the coronal loops are observed in solar active regions, which are the area with large scale strong magnetic flux concentrations. The interaction of the flows and the magnetic field in active regions are very likely to offer the energy budget for formation of coronal loops. Moreover, major solar activities, such as solar flares and coronal mass ejections (CMEs), are also born in active regions. Thus the formation and evolution of solar active regions, in particular their magnetic structures, are always intriguing topics.

During the formation stage of an active region, which is usually on a time scale of days, a large amount of magnetic flux emerges in the photosphere. The emerged flux forms strong magnetic flux concentrations of opposite magnetic polarities that has a length scale of several tens Mm (e.g. lower panels of Fig. 2.3). This is commonly interpreted as a magnetic flux tube breaking into the photosphere. The magnetic flux tubes are expected to be intensified by the dynamo process in the convection zone, buoyantly rise to the solar surface, and bring the magnetic flux further into the upper solar atmosphere (Fan 2009, Cheung and Isobe 2014). While another interpretation suggests that magnetic flux concentrations could be intensified near the solar surface by turbulent convections (Kleeorin and Rogachevskii 1994, Brandenburg et al. 2012, Warnecke et al. 2013). Thus there is no need for an intensified magnetic flux tube coming from the deeper convection zone.

In spite of the debate origin of magnet flux tubes, the emergence of the flux tube from the upper convection zone to the corona has been extensively investigated. However, most of the studies were aimed on the evolution of the magnetic field, and treated the plasma and radiation in the solar atmosphere in highly simplified manner (e.g., Fan 2001, Abbett and Fisher 2003, Manchester et al. 2004, Archontis et al. 2004, Magara 2006). Later models (Abbett 2007, Fang et al. 2010, 2012) made effort to improve the model atmosphere by including semi-empirical radiation in the lower solar atmosphere, radiative loss in the corona, and empirical heating related to the magnetic field.

Martínez-Sykora et al. (2008, 2009) studied the emergence of a twisted flux from the upper convection zone into the lower corona, on a spatial scale more representative for plage patches (of the order of 10 Mm). This model accounts for the radiative transfers in the lower atmosphere, with the anisotropic heating conduction and the optically thin radiation in the corona. The heating is added by the Ohmic dissipation. Although this model has a very sophisticated description on the atmosphere, the spatial scale is much smaller than typical solar active region. Furthermore, the magnetic features in this model did represent that in active region. However, it is much too computationally demanding to extend the models that consider convection zone and the corona at the same time into large spacial scales, e.g. representing active regions (of the order of 100 Mm).

Concerning more on the magnetic field structures from the convection zone up to the photosphere, highly realistic models have become possible to studies the sunspots structures (Heinemann et al. 2007, Rempel et al. 2009b) and the granulations in and around the sunspot Rempel et al. (2009a) on large spatial scales. With the proper treatment on the radiative transfer and equation of state, these models produced synthetic features that appears similar to even the finest observations. (Cheung et al. 2010) studied the emergence of a twisted magnetic flux tube through the upper convection zone. A pair of big

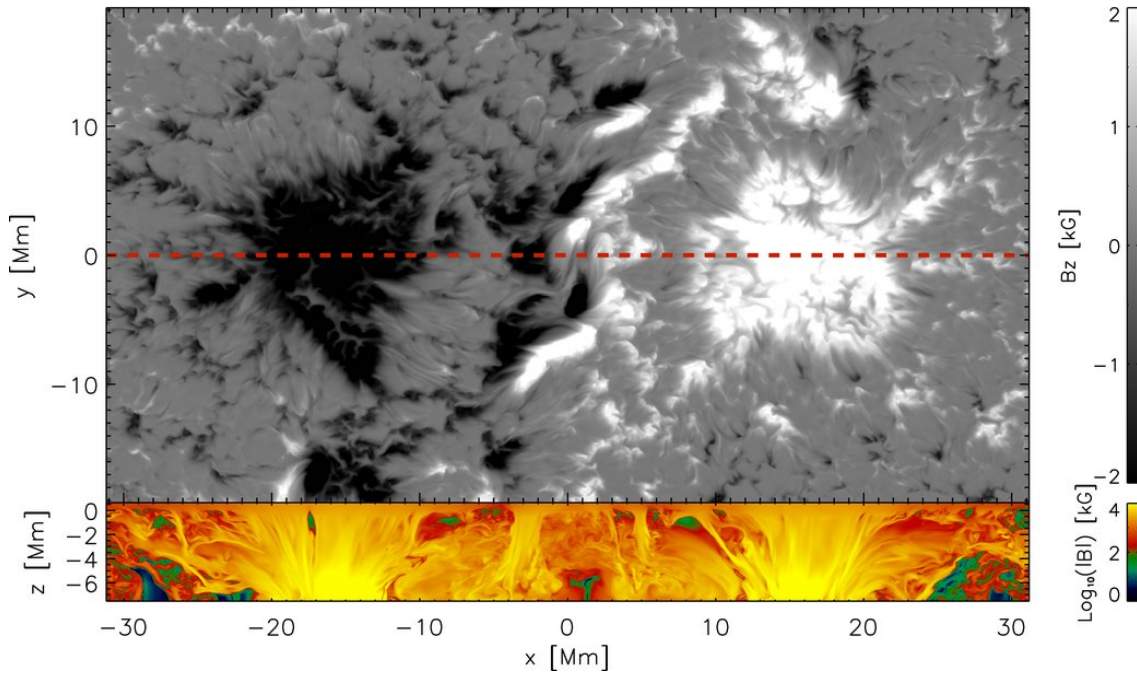


Figure 2.6: A pair of sunspots formed in the photospheric level of an flux emergence simulation. The upper panel shows the vertical magnetic field. The lower panel shows a vertical cut along the red dashed line and extending 7.5 Mm below the photosphere, where a torus shaped magnetic flux tube was injected at the beginning of the simulation. In the vertical cut, the footpoints of this flux tube are rooted at $x=12$ to 20 Mm and $x=-12$ to -20 Mm, symmetrically. They can be identified as the regions with the highest magnetic field strength. Meanwhile, the body of the flux tube has become very fragmented. This figure is taken from Cheung et al. (2010)

sunspots formed after the flux tube breaks into the photosphere, as shown in Fig. 2.6. The diameter of each sunspot is about 10 Mm. The field strength in the sunspots can exceed 2000 G. These features are quite comparable to real active regions. Rempel and Cheung (2014) further applied the same modelling strategy on full life of an active region, from the emergence to the decay. Compared with models of Martínez-Sykora et al. (2008, 2009), these models have similarly sophisticated treatment on the radiative transfer in the lower atmosphere, and their spatial scale has been comparable to typical active regions. However, they have to omit the upper atmosphere, i.e. the corona.

2.8 Motivation and aim of this study

The coupling of different layers in the solar atmosphere, is considered to be a key understand the solar atmosphere. Many efforts have been made to understand the formation of the coronal features and their connections to the lower atmosphere, as we have introduced in the sections above. How coronal structures in an active region form at the same time of the emergence of magnetic flux in the photosphere is a peak that is not yet conquered. However, depicting a comprehensive picture on the plasma properties, magnetic structures would require the model to properly treat the fundamental physics from convection

zone to the corona. Unfortunately such a model would be much too computationally demanding for the present-day computing power.

Both the realistic flux emergence model spanning from convection zone to the photosphere (Cheung et al. 2010, Rempel and Cheung 2014) and the realistic coronal models that covers the atmosphere starting the photosphere (the Gudiksen model, Bingert and Peter 2011, Bourdin et al. 2013) have been very successful in their own regime. This inspires us to couple a coronal simulation to a flux emergence simulation.

The convection zone and the photosphere are basic in the high β regime, where the fluid drives the magnetic field evolution. Meanwhile the majority of the corona is in the low β regime, where the magnetic field dominates over the plasma. Therefore, the coupling between the two models is actually *driving* the coronal simulation with the flux emergence simulation (see Sect. 3.2.3 for the implementation), while the back reactions of the corona to the photosphere, which are supposed to be minor during the flux emergence, are omitted. Nonetheless, this provides the unique model in which we can study the corona dynamics driven by magnetic flux emergence.

This coupled model has the following advantages compared with previous models.

- It has a proper treatment on the energetics of the coronal plasma, compared with flux emergence models with a simplified atmosphere (Sect. 2.7).
- It has a self-consistent heat input from the interaction of the fluid and the magnetic field in the photosphere, compared with coronal models using a prescribed heating rate (Sect. 2.6.3.1).
- It has an evolving magnetic structure in response to the vast magnetic flux emergence. This is substantially different with coronal models, in which the magnetic field only changes gently and slightly due to braidings in the photosphere (Sect. 2.6.3.2).
- It can model an active region on a spatial scale of 100 Mm, which is one order of magnitude larger than that of the model solving the flux emergence from the convection zone to the corona (Sect. 2.7).

In the coronal model driven by magnetic flux emergence we will study the energy budget for coronal loops, the dynamics of the loops, and the evolution of EUV and magnetic structures. The comparison to previous models will highlight how this model shed new light on the dynamics in a forming active region.

In Chap. 3, we first give a description on the numerical method. Then we introduce the basic properties of the flux emergence simulation and the configuration of the coronal simulation. Finally, we describe how the coupling of the flux emergence simulation and the coronal simulation is implemented.

In Chap. 4 we show the analysis focused on the first loop-like structure found in the synthetic EUV images. We exam the thermal dynamics along the magnetic fieldline hosting the EUV loop, and compare the dynamics with traditional 1D loop models. Furthermore, we demonstrate how the density and temperature structures in 3D space determin the cross section of the EUV loop. Finally we reveal the character of the energy input in the lower atmosphere that essentially triggers the formation of the loop. This analysis depict an overall picture of the built-up of a coronal loop in a forming active region.

We then focus on the evolution of EUV loops and the magnetic field in Chap. 5. By tracing the evolution of the apparent EUV structure (i.e. the EUV loop) and a bundle of magnetic fieldlines (i.e. the magnetic loop), we show that their evolution are not identical, even though in any static image a EUV loop is nicely along the magnetic fieldline. The reason is found by investigating how the heat input in individual magnetic fieldlines sets their density and temperature when the footpoints of these fieldlines are advected into the sunspot by the coalescent flow in the photosphere. This analysis reveals the substantial difference between the dynamics in an emergence active region and that in a stable active region.

In Chap. 6 we study the transverse oscillations in coronal loops, which is an example of the detailed dynamics in the model. The damped oscillation can be well identified by the synthetic imaging and spectroscopic observations. Its (synthetic) observational properties is very similar with oscillations observed in real corona. Thus the realistic model can serve as a test case for techniques applied on real observation, such as corona seismology.

Finally we summarise the results in Chap. 7 and discuss further extensions of the present work.

3 Coronal simulations driven through the bottom boundary

3.1 Numerical method

3.1.1 Governing equations

We use the PENCIL CODE¹ to numerically solve the MHD problem. The equations for coronal simulations in the PENCIL CODE read,

$$\frac{\partial \ln \rho}{\partial t} = -(\mathbf{u} \cdot \nabla) \ln \rho - \nabla \cdot \mathbf{u}, \quad (3.1)$$

$$\frac{\partial \mathbf{u}}{\partial t} = -(\mathbf{u} \cdot \nabla) \mathbf{u} + \frac{1}{\rho} \left[-\nabla p + \rho \mathbf{g} + \mathbf{j} \times \mathbf{B} + 2\nu \nabla \circ (\rho \underline{S}) \right], \quad (3.2)$$

$$\frac{\partial \mathbf{A}}{\partial t} = \mathbf{u} \times \mathbf{B} - \eta \mu_0 \mathbf{j}, \quad (3.3)$$

$$\frac{\partial \ln T}{\partial t} = -(\mathbf{u} \cdot \nabla) \ln T - (\gamma - 1) \nabla \cdot \mathbf{u} + \frac{1}{c_V \rho T} \left(\eta \mu_0 \mathbf{j}^2 + 2\rho \nu \underline{S}^2 - \nabla \cdot \mathbf{q} - L_{\text{rad}} \right), \quad (3.4)$$

where ν is the viscosity, η the resistivity, c_V the specific heat capacity at constant volume, \mathbf{A} the vector potential, and \underline{S} the rate-of-strain tensor written as

$$\underline{S} = \frac{1}{2} \left(\frac{\partial u_i}{\partial x_j} + \frac{\partial u_j}{\partial x_i} \right) - \frac{1}{3} \delta_{ij} \nabla \cdot \mathbf{u}. \quad (3.5)$$

In the energy equation (Eq. (3.4)), $\eta \mu_0 \mathbf{j}^2$ is the Ohmic heating from the dissipation of free magnetic energy, and $2\rho \nu \underline{S}^2$ is the viscose heating from the dissipation of the kinetic energy. The heat flux of the Spitzer heat conduction, \mathbf{q} , is written as

$$\mathbf{q} = -\kappa_0 T^{5/2} \mathbf{b}(\mathbf{b} \cdot \nabla T), \quad (3.6)$$

which is the same as Eq. (2.15). The energy loss through the optically thin radiation, L_{rad} , is evaluated by

$$L_{\text{rad}} = n_e^2 \Lambda(T), \quad (3.7)$$

as in Eq. (2.14). We use the contribution function, $\Lambda(T)$, given by Cook et al. (1989).

The MHD equations are solved together with the equation of state for an ideal gas (Eq. (2.6)). We use $\tilde{\mu}=0.667$, as given by Bingert and Peter (2011). In total this set of

¹<https://github.com/pencil-code/>

equations describes the evolution of the fully compressible plasma with a proper treatment on the energy balance in the solar corona including the heat conduction along the magnetic field, the loss of energy through the optically thin radiation, and the heating by the dissipation of the magnetic and kinetic energy. The spatial derivatives are evaluated by a sixth order center finite difference scheme, while the time integration is discussed in Sect. 3.1.2 and Sect. 3.1.3.

Induction equation of the magnetic field

We solve the induction equation of the vector potential, \mathbf{A} . The magnetic field is defined by

$$\mathbf{B} = \nabla \times \mathbf{A}. \quad (3.8)$$

This guarantees that the magnetic field is perfectly solenoidal, i.e.

$$\nabla \cdot \mathbf{B} = \nabla \cdot (\nabla \times \mathbf{A}) = 0.$$

The curl of Eq. (3.3) reads,

$$\nabla \times \left(\frac{\partial \mathbf{A}}{\partial t} \right) = \nabla \times (\mathbf{u} \times \mathbf{B}) - \nabla \times (\eta \mu_0 \mathbf{j}). \quad (3.9)$$

With the Ampère's law, $\mu_0 \mathbf{j} = \nabla \times \mathbf{B}$, this equation can be written as

$$\frac{\partial \mathbf{B}}{\partial t} = \nabla \times (\mathbf{u} \times \mathbf{B}) - \nabla \times (\eta \nabla \times \mathbf{B}), \quad (3.10)$$

which is the common form of the induction equation of magnetic field, i.e. Eq. (2.3). We have the freedom to add the gradient of scalar, $\nabla \phi$, to the right hand side of Eq. (3.3). This is known as the gauge for the induction equation of \mathbf{A} . The curl of $\nabla \phi$ vanishes, thus the gauge does not change the equation of \mathbf{B} . In our simulations, we apply the resistive gauge, which adds $\nabla(\eta \nabla \cdot \mathbf{A})$ to Eq. (3.3). When η is a constant in space, Eq. (3.3) can be formulated to

$$\frac{\partial \mathbf{A}}{\partial t} = \mathbf{u} \times \mathbf{B} + \eta \nabla^2 \mathbf{A}. \quad (3.11)$$

Limiting the Alfvén speed

The Alfvén speed in the model solar atmosphere can be extremely high, particularly above the sunspots. As described later in Sect. 3.2 we use a non-uniform grid spacing in the vertical direction of the coronal simulation. The smallest grid spacing is 32 km near the bottom. Therefore, the time step would be severely limited by the very high Alfvén speed and the small grid spacing.

We control the Alfvén speed by limiting the Lorentz force to obtain a large time step, as applied by Rempel et al. (2009b). When the Alfvén speed exceeds $v_{A0}=2000 \text{ km s}^{-1}$, a factor defined as

$$f_A = v_{A0}^2 \left(v_A^4 + v_{A0}^4 \right)^{-1/2} \quad (3.12)$$

is applied to the Lorentz force, i.e. the $\mathbf{j} \times \mathbf{B}$ term in Eq. (3.2). The corresponding effective Alfvén speed (\tilde{v}_A) in the model is evaluated by $\tilde{v}_A^2 = v_A^2 f_A$, which can not exceed v_{A0} as

the result of the limiting. For a coronal loop of a density of 10^9 cm^{-3} and a magnetic field strength of 100 G, the original Alfvén of about 6500 km s^{-1} is reduced by a factor of about 3. The model corona still keeps a sufficiently low plasma β . The effective Alfvén speed is larger than the fastest sound speed (e.g. 150 km s^{-1}) in the model by more than one order of magnitude. Therefore, the plasma beta in the corona is still well below the 10^{-2} .

3.1.2 Time step constraint

The MHD equations is integrated in time by an explicit third order Runge-Kutta scheme described by Williamson (1980). The time step is limited by the Courant-Friedrichs-Lewy (CFL) condition. The time step, δt is evaluated by

$$\delta t = \min \left(c_{\delta t} \frac{\delta x_{\min}}{u_{\max}}, c_{\delta t, v} \frac{\delta x_{\min}^2}{D_{\max}} \right), \quad (3.13)$$

where δx_{\min} is the minimum grid spacing, u_{\max} the largest flow/wave speed including the sound speed and Alfvén speed, and D_{\max} the largest diffusivity. c is a coefficient less than unity. Here we use $c_{\delta t}=0.8$ and $c_{\delta t, v}=0.4$.

Under typical coronal conditions, the time step limited by the thermal diffusivity of the Spitzer heat conduction is significantly smaller than all the others. The thermal diffusivity is defined as

$$\chi = \frac{\kappa_0 T^{5/2}}{c_V \rho}, \quad (3.14)$$

Given a grid spacing of 200 km, the heat conduction time step for the corona plasma of a density of 10^9 cm^{-3} and a temperature of 2 MK is evaluated as

$$\delta t_{\text{spitzer}} = c_{\delta t, v} \frac{\delta x_{\min}^2}{\chi} \approx 6 \times 10^{-5} \text{ s}. \quad (3.15)$$

The second smallest time step in our simulation is usually limited by the viscosity and resistivity that are determined by the grid Reynolds number, Eq. (2.32). For the typical viscosity and resistivity we use, the correspond time step is about $5 \times 10^{-3} \text{ s}$, which larger than $\delta t_{\text{spitzer}}$ by two orders of magnitude.

We are interested in the evolution of an active region corona in a period of the order of hours. Given the time step constraint by the heat conduction, it would require about 10^8 step, which is a high computational demand. One solution to this problem is using implicit time stepping schemes which are unconditionally (numerically) stable for any length of time step. The disadvantage of using implicit time stepping schemes is that they need to solve a large system of linear equations. This requires inverting of the global scale matrix which is very computationally demanding. Moreover in massively parallel computations as what we do (e.g. usually with 4096 processors), the global message communication between processors may become a substantial limit to the computation speed. (In comparison, explicit time stepping schemes would mainly require communications of the boundary information between neighbouring processors.)

Finally even though implicit schemes are unconditionally stable in the numerical aspect. The largest time step is still limited by the characteristic time scale of the physical variations of the model. The computational demand and the communication bottleneck in

massively parallel computations may make the actual speed up even lower. In real practice, a code using an implicit time stepping scheme for the heat conduction (Gudiksen et al. 2011) can actually gain a speeding-up of about 4.

3.1.3 Sub-cycle for the heat conduction

As an alternative to using the implicit time stepping scheme, we treat the heat conduction term in a loop separated from the main MHD equations. This choice is based on that the time step limited by the heat conduction is significantly smaller than the second smallest time limit.

Let δt_{2nd} denote the second smallest time step limit. When we evolve the full MHD equation from t^n to $t^n + \delta t_{2nd}$, we first evolve the continuity equation, the momentum equation, and the energy equation *without* the heat conduction term. This set of equations can be evolved stably by the explicit Runge-Kutta time stepping scheme with a time step of δt_{2nd} .

Then in a "sub-cycle" for the heat conduction, we can consider an energy equation that *only* contains the heat conduction term, which reads

$$\frac{\partial \ln T}{\partial t} = -\frac{1}{c_V \rho T} (\nabla \cdot \mathbf{q}). \quad (3.16)$$

This equation is integrated in time with a time step $\delta t_{\text{Spitzer}}$. The time integrate in the sub-cycle is repeated until the time in the sub-cycle is evolved by δt_{2nd} in total. Therefore the amount of iterations in the sub-cycle is about $\delta t_{2nd}/\delta t_{\text{Spitzer}}$.

In this way the full MHD equations are evolved from t^n to $t^n + \delta t_{2nd}$. The computation on the majority of the equations can be reduced by a factor of about $\delta t_{2nd}/\delta t_{\text{Spitzer}}$. Thus we get a significant speed up compared to evolving the full equations with $\delta t_{\text{Spitzer}}$.

3.1.4 Super time stepping in the sub-cycle

In practice, $\delta t_{\text{Spitzer}}$ is usually smaller than δt_{2nd} by two orders of magnitude. The amount of iterations in the sub-cycle is usually of the order of 100. By applying a super time stepping scheme on the time integration of the energy equation in the sub-cycle, we are able to evolve it with a time step significantly enhanced from $\delta t_{\text{Spitzer}}$. Therefore the amount of iterations in the sub-cycle is reduced correspondingly.

The super time stepping is a (family of) very efficient method to speed up computations for parabolic equations, such the heat conduction problem. It is essentially a class of multi-step Runge-Kutta method. By doing s sub-steps in a full time step of the super time stepping, it achieves a time step that is enhanced from the time step determined by the CFL condition (i.e. the time step for the ordinary Runge-Kutta method) by a factor proportional to s^2 .

In our simulation, we implement the method described by Meyer et al. (2012). The sub-steps are designed based on the recursion relation of shifted Legendre polynomials. Therefore, it is also referred as the Runge-Kutta-Legendre (RKL) method. Here we give only a brief description of this method.

A general parabolic equation is written as

$$\frac{\partial U}{\partial t} = L_{\text{para}}(U), \quad (3.17)$$

where U is a variable and L_{para} is a parabolic operator. When this equation is evolved one time step forward, i.e. from t^n to $t^{n+1}=t^n + \delta t_{\text{RKL}}$, the RKL scheme with s sub-steps is written as

$$\begin{aligned}
 Y_0 &= U^n \\
 Y_1 &= Y_0 + \tilde{\mu}_1 \delta t_{\text{RKL}} L_{\text{para}}(Y_0) \\
 Y_j &= \mu_j Y_{j-1} + \nu_j Y_{j-2} + (1 - \mu_j - \nu_j) Y_0 \\
 &\quad + \tilde{\mu}_j \delta t_{\text{RKL}} L_{\text{para}}(Y_{j-1}) + \tilde{\gamma}_j \delta t_{\text{RKL}} L_{\text{para}}(Y_0); \quad 2 \leq j \leq s \\
 U^{n+1} &= Y_s,
 \end{aligned} \tag{3.18}$$

where U^n and U^{n+1} are the solutions at t^n and t^{n+1} , respectively. Y_j is the approximate solution at each sub sub-step. The recursion relation is determined by the parameters μ_j , $\tilde{\mu}_j$, ν_j , and $\tilde{\gamma}_j$. These parameters are defined as

$$\begin{aligned}
 \tilde{\mu}_1 &= \frac{4}{3(s^2 + s - 2)}, \quad \mu_j = \frac{2j-1}{j} \frac{b_j}{b_{j-1}}, \\
 \tilde{\mu}_j &= \frac{4(2j-1)}{j(s^2 + s - 2)} \frac{b_j}{b_{j-1}}, \quad \nu_j = -\frac{j-1}{j} \frac{b_j}{b_{j-2}}, \\
 \tilde{\gamma}_j &= -a_{j-1} \tilde{\mu}_j, \quad a_j = 1 - b_j, \\
 b_j &= \frac{j^2 + j - 2}{2j(j+1)}, \quad 2 \leq j \leq s \\
 b_0 &= b_1 = b_2 = \frac{1}{3}.
 \end{aligned} \tag{3.19}$$

If the time step of Eq.(3.17) limited by the CFL condition is δt_{para} , the time step constraint for the RKL method is

$$\delta t_{\text{RKL}} \leq \frac{s^2 + s - 1}{4} \delta t_{\text{para}}. \tag{3.20}$$

Meyer et al. (2012) noted that people should use odd values of s , for sake of a better numerical stability. For our simulation, we can in principle choose an odd value of s' , so that δt_{RKL} is equal to $\delta t_{2\text{nd}}$. Therefore the evolution of Eq. (3.16) from t^n to $t^n + t_{2\text{nd}}$ could be done by one RKL step with s' sub-steps, and there is actually no need for the sub-cycle iteration. However, in real practice we find that using a large s is very likely to be unstable, particularly in 3D simulations. The typical s value we use in our simulations is 3 or 5. Compared to the ordinary third order Runge-Kutta scheme (containing 3 sub-steps), $s=3$ achieves an enhancement of 2.5 in time step, as determined by Eq. (3.20), with few extra computation. For $s=5$, we obtain an enhancement in time step of 7. The computational demand is also increased because more sub-steps need to be calculated. In together we get a speeding-up of about 4.

Summary for the time stepping strategy

In summary, the most severe time step constraint in our simulation is from the Spitzer heat conduction along the magnetic field, i.e. $\delta t_{\text{Spitzer}}$, which is usually smallest than the second smallest time step, $\delta t_{2\text{nd}}$, by 2 orders of magnitude. We evolve the majority of the MHD equations with $\delta t_{2\text{nd}}$ by a third order Runge-Kutta scheme, and evolve an energy equation that only considers the heat conduction in a sub-cycle. The energy equation in the sub-cycle is a parabolic equation that can be evolved with the Runge-Kutta-Legendre scheme. With this method, we are able to evolve the energy equation in the sub-cycle with a time step of δt_{RKL} that is enhanced from $\delta t_{\text{Spitzer}}$ by a factor of about 2.5 to 4. Therefore the number of iterations in the sub-cycle is reduced. In total, by using the sub-cycle and the RKL scheme we can achieve a significant speeding-up compared to evolving the full MHD equations with the smallest time step ($\delta t_{\text{Spitzer}}$). The speeding-up factor varies during the simulation, because it depends on the ratio of $\delta t_{2\text{nd}}$ to δt_{RKL} . Nonetheless it is supposed to be better than the speeding-up factor if we would use an implicit time stepping scheme for the heat conduction, because we usually execute massively parallel computations on over 4000 processors, which would severely limit the efficiency of implicit schemes.

3.2 Model setup

The idea of our coupled model is that we use the output at the photospheric layers in a flux emergence simulation as the bottom boundary of a coronal simulation spanning from the photosphere to the upper corona. In this way we drive the coronal simulation and study the structures and dynamics in the model corona driven by the flux emergence in the photosphere.

Here we give a description of the flux emergence simulation used as the input at the boundary (Sect. 3.2.1), the configuration of the coronal simulation (Sect. 3.2.2), and the approach to drive the coronal simulation from the bottom boundary (Sect. 3.2.3).

3.2.1 The flux emergence simulation

The flux emergence simulation is done by the MPS/University of Chicago Radiative MHD (MURaM) code (Vögler et al. 2005, Rempel et al. 2009b). This code accounts for the non-gray radiative transfer and a realistic equation-of-state (EOS) for the partially ionized plasma in the lower solar atmosphere. Simulations from the MURaM code can model the magnetoconvection in the upper solar convection zone, and the plasma and magnetic properties in the lower solar atmosphere. These highly realistic simulations are comparable to state-of-the-art observations.

The advantage of driving the corona with simulation data is that these simulations successfully resemble the key features in photosphere of the real Sun. The data from the simulation offer the full information on the evolution of the density, temperature, velocity and magnetic field. Some of these quantities in the photosphere are still difficult to measure directly from observations, for example the horizontal component of the velocity. Previous coronal simulations usually use an artificial velocity field similar to the typical granular motions in the photosphere. However this trades off the self-consistency in the evolution of the velocity and magnetic field. Therefore the realistic simulation is a

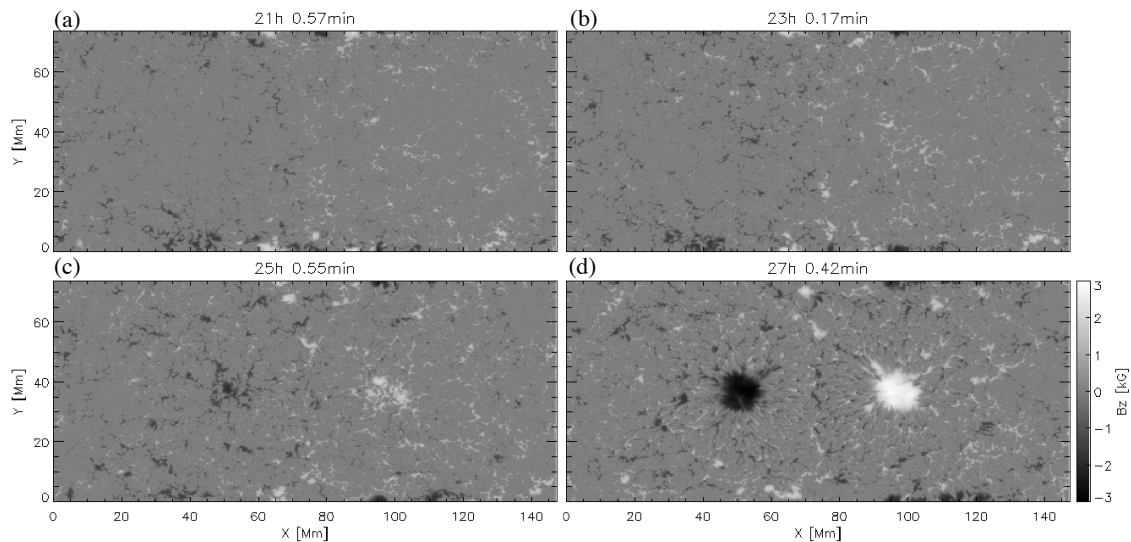


Figure 3.1: Evolution of the vertical magnetic field in the photosphere of the flux emergence simulation. It demonstrates the emergence and coalescence of magnetic flux in the photosphere in 6 solar hours. See Sect. 3.2.1 for details.

good option as a self-consistent driver for coronal simulations, in particular if we intend to study the flux emergence process.

The flux emergence simulation we use is designed by Cheung et al. (2010) and Rempel and Cheung (2014). The computational domain covers an area of $147.5 \times 73.7 \text{ Mm}^2$, and spans 16.4 Mm in the vertical direction. The horizontal grid spacing is 96 km and the vertical is 32 km . The bottom boundary is 15.7 Mm below the model photosphere, where the average optical depth is unity. Therefore the simulation is mainly designed to study the emergence of a flux tube from the upper convection zone to the photosphere.

The simulation is first relaxed to a non-magnetic convection. As the start of the flux emergence, a semi-torus magnetic flux tube is advected kinematically across the bottom boundary by a vertical velocity of 500 m s^{-1} . After the semi-torus is fully advected into the domain, it then evolves freely. The flux tube has no imposed twist, i.e. the magnetic field is purely in the direction of the axis. It contains a total magnetic flux $1.7 \times 10^{22} \text{ Mx}$. The magnetic field strength is 10.6 kG at the axis.

The magnetic flux tube buoyantly rises through the convection zone and reach the photosphere. During the process it is fragmented by the interaction with the convective motions. In the photosphere, many small scale magnetic elements, with a field strength of a few hundred or over one thousand Gauss, appear first (Fig. 3.1a). Later the small magnetic elements start to coalescent with each other and form larger magnetic flux patches (Fig. 3.1b and c). At about 27h after the injection of the flux tube at the bottom, a pair of Sunspots forms in the photosphere (Fig. 3.1d). Each sunspot has a diameter of about 15 Mm . The highest magnetic field strength at the center may exceed 2000 G . These model sunspots are very similar to a large active region in the real Sun.

We extract a full set of variables in *four consecutive horizontal layers* in the model photosphere with a 25 s cadence. We use this dataset as the bottom boundary that will drive the coronal simulation. The number of horizontal layers are determined by the sixth

order central finite difference scheme in the PENCIL CODE, which requires three ghost cells at the bottom boundary. We would put one more layer in the first cell of the computation domain. Therefore, four horizontal layers in total are required. (see Fig. 3.2 and detailed descriptions in Sect. 3.2.3).

3.2.2 Setup of the coronal model

The coronal simulation focuses on the further evolution of the emerged magnetic field from the photosphere into the higher solar atmosphere and the dynamical response of the coronal plasma to the injection of the magnetic energy.

3.2.2.1 Computation domain

The domain of the coronal simulation is identical to the flux emergence simulation in the horizontal direction. We conduct two numerical experiments with different designs for the grid (hereafter, the low resolution run and the high resolution run), as following.

- *Low resolution run*

This is preparatory test for later high resolution simulations. The horizontal domain of $147.5 \times 73.7 \text{ Mm}^2$ is resolved 256×128 grid points, which yields a 576 km grid spacing. The computation domain that spans 73 Mm upward from the photosphere is resolved by 256 grid points. We use a non-uniform grid in the vertical direction. The grid spacing is 32 km at the bottom (to match that of the flux emergence simulation), and about 300 km in the coronal part.

- *High resolution run*

This is our production run based on the successful preparatory low resolution test. The horizontal domain of $147.5 \times 73.7 \text{ Mm}^2$ is resolved 1024×512 grid points. The horizontal grid spacing is 144 km, which is higher than that of the low resolution run by a factor of 4. In the vertical direction, we use non-uniform grid with 256 points to resolve a reduced domain height of 50 Mm, because we found in the low resolution run that the interesting features and dynamics are mainly below the height of 20 Mm. The vertical grid spacing is 32 km at the bottom, and 190 km in the coronal part of the domain.

3.2.2.2 Initial conditions

In the early stage of the flux emergence simulation, the flux tube is still in the convection zone. These period is not particularly interesting for the study of coronal dynamics. Only in the later stage, when the strong magnetic flux concentrations start to form, the coronal dynamics becomes worth of studies. Therefore, the start of the coronal simulations are usually later than $t=20$ h in the flux emergence simulation.

The low resolution run starts at $t=21$ h, while the high resolution run starts at $t=24$ h, because we found in the former that the first coronal feature only appear after $t=25$ h.

The initial atmosphere is design to have a stratification similar to the real solar atmosphere. The temperature at the bottom is 5100 K. It increases to 1 MK in the corona part, with a transition at about 3 Mm in height. The density at the bottom is set by the average

density of the horizontal layers from the flux emergence simulation. The density profile is calculated from the hydrostatic equilibrium.

The initial magnetic field in the coronal simulation is a potential field determined by the vertical magnetic field at the bottom, which is from the photospheric magnetic field in the flux emergence simulation. In this stage the magnetic field in the photosphere is still mainly distributed small scale magnetic elements. The coronal magnetic field is almost completely reconfigured when the stronger magnetic field from the flux tube emerges through the photosphere and expands to the higher atmosphere.

3.2.2.3 Boundary conditions

The lateral boundaries are periodic for all variables. This potentially allows magnetic fieldlines in the emerging active region to connect to the outside of the simulation domain (e.g. the white solid line in Fig. 2.5, albeit in a stable active region). However, we would like to keep the emerging active region in the simulation isolated from neighbouring active regions (due to the periodic lateral boundary). The original flux emergence simulation has developed an enough quiescent Sun area around the emerging active region, so that the magnetic fieldlines in the active region mainly connect the two sunspots. Otherwise, one has to manual set up some quiescent Sun magnetic field around the active region, as what was implemented by Bourdin et al. (2013).

At the top boundary, the temperature is set to have a zero gradient, so that the heat flux vanishes at the top boundary. This makes sure that the model corona will not be heated by any external heat flux from the top. The velocity vanishes and the density is extrapolated upward with the hydrostatic equilibrium. This sets up a hydrostatic top boundary, because the dynamics at the top is of no interest in this model. The magnetic field is connected to a potential field, which is a common approximation to the coronal magnetic field on the large scale. While some slight currents are built at the interface of the non-potential magnetic field and the potential one, the corresponding Ohmic heating is very weak and has no impact on the plasma properties in the region of interest.

The bottom boundary, which is set by the input from the flux emergence simulation, is the time-dependent driver of the coronal simulation. The implementation is described in detail in the next section, i.e. Sect. 3.2.3.

3.2.3 Coupling of the flux emergence and corona model

To drive the coronal simulation by the input from the flux emergence simulation, we first need to convert the variables to those can be used in the coronal simulation, i.e. $\ln \rho$, $\ln T$, \mathbf{u} , and \mathbf{A} .

The input from the flux emergence simulation contains the density, internal energy, momentum and magnetic field. The density can be directly used. The velocity can be derived straightforward from the density and momentum. The temperature can be deduced by the density and internal energy through the realistic (tabular) equation of state used by the MURaM code (Vögler et al. 2005).

Our coronal simulations use the vector potential, \mathbf{A} , as the variable for the induction equation. Therefore we need to calculate the vector potential from the magnetic field.

3.2.3.1 Preparing the vector potential

From the relation of \mathbf{A} and \mathbf{B} , and the Ampère's law, we obtain

$$\nabla \times (\nabla \times \mathbf{A}) = \mu_0 \mathbf{j},$$

which can be written as

$$\nabla(\nabla \cdot \mathbf{A}) - \nabla^2 \mathbf{A} = \mu_0 \mathbf{j}, \quad (3.21)$$

The current, \mathbf{j} , in the four layers from the flux emergence simulation is evaluated by the curl of \mathbf{B} in the same dataset. The dataset is periodic in the horizontal direction, which allows us to use a sixth order central difference to calculate the horizontal derivatives. However, this dataset has only four point in the vertical direction, thus we use a four-point-stencil one-side difference for the vertical derivatives.

We have the freedom to choose the gauge for the vector potential. When the difference between two vector potentials \mathbf{A}_1 and \mathbf{A}_2 can be written as

$$\mathbf{A}_1 = \mathbf{A}_2 + \nabla \phi, \quad (3.22)$$

where ϕ is an arbitrary scalar, the magnetic fields defined by \mathbf{A}_1 and \mathbf{A}_2 are identical, because

$$\begin{aligned} \mathbf{B}_1 &= \nabla \times \mathbf{A}_1 \\ &= \nabla \times (\mathbf{A}_2 + \nabla \phi) \\ &= \nabla \times \mathbf{A}_2 + \nabla \times (\nabla \phi) \\ &= \nabla \times \mathbf{A}_2 \\ &= \mathbf{B}_2. \end{aligned} \quad (3.23)$$

Here we apply $\nabla \cdot \mathbf{A} = 0$ in Eq.(3.21) and obtain

$$\nabla^2 \mathbf{A} = -\mu_0 \mathbf{j}. \quad (3.24)$$

Both the flux emergence simulation and the coronal simulation are periodic in the horizontal dimension, thus we apply a two dimensional Fourier transform on Eq.(3.24) in each horizontal layer respectively. In the Fourier space,

$$\frac{\partial}{\partial x} \rightarrow ik_x, \text{ and } \frac{\partial}{\partial y} \rightarrow ik_y,$$

where k_x and k_y are the wave number. The partial differential equation, Eq.(3.24), is converted into a set of ordinary differential equations (ODEs) that reads,

$$\frac{d^2 \hat{A}_x}{dz^2} = k^2 \hat{A}_x - \mu_0 \hat{J}_x, \quad (3.25)$$

$$\frac{d^2 \hat{A}_y}{dz^2} = k^2 \hat{A}_y - \mu_0 \hat{J}_y, \quad (3.26)$$

$$\frac{d^2 \hat{A}_z}{dz^2} = k^2 \hat{A}_z - \mu_0 \hat{J}_z, \quad (3.27)$$

where \hat{A}_x is the Fourier transform of A_x (the same for the other components of \mathbf{A} and \mathbf{j}), and $k^2 = k_x^2 + k_y^2$. The relations, $\mathbf{B} = \nabla \times \mathbf{A}$ and $\nabla \cdot \mathbf{A} = 0$, are also rewritten as

$$\hat{B}_x = ik_y \hat{A}_z, -\frac{d\hat{A}_y}{dz} \quad (3.28)$$

$$\hat{B}_y = \frac{d\hat{A}_x}{dz} - ik_x \hat{A}_z \quad (3.29)$$

$$\hat{B}_z = ik_x \hat{A}_y - ik_y \hat{A}_x \quad (3.30)$$

$$0 = ik_x \hat{A}_x + ik_y \hat{A}_y + \frac{d\hat{A}_z}{dz}. \quad (3.31)$$

The task is to solve the system of the second order ODEs in the four horizontal layers. We use a fourth order Runge-Kutta method to integrate Eq. (3.25), Eq. (3.26), and Eq. (3.27) from $l=0$ to $l=3$, where $l=0$ is the lowest layer and $l=3$ the highest. For example Eq. (3.25) is decomposed into two first order ODEs, which are written as

$$\frac{du_1}{dz} = u_2, \quad (3.32)$$

$$\frac{du_2}{dz} = k_x^2 \hat{A}_x - \mu_0 \hat{j}_x, \quad (3.33)$$

where $u_1 = \hat{A}_x$, and $u_2 = \frac{d\hat{A}_x}{dz}$. Eq. (3.26) and Eq. (3.27) can be reformulated in the same way.

At $l=0$, the boundary values for u_1 and u_2 (i.e. $\hat{A}_x, \hat{A}_y, \hat{A}_z$, and their vertical derivatives) are defined as,

$$\hat{A}_x, l=0 = \frac{-k_y \hat{B}_z, l=0}{ik^2}, \quad \left(\frac{d\hat{A}_x}{dz} \right)_{l=0} = \hat{B}_y, l=0 \quad (3.34)$$

$$\hat{A}_y, l=0 = \frac{k_x \hat{B}_z, l=0}{ik^2}, \quad \left(\frac{d\hat{A}_y}{dz} \right)_{l=0} = -\hat{B}_x, l=0 \quad (3.35)$$

$$\hat{A}_z, l=0 = 0, \quad \left(\frac{d\hat{A}_z}{dz} \right)_{l=0} = 0. \quad (3.36)$$

With these boundary values, we can integrate Eq. (3.32) and Eq. (3.33) and get the solution for \hat{A}_x, \hat{A}_y , and \hat{A}_z in all four layers. The vector potentials are given by the inverse Fourier transform. The curl of the vector potential well resembles the input magnetic field.

3.2.3.2 Time dependent update

The cartoon in Fig. 3.2 shows how the coronal model is driven by the flux emergence model. The physical quantities (converted into the variables of the coronal simulation) in the four horizontal layers from the flux emergence simulation are copied to the bottom of the coronal simulation (three ghost cells and the first cell in the computation domain).

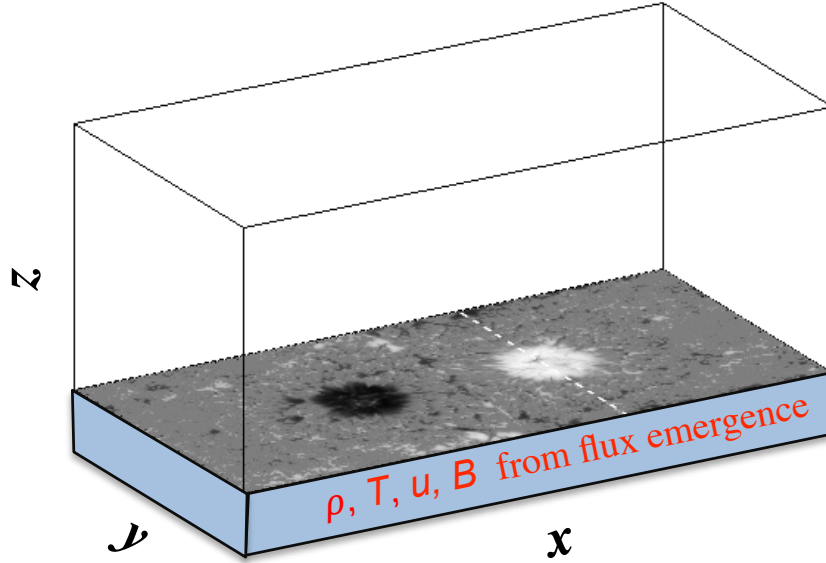


Figure 3.2: Cartoon showing the coupling of the flux emergence simulation and the coronal simulation. The image is the vertical magnetic field in the photosphere. The frame above the image present the computational domain of the coronal simulation, with x , y , z the coordinate axes. The blue cube is the bottom boundary (three ghost cells) of the coronal simulation. The physical quantities (ρ , T , \mathbf{u} and \mathbf{B} correspond to the density, temperature, velocity and magnetic field) in the bottom boundary is from the flux emergence.

The input from the flux emergence simulation has 1536×768 grid points. This data has to be reformed to the grid of the coronal simulation, i.e. 256×128 for the low resolution run and 1024×512 for the high resolution run. We use a nearest-neighbour method to interpolate the data in each horizontal layer.

The data from the flux emergence simulation has time cadence of 25 s, which is very sufficient to capture the evolution of plasma and magnetic structures in the photosphere. The boundary values for the coronal simulation at each time step (U_t) is calculated by a linear interpolation between two consecutive data sets of the flux emergence simulation, i.e.

$$U_t = U_L + \left(\frac{U_R - U_L}{t_R - t_L} \right) (t - t_L) \quad (3.37)$$

Here t is the time, U_L the first data set before the current time, U_R the first data set after the current time. t_L and t_R , which follow $t_L \leq t \leq t_R$, are for the two datasets, respectively.

At the beginning of the coronal simulation, the atmosphere is stratified in the vertical direction, but uniform in the horizontal direction. However, the input from the flux emergence simulation has already developed some density and temperature structures. The initial magnetic field in the coronal simulation is the potential field extrapolated from vertical magnetic field in the highest horizontal layer (i.e. $l=3$). But the magnetic field in the lower horizontal layers (i.e. $l=0$ to $l=3$) are not potential. Therefore, at the very

beginning of the coronal simulation, there is a considerable mismatch between the values copied from the flux emergence simulation and those set by the initial condition of the coronal simulation. We switch on the driver at the bottom in a time-dependent manner in the first 5 min of the coronal simulation. The values in the lowest cells (U_{init} , i.e. in the three ghost cells and the first cell in the computation domain) are set by

$$U_{\text{init}} = w U_0 + (1 - w) U_t, \quad (3.38)$$

where U_0 is the values defined by the initial condition, U_t defined by Eq. (3.37), and w the weight that decreases from 1 to 0 linearly in time in the first 5 min of the coronal simulation.

4 Coronal loops formed in an emerging solar active region

* Sect. 4.2 to Sect. 4.6 are Sect. 3 to Sect. 7 in the article *A model for the formation of the active region corona driven by magnetic flux emergence* by F. Chen, H. Peter, S. Bingert, and M. C. M. Cheung, published in *Astronomy & Astrophysics*, 564, A12 (2014), DOI: 10.1051/0004-6361/201322859. Reproduced with permission from Astronomy & Astrophysics, © ESO

4.1 Introduction

The primary goal of the coronal model is to investigate how the coronal structures (e.g. coronal loops) form during the emergence of the magnetic flux tube, and how well the model features match the real corona. Therefore, we first analyse the data of the low resolution run for the general properties of the coronal loop formed in the model. Here we focus on a time period of about 30 min when the first coronal loop becomes visible in the synthetic EUV images.

In this chapter we first give a detailed description on the first EUV loop formed during the flux emergence (Sect. 4.2). We then compare the thermal dynamics and energetic along the loop with the classical understandings from traditional 1D loop models (Sect. 4.3). The 3D nature of the loop, which is beyond the regime of 1D loop models, is highlighted in Sect. 4.4. Finally Sect. 4.5 discusses the enhancement of the energy input in the model photosphere that triggers the loop formation.

4.2 Coronal loops appearing in an emerging active region

4.2.1 Magnetic expansion into the corona

Driven by the magnetic flux emergence through the bottom boundary, the magnetic field expands into the corona. In Fig. 4.1 we show an overview of the evolution of the magnetic field in the coronal simulation over four hours. We select the fieldlines at an early stage of the simulation by random seeds in a small volume in the lower middle of the computational box and trace their evolution.¹ Thus the lines in the three lower panels of Fig. 4.1

¹The algorithm for fieldline tracing used by VAPOR with the results shown in Fig. 4.1 is described at <http://www.vapor.ucar.edu/docs/vapor-renderer-guide/flow-tab-field-line-advection>. It assumes that fieldlines are frozen in the plasma elements (i.e., infinite conductivity) everywhere and follows the motions of

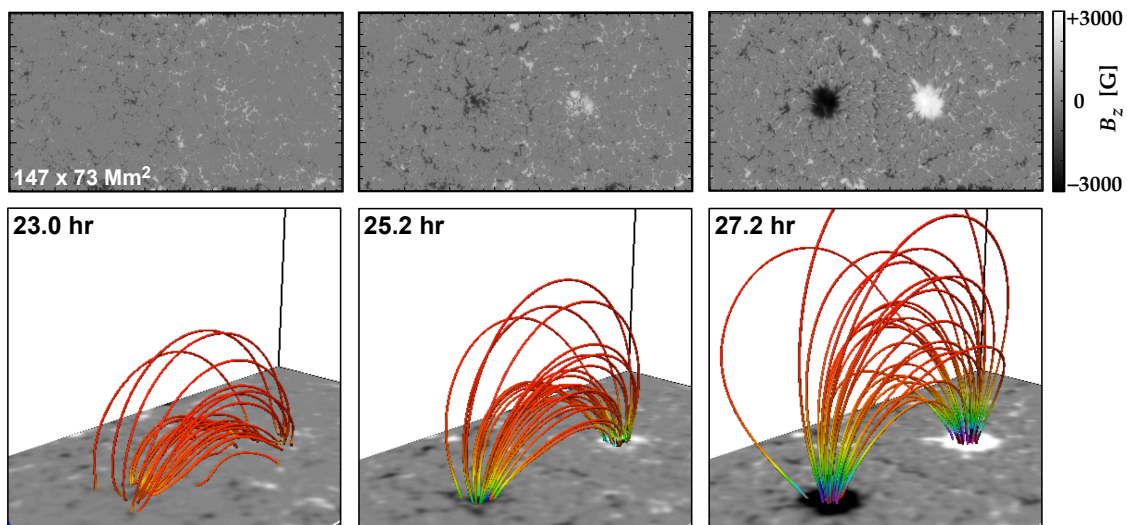


Figure 4.1: Overview of evolution of magnetic field. The top row shows the magnetogram at the bottom boundary in the photosphere at three different times (vertical magnetic field). The horizontal extent in the top panels is $147.5 \times 73.7 \text{ Mm}^2$. The bottom row shows the evolution of a group of magnetic fieldlines in the coronal model driven by the flux emergence. The color coding on the fieldlines shows the magnetic field strength (red is low and purple is high). The bottom of the 3D rendering boxes are the same magnetogram as the top row. The times in the panels refer to the time since the start of the flux-emergence simulation. See Sect. 4.2.1.

show the same set of fieldlines and how they evolve in time.

At 23.0 h, there are already lots of small-scale flux-concentrations in the photosphere. Low-lying fieldlines connect these small elements (not shown in the figure). As discussed in Cheung et al. (2010), these small flux concentrations are part of the flux tube brought to the surface through the near-surface convection. Because of the large scale of the emerging flux tube, the large-scale magnetic connections in the figure (at 23 h) show a bipolar pattern.

After two hours evolution at about 25.2 h, more magnetic flux emerged through the photosphere and the small-scale flux-concentrations begin to coalesce. Now the large-scale magnetic field concentrations start to become visible in the photosphere. This is also illustrated by the fieldlines whose footpoints are moving closer to each other now concentrating near the simulated spots. The magnetic field strength near the footpoints increases. At the same time, the fieldlines expand upward into the higher atmosphere.

After another two hours, around 27.2 h, a pair of simulated spots, where the magnetic field strength is over 3000 G, has formed in the photosphere. Now at the end of the coalescence process the footpoints of the fieldlines are bundled closely together. The central part of the set of fieldlines continues to expand into the higher corona.

The evolution of the magnetic field at the bottom boundary of our coronal model follows that in the flux emergence simulation, of course, albeit at a reduced spatial resolution. While most of the fine structures are lost due to the lower resolution, the photospheric

plasma elements. The influence of magnetic diffusivity is discussed in Sect. 4.3.

magnetic field still captures the formation of sunspots by coalescence of small (down to the resolvable scale) flux elements.

4.2.2 Appearance of a coronal loop

One of the key interests of this study is whether coronal loops will form during the active region formation. Here and in most of the cases in this paper the term *coronal loop* refers to a loop-like structure identifiable in (real or model-synthesized) EUV observations of the corona. Whenever we refer to the magnetic field that confines the plasma contributing to the EUV loop emission, we always use the term *magnetic tube*.

To perform a direct comparison between our model and observations, we synthesize EUV images using the AIA response function (Boerner et al. 2012), following the procedure of Peter and Bingert (2012). Here we concentrate at the AIA 193 Å channel. It looks similar but not identical to 171 Å and 211 Å channels, which sample the 1 to 2 MK plasma, too. The 193 Å and 211 Å channels have also contributions from cooler plasma, in particular in quiet regions. However, this does not play a major role in our active region (model).

To form a coronal loop visible in EUV, one has to bring up enough plasma into the upper atmosphere along a fieldline and heat it to at least 10^6 K. In our model, the heating is by dissipation of currents which are induced by braiding of magnetic fieldlines through photospheric motions. If the magnetic field strength in the photosphere is low, the plasma motion can braid the magnetic fieldlines efficiently, but the induced currents will be weak, too. On the other hand, the braiding does not work in very strong magnetic flux concentrations, because there the plasma motions are suppressed. Both moderately high magnetic field and horizontal velocity are needed to induce enough current. This favorable combination is found at the periphery of sunspots, and in particular in our model after some 25.5 h after the start of the flux-emergence simulation. Therefore all times (usually given in minutes) mentioned in the remainder of the paper will refer to this time, i.e., in the following $t=0$ refers to 25.5 h after the start of the flux emergence simulation.

Once the energy input into the corona is sufficient, EUV loops will start to form. In Fig. 4.2 we show the synthesized images for the AIA 193 Å channel integrated along the vertical and the horizontal coordinate at two different times 20 minutes apart. These views correspond to observations near the disk center (top panels) and at the limb (bottom panels). The left column shows a snapshot at $t=14$ min, just after the first EUV loop appears. At this time we see a single EUV loop forming, at later times more loops form at different places. Here we concentrate on the first single EUV loop in order to better isolate the processes triggering its formation.² The right panels of Fig. 4.2 show the coronal emission at $t=34$ min, after the loop started to fragment into several individual loops (see Sect. 4.4.2). From almost no emission to clearly detectable count rates in the synthesized images it takes only ≈ 5 min (see the animation with Fig. 4.2). In this paper we will mainly concentrate on the initial evolution of the loop system during about 15 min.

The EUV loop is rooted in the periphery of the simulated spots, which is clear from the top panels of Fig. 4.2 showing an overlay of magnetogram and emission. This is consistent with the long-known observation fact that the footpoints of coronal loops are not in the

²In a more recent not yet fully finished numerical experiment we see also multiple loops forming at this early stage, so the limited spatial resolution in this model plays a role, too.

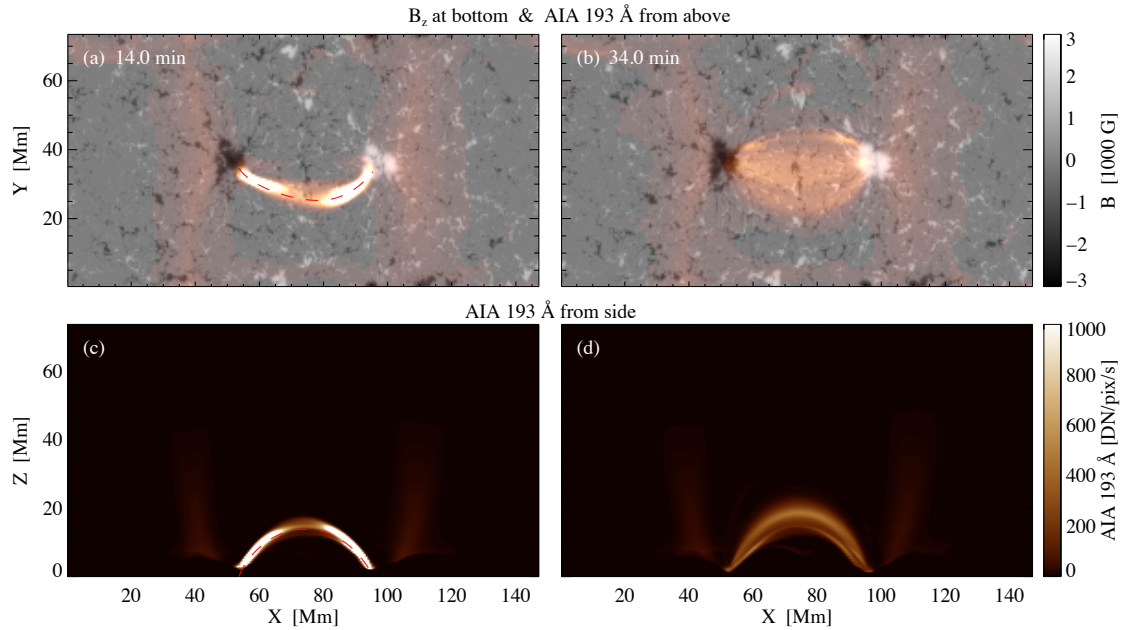


Figure 4.2: Evolution of synthesized coronal emission and magnetic field. The top panels show photospheric magnetograms (vertical component), overlaid with the synthesized coronal emission as it would be seen in the AIA 193 Å channel. The bottom panels show synthesized AIA 193 Å images as seen from the side. The synthetic emission is integrated along the line of sight, comparable to what is seen at disk center (top) or the limb (bottom). The two columns show snapshots from the simulation 20 minutes apart. Times refer to 25.5 h after the start of the flux-emergence simulation. The dashed line in the left panels shows the fieldline at the spine of the loop selected for the analysis in Sect. 4.3. See Sect. 4.2.2.

umbra at the higher field strengths, but in the periphery, the penumbra (Bray et al. 1991). Even though the flux emergence simulation does not contain a proper penumbra (Cheung et al. 2010) it is clear that the loops are rooted in a region where convection can do considerable work to the magnetic field in the photosphere (see Sect. 4.5) and thus induces strong currents in the corona.

The visible top of the EUV loop rises upwards by 10 Mm within 20 min, which means a 10 km s^{-1} average upward velocity of the apex. The cross section of the EUV loop expands in the vertical direction during this rise. However, the EUV loop expands even more strongly in the horizontal direction after its initial appearance as a relative thin tube of up to 5 Mm diameter and 45 Mm length. Finally the emission covers the whole area in-between the two simulated spots, with a few fragments in the relatively diffuse loop emission (Fig. 4.2b).

The above discussion, in particular the late fragmentation, shows that a 3D treatment of the loop formation is essential. Still, in the early phase, the loop evolution appears to be close to a single monolithic loop. Therefore, we first analyze the 1D evolution along the spine of the emerging loop in Sect. 4.3. The full 3D aspects and the trigger of the loop formation will be addressed after that in Sects. 4.4 and 4.5.

4.3 The 3D loop collapsed to one dimension

In the solar corona, the high electric conductivity prevents slippage of the fully ionized plasma across the field. The dominant magnetic energy assures that the Lorentz force determines motions perpendicular to the magnetic field. The anisotropic heat conduction quickly spreads the thermal energy along the fieldlines. Under such circumstances, often a simplified 1D model along a magnetic fieldline is sufficient to describe a coronal loop, although EUV loops are 3D structures in nature, as we show in this study.

In a 3D model, one can analyze the dynamics and thermal structures along a certain magnetic fieldline, which should then give results equivalent to that of a 1D loop model. For the loop forming in our 3D model, this applies in the early phase, when the loop is still confined to a thin magnetic tube. This assumption breaks down in the later phase, when the loop fragments into several substructures (see Sect. 4.4).

The spine of a EUV loop, which can be considered as being the central magnetic fieldline in the structure, is assumed to be static in most 1D models. However, it evolves in a self-consistent manner in 3D models. For 3D models of mature active regions (Gudiksen and Nordlund 2005a,b, Bingert and Peter 2011), the magnetic field evolution follows the shuffling of footpoints of the fieldlines by granular motions and the change in morphology is very gentle. It is quite different in our model. When the first coronal loop becomes visible, the flux emergence is still going on, and the coronal magnetic field changes dramatically. To analyze the evolution of an equivalent 1D model, we need to follow the magnetic fieldline in time and extract all physical quantities along this evolving fieldline.

During this tracing, we assume that magnetic fieldlines are frozen-in with the plasma elements, as it should be in the case of high electric conductivity. Although there is a constant numerical resistivity in the induction equation in our simulation, the typical diffusion speed over 10 Mm is on the order of 1 km s^{-1} , which is smaller than the typical velocities (perpendicular to B) associated with the expansion of the magnetic fieldlines. In practice, we first follow the motion of the plasma element at the apex of a magnetic fieldline, and then calculate the new fieldline passing through the new position of this plasma element.

4.3.1 Thermal structure and dynamics of the loop

We choose a fieldline along the spine of the loop seen in the AIA 193 Å image at $t=14$ min, when the loop is clearly defined (left panels of Fig. 4.2). In Fig. 4.3 we show a space-time diagram for this fieldline traced following the strategy above. The coordinate along the magnetic fieldline is normalized by the instantaneous length integrated between the two photospheric footpoints of the magnetic fieldline. During the time we investigate the evolution of the loop (approx. 14 min to 24 min) the fieldline at its spine lengthens by some 10% to 15%.

In the very early stage, the plasma along the fieldline is still cold and the pressure near the top is low. In this early phase ($t < 14$ min), there is some weak draining along the fieldline, due to the slow rise of the fieldline driven by the flux emergence.

At $t \approx 14$ min, Ohmic heating increases through the whole loop, and the coronal temperature quickly increases to over 1 MK (Fig. 4.3a, b). Here we analyze the temporal change in the heating, and discuss in Sect. 4.5 the self-consistent trigger of the increase

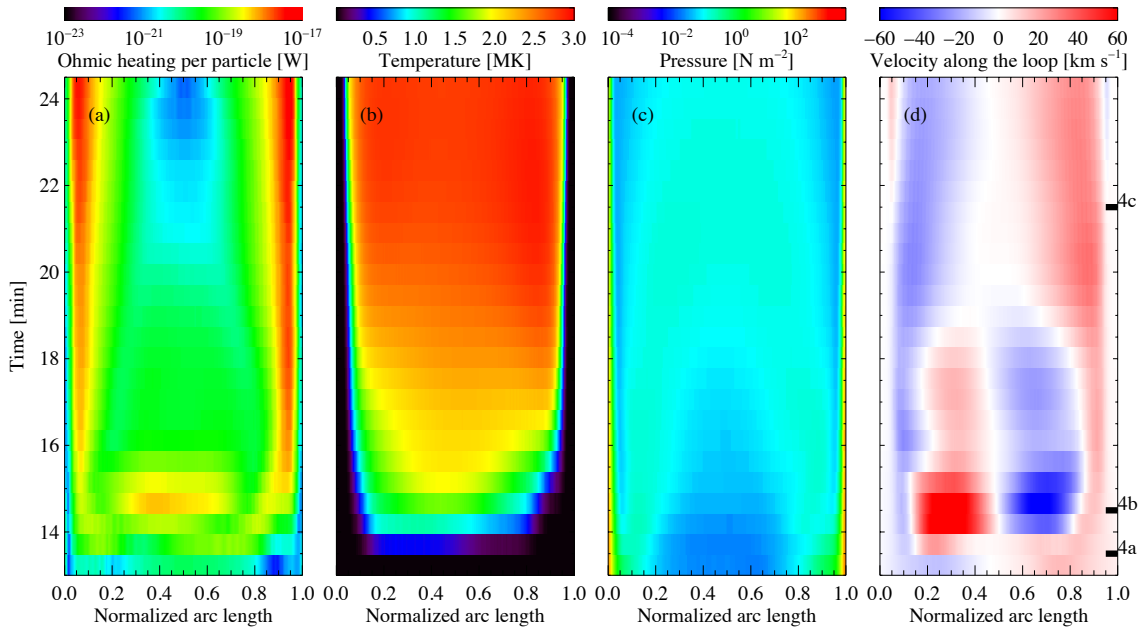


Figure 4.3: Space-time diagram of emerging loop. All properties are shown as functions of normalized arc length along the fieldline at the spine of the forming loop and time. Because the fieldline is followed in time, its length is changing and the arc length along the fieldline is normalized to the length at the respective time. The loop footpoints are at arclengths 0 and 1. In the velocity plot positive velocities (red) indicate a flow in the direction of arc lengths from 0 to 1 (“to the right”). In the color scale for the temperature green roughly corresponds to the peak contribution to the AIA 193 Å channel. The marks 4a, 4b, and 4c in the right panel indicate the times shown in the three panels of Fig. 4.4. See Sect. 4.3.1.

of the heating rate in the 3D model. Very efficient heat conduction along the loop ensures an almost constant temperature along the fieldline in the coronal part (Fig. 4.3b). At the same time, the heat conduction transfers the energy deposited in the corona down to the cold dense chromosphere and induces an evaporation upflow (Fig. 4.3d). This flow fills the loop with plasma as is reflected by the increase of loop pressure in the Fig. 4.3c.

On the particular fieldline we analyze here, the plasma starts to increase its temperature at around $t=14$ min. On other fieldlines (reaching slightly greater apex heights) the heating sets in earlier. Thus some emission in the AIA 193 Å channel can be seen already before $t=14$ min.

In a later stage ($t>16$ min), the Ohmic heating drops and the filling of the loop gradually ceases (Fig. 4.3a, d). The pressure gradient at this moment is not sufficient to balance gravity and thus to maintain an equilibrium. As a result, the plasma starts to drain, as demonstrated by the downflows in Fig. 4.3d after $t\approx 20$ min. The loop temperature, which is over 2.5 MK after $t\approx 19$ min, is maintained for a long time. This is consistent with the long cooling times for these high temperatures (Klimchuk 2006), which is about 30 min. The energy evolution of the loop is further analyzed in detail in Sect. 4.3.2.

There is a local pressure peak in the lower part on each side of the loop from $t=13.5$ min to 18 min. These peaks result in both upward and downward pressure gra-

dient forces, which drive the flows to the loop top and the loop feet. The temperature of the downflow is 10^4 K to 10^5 K, which corresponds to transition region temperatures; that of the upflow is 10^6 K, which corresponds to coronal temperature. This would cause the transition region lines (formed below 0.5 MK) to be redshifted and the coronal lines to be blueshifted. Thus, this is consistent with observations (Peter 1999, Peter and Judge 1999) and in line with processes found by Spadaro et al. (2006) in 1D models and by Hansteen et al. (2010) in 3D models.

4.3.2 Energetics in the emerging loop

To investigate the energy budget controlling the thermal structure of the loop and its dynamics we derive the governing equation of the evolution of the energy along a (field) line that moves with the velocity perpendicular to the line itself, with the following assumptions.

1. *Constant cross section.*

\mathbf{B} is invariant along the magnetic tube, which is the same as to say that the loop has a constant cross section. Therefore, the unit vector of the magnetic field, \mathbf{b} , satisfies

$$\nabla \cdot \mathbf{b} = \frac{1}{|\mathbf{B}|} \nabla \cdot \mathbf{B} + \mathbf{B} \cdot \nabla \frac{1}{|\mathbf{B}|} = 0.$$

2. *No compression perpendicular to the loop.*

The velocity is decomposed into $u_{\parallel} \mathbf{b} + u_{\perp} \boldsymbol{\delta}$, with the parallel $u_{\parallel} = \mathbf{u} \cdot \mathbf{b}$, the perpendicular component $u_{\perp} = |\mathbf{u} - u_{\parallel} \mathbf{b}|$. Here \mathbf{b} is the unit vector of the magnetic field, and $\mathbf{b} \cdot \boldsymbol{\delta} = 0$. We assume the magnetic tube is not compressed by the flows in the perpendicular direction, which implies $\nabla \cdot (u_{\perp} \boldsymbol{\delta}) = 0$. This assumption is appropriate for a rigid 1D loop model, although it is not the case in our 3D simulation.

3. *Heat conduction parallel to the loop.*

The heat flux is along the magnetic field, i.e., $\mathbf{q} = q_{\parallel} \mathbf{b}$. Because B is invariant along the magnetic tube,

$$\nabla \cdot \mathbf{q} = \mathbf{b} \cdot \nabla q_{\parallel} + q_{\parallel} \nabla \cdot \mathbf{b} = \mathbf{b} \cdot \nabla q_{\parallel}.$$

These assumptions are consistent with traditional 1D loop modeling. They do not fully hold in the 3D loop we find in our numerical experiment, but are appropriate for the purpose of the comparison made in Sect. 4.3.

In general, the conservation of thermal energy is written as

$$\frac{\partial e_{\text{th}}}{\partial t} = -(\mathbf{u} \cdot \nabla) e_{\text{th}} - \frac{\gamma}{\gamma - 1} p (\nabla \cdot \mathbf{u}) + Q - L - \nabla \cdot \mathbf{q}. \quad (4.1)$$

With the above assumptions this energy budget can be rewritten as

$$\begin{aligned} \frac{\partial e_{\text{th}}}{\partial t} = & -u_{\parallel} (\mathbf{b} \cdot \nabla) e_{\text{th}} - u_{\perp} (\boldsymbol{\delta} \cdot \nabla) e_{\text{th}} - \frac{\gamma}{\gamma - 1} p \left[\nabla \cdot (u_{\parallel} \mathbf{b}) + \nabla \cdot (u_{\perp} \boldsymbol{\delta}) \right] \\ & + Q - L - \mathbf{b} \cdot \nabla q_{\parallel}. \end{aligned} \quad (4.2)$$

Here e_{th} is the thermal energy per unit volume, following $e_{\text{th}} = p/(\gamma - 1)$. p is the plasma pressure. L denotes the radiative losses through optically thin radiation, and $q_{\parallel} = -\kappa_0 T^{5/2}(\mathbf{b} \cdot \nabla T)$ is the heat flux along the magnetic field.

$$\frac{\partial e_{\text{th}}}{\partial t} = -u_{\parallel}(\mathbf{b} \cdot \nabla) e_{\text{th}} - u_{\perp}(\boldsymbol{\delta} \cdot \nabla) e_{\text{th}} - \frac{\gamma}{\gamma - 1} p(\mathbf{b} \cdot \nabla) u_{\parallel} + Q - L - \mathbf{b} \cdot \nabla q_{\parallel}. \quad (4.3)$$

We move the term related to $u_{\perp}\boldsymbol{\delta}$ to the left-hand side of the equation and define

$$\left(\frac{\partial e_{\text{th}}}{\partial t}\right)_s = \left[\frac{\partial e_{\text{th}}}{\partial t} + u_{\perp}(\boldsymbol{\delta} \cdot \nabla) e_{\text{th}}\right]. \quad (4.4)$$

This can be considered as a type of material derivative.

With this the energy budget reads,

$$\left(\frac{\partial e_{\text{th}}}{\partial t}\right)_s = \underbrace{-u_{\parallel}(\mathbf{b} \cdot \nabla) e_{\text{th}}}_{(1)} - \underbrace{\frac{\gamma}{\gamma - 1} p(\mathbf{b} \cdot \nabla) u_{\parallel}}_{(2)} + \underbrace{Q}_{(3a,3b)} - \underbrace{L}_{(4)} - \underbrace{\mathbf{b} \cdot \nabla q_{\parallel}}_{(5)}. \quad (4.5)$$

Energy is added through $Q = Q_{\text{Ohm}} + Q_{\text{visc}}$, with the Ohmic heating (3a) $Q_{\text{Ohm}} = \eta\mu_0 j^2$ and viscous heating (3b) $Q_{\text{visc}} = 2\rho\nu\mathbf{S}^2$, where \mathbf{j} is the current and \mathbf{S} is the rate-of-strain tensor. In an equilibrium model, the time derivative and velocity would vanish, and the energy would be balanced between heating (3), radiative losses (4) and heat conduction (5). In our time-dependent 3D model, the loop never reaches an equilibrium. The advection of thermal energy along the loop is given by term (1) and the compressional work (combined with the change in e_{th} due to the compressibility of the plasma) by term (2) in the above equation.

In the following, we discuss the energy budget along the same fieldlines as in Sect. 4.3.1 before, during, and after the loop formation. For this we concentrate on the times $t=13.5$ min, 14.5 min, and 22.0 min which are indicated in Fig. 4.3 by the marks 4a, 4b, and 4c, which refer to the respective panels in Fig. 4.4 showing the terms (1) to (5) in the energy budget along the fieldline.

4.3.2.1 Initiation phase

In this early stage, there is a weak siphon flow in the loop (Fig. 4.3d), which is probably driven by the stronger heat input near the left footpoint. Because the loop is cool ($T < 5 \times 10^4$ K), the heat input is more or less balanced by radiative losses (Fig. 4.4a). At this time the loop would be invisible in EUV images with count rates below the sensitivity (of AIA observations). But at this moment, the Ohmic heating starts to increase. Although at the normalized arc length of 0.3 viscous heating is of the same magnitude as Ohmic heating, it is in general lower than Ohmic heating by at least one order of magnitude. Thus the increase of Ohmic heating is the primary cause of loop formation.

4.3.2.2 Formation phase

At $t=14.5$ min, the Ohmic heating is high in the middle part of the fieldline, giving rise to the loop formation. Within less than a minute, the Ohmic heating rate has risen to a

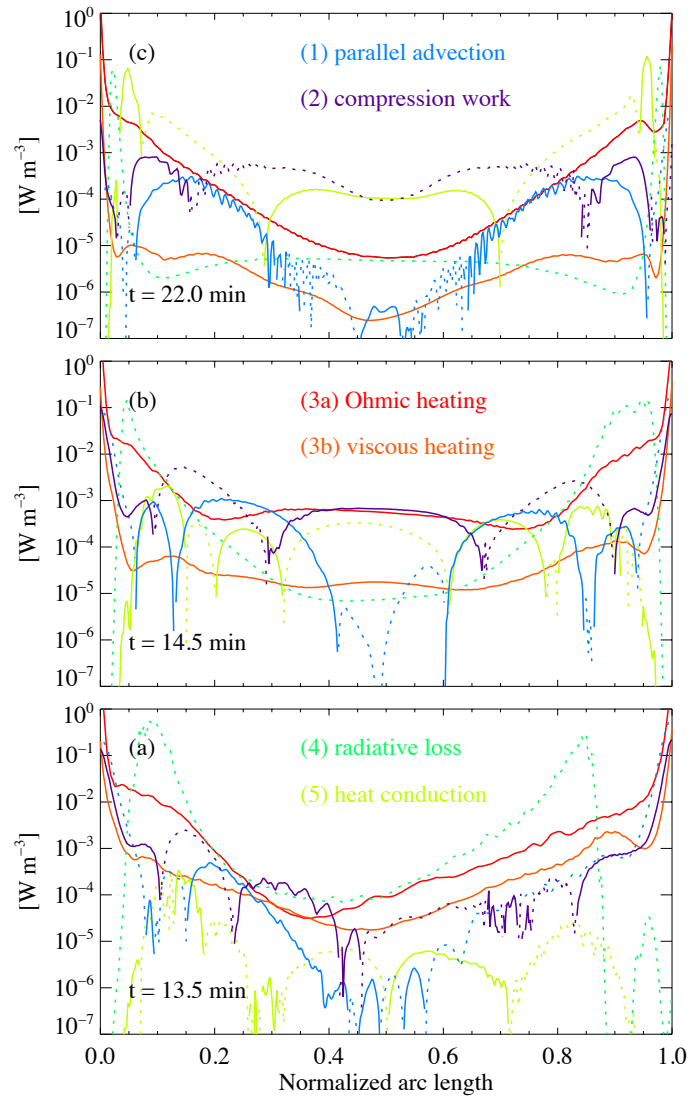


Figure 4.4: Energy budget along the loop at three different times. The panels show snapshots during the phases of initiation (a), formation (b), and cooling (c) at the time given with each panel. These times are indicated to the right of Fig. 4.3d by the marks 4a, 4b, and 4c. The terms in Eq. (4.5) are shown accordingly to the labels in the plots, the numbers correspondingly to those in Eq. (4.5). The line colors follow the same definition in all panels. Dashed lines indicate negative, solid lines positive values. The arc lengths are normalized, with 0 and 1 corresponding to the two footpoints of the fieldline in the photosphere. See Sect. 4.3.2.

roughly constant level of almost 10^{-3} W m^{-3} in the hot coronal part (Fig. 4.4b). Considering that the coronal part covers 20 Mm to 30 Mm along the loop, this implies an energy flux of $\approx 10^4 \text{ W m}^{-2}$ into the loop, which would be consistent with estimates for coronal heating in active regions derived from observations (Withbroe and Noyes 1977).

The Ohmic heating rate in other 3D MHD models (Gudiksen and Nordlund 2005a,b, Bingert and Peter 2011) drops (on average) exponentially with height, which is also true when following individual fieldlines (van Wettum et al. 2013). These previous models were describing a mature active region with a relatively stable magnetic configuration in which the footpoints are shuffled around. In contrast, in the present model the emerging magnetic field rises into the corona. Thus the interaction between the rising magnetic fieldlines hosting the loop and the ambient magnetic field also contributes to the currents along the loop, so that the Ohmic heating rate is quite constant along the loop (Fig. 4.4b). The viscous heating is almost two orders of magnitude lower, so that the Ohmic heating dominates the energy input.

The heat conduction term is negative near the apex, i.e., it transports the energy added by the Ohmic heating to the lower part of the loop. Ultimately, the energy is radiated close to the footpoints where the temperature is low.

The advection term at normalized arc lengths of 0.15 to 0.3 (and symmetric on the other side of loop) demonstrates the evaporation upflow filling the loop (Fig. 4.3d). This converging flow towards the loop top provides compressional work adding energy near the loop apex. This compressional work nearly equals the Ohmic heating at the loop top.

The effect of all contributions, i.e., the right-hand side of Eq. (4.5), is positive. This leads to a net rise of $\partial e_{\text{th}}/\partial t$ on the order of $e_{\text{th}}/\tau \approx 10^{-3} \text{ W m}^{-3}$ (see Fig. 4.4b). In the coronal part of the loop the number density is about $n \approx 10^9 \text{ cm}^{-3}$. Therefore the required increase of the energy $e_{\text{th}} = \frac{3}{2}nk_{\text{B}}T$ to reach coronal temperatures of about $T \approx 10^6 \text{ K}$ is on the order of $\tau \approx 1 \text{ min}$. This time is compatible with the synthesized images, in which we see the loop forming in a matter of minutes (see animation attached to Fig. 4.2).

In their 2D study Hurlburt et al. (2002) implicitly assumed that the corona adjusts instantly to changes in the heat input because they employ a series of (static) equilibrium models. Here we see that the timescale for the evolution of the loop (minutes) is comparable to the timescale of the energy injection from the photosphere through the Poynting flux (see also Sect. 4.5). Thus one has to account for the evolution of the thermal properties in a dynamic model.

4.3.2.3 Cooling phase

After the heating ceases the loop enters a slow cooling phase (Fig. 4.4c). Owing to the drop of Ohmic heating, the plasma pressure falls, the plasma loses its support, and the loop drains. Consequently, decompression is the dominating cooling agent at the apex, as is illustrated by the negative contribution of the compression work throughout the top half of the loop (Fig. 4.4c). Along with the draining, advection transports energy from the loop top to the lower parts. In this late phase the dominant heating of the apex is due to heat conduction from the sides. Potentially, such situations can lead to a loss of equilibrium and catastrophic cooling (Müller et al. 2003, 2004), which we do not observe here because the heating is not concentrated strongly enough towards the footpoints.

In 3D models with a more stable magnetic field configuration, the loop can reach a

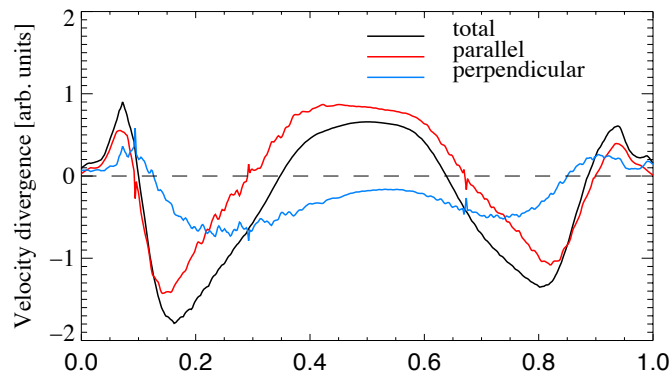


Figure 4.5: Divergence of velocity along the loop at $t=14.5$ min during the loop formation phase. The total divergence $-\nabla \cdot \mathbf{u}$ is shown in black, the parallel component in red, and the perpendicular component in blue. The arc length along the fieldline is normalized to the loop length. See Sect. 4.3.2.4.

(quasi-) equilibrium state, and remain stable for a longer time (Peter and Bingert 2012). In our model, the magnetic field is expanding due to the flux emergence. Thus the loop cannot reach a (quasi-) equilibrium state and remains a transient feature evolving fast on a timescale of much less than 30 min (see animation with Fig. 4.2). This is underlined by the fact that the main cooling agent (in the top part) is decompression of the plasma driven by the expansion of the magnetic field.

4.3.2.4 Perpendicular compression

A static rigid 1D loop model only accounts for the compression work from velocity parallel to the magnetic fieldline. However, the compression or expansion perpendicular to the fieldline contributes to the thermal energy density in a 3D model, in particular, if the loop is expanding and interacting with the ambient magnetic field, as it is the case here.

To evaluate the role of the perpendicular compression, we split the divergence of the velocity, $\nabla \cdot \mathbf{u}$, into its parallel component ($(\mathbf{b} \cdot \nabla) u_{\parallel}$) and its perpendicular component. The latter is evaluated by $\nabla \cdot \mathbf{u} - (\mathbf{b} \cdot \nabla) u_{\parallel}$. Figure 4.5 shows these contributions at $t=14.5$ min, i.e., during the loop formation phase. For consistency with Fig. 4.4 we plot $-\nabla \cdot \mathbf{u}$. A positive value in Fig. 4.5 implies convergence/compression, and a negative one implies divergence/expansion. Near the loop top, the parallel contribution shows a converging pattern, because evaporation flows from loop footpoints meet at the loop top (cf., Fig. 4.3). In contrast, the perpendicular contribution shows a diverging pattern at the top. This is corresponding to the expansion of the magnetic tube which will be discussed in Sect. 4.4.1. Still, the net effect is a compression of the plasma. In the lower part of the loop the total divergence is basically determined by the parallel contribution.

Although the perpendicular divergence has non-negligible contribution throughout the loop, the profile of the total divergence mostly follows that of the parallel contribution. This suggests that the 1D description of the flow in the loop is still acceptable at this stage. However, later the loop shows a clear 3D nature, which is discussed in the next section.

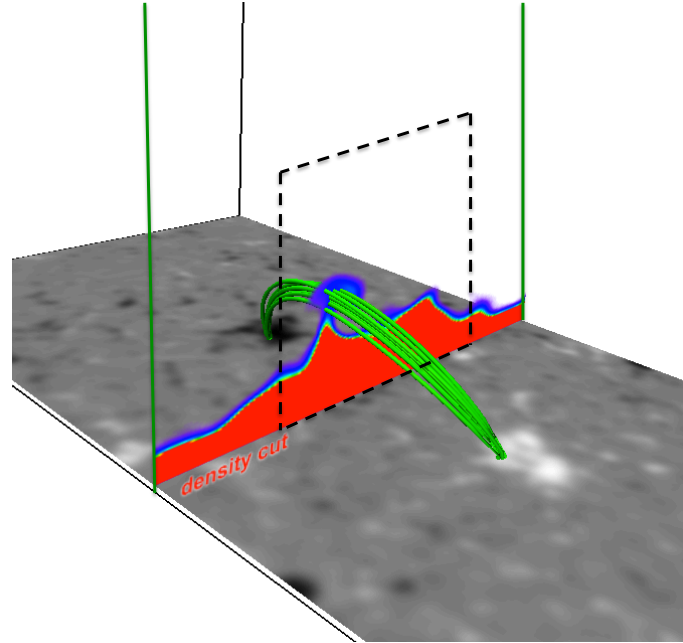


Figure 4.6: 3D Visualization of the location of the bright loop at time $t=14$ min. The green lines show the fieldlines roughly outlining the volume of the first bright loop appearing in the simulation. The bottom plane shows the vertical component of the photospheric magnetic field. A density cut in the vertical plane halfway between the footpoints of the loops perpendicular to the loop is indicated by the large green square. On this cut red indicates chromospheric densities, and blue enhanced coronal densities of about 10^9 cm^{-3} . Lower densities in the corona are transparent. The black square in dashed line on the midplane indicates the field of view in Fig. 4.8. See Sect. 4.4.

4.4 The 3D nature of the loop

4.4.1 Evolution of the magnetic envelope

To study the magnetic envelope of the EUV loop seen in the synthesized 193 \AA images, we investigate the evolution of a magnetic tube that is (at one particular time) roughly co-spatial with the volume of the EUV loop. We define the magnetic tube based on a *vertical* cut perpendicular to the loop plane in the middle between the two sunspots ($x=73 \text{ Mm}$) at the time $t=14$ min (see Fig. 4.6). On this plane, we choose several points roughly enclosing the cross section of the synthesized AIA 193 \AA loop as starting points to follow magnetic fieldlines. This set of fieldlines defines the magnetic tube that we study further. We follow the magnetic tube in time by the same method as used in Sect. 4.3 and investigate the evolution of the cross section of the tube in the vertical midplane between the loop footpoints (large green square in Fig. 4.6).

We depict the temporal evolution of the cross section of the magnetic tube in the vertical midplane in Fig. 4.7. The magnetic tube moves upward as a whole and the cross section is significantly deformed. From $t=14$ min to $t=22$ min the cross section contracts in the vertical direction and expands significantly in the horizontal direction. This ap-

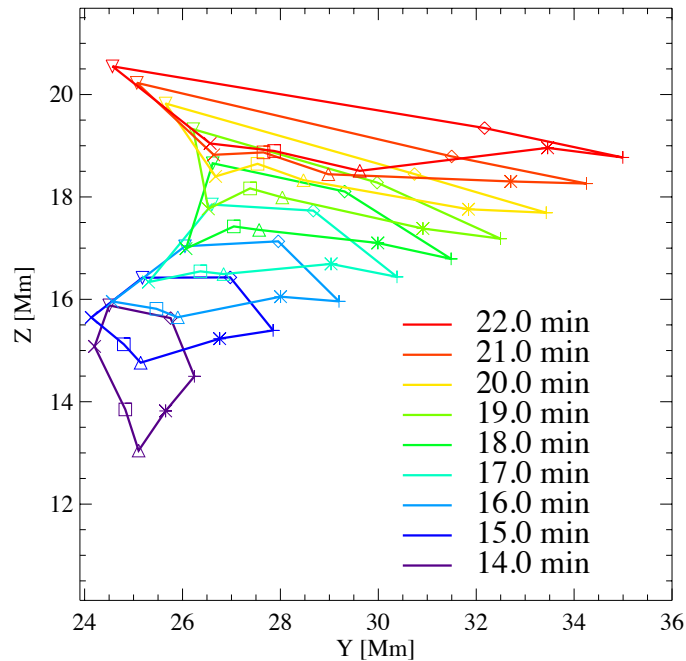


Figure 4.7: Evolution of cross section of the magnetic tube roughly encompassing the loop appearing in the synthesized AIA 193 Å images (cf. Fig. 4.2). The symbols show the positions of the fieldlines used to define the magnetic tube in the vertical midplane between the loop footpoints (cf. green square in Fig. 4.6). The same symbols indicate the same fieldline at the times color coded according to the legend. See Sect. 4.4.1.

pearance of the magnetic tube is consistent with the rise of the synthesized AIA 193 Å loop spine in the vertical direction and its significant horizontal expansion (see Fig. 4.2 and attached animation). An oblate shape of flux tubes was recently also reported by Malanushenko and Schrijver (2013) who analyzed the cross section of thin flux tubes in a potential field model. They found that the cross section is distorted for the end-to-apex mapping. That the magnetic tubes in the corona will be non-circular in cross section has already been reported before (Gudiksen and Nordlund 2005b).

4.4.2 Fragmentation of the loop

In Fig. 4.2 (and the attached animation) one can see that the synthesized AIA 193 Å loop is a thin bright structure at the early stage, and then expands. The single bright loop breaks into several individual strands, which is best seen in the top view of the box (Fig. 4.2b). We use the term *fragmentation* for this process. Inspecting the temporal evolution in the movies attached to Fig. 4.2 it is clear that this fragmentation means that the original loop fades and new fragments or strand continuously form and dissolve, giving the overall impression of a fragmentation. So this fragmentation is not to be understood in a way as a piece of wood would splinter, but as a coming and going of strands in a growing envelope.

To investigate this process, we show in Fig. 4.8 vertical cuts through the box in the midplane between the two footpoints. This midplane is roughly perpendicular to the loop

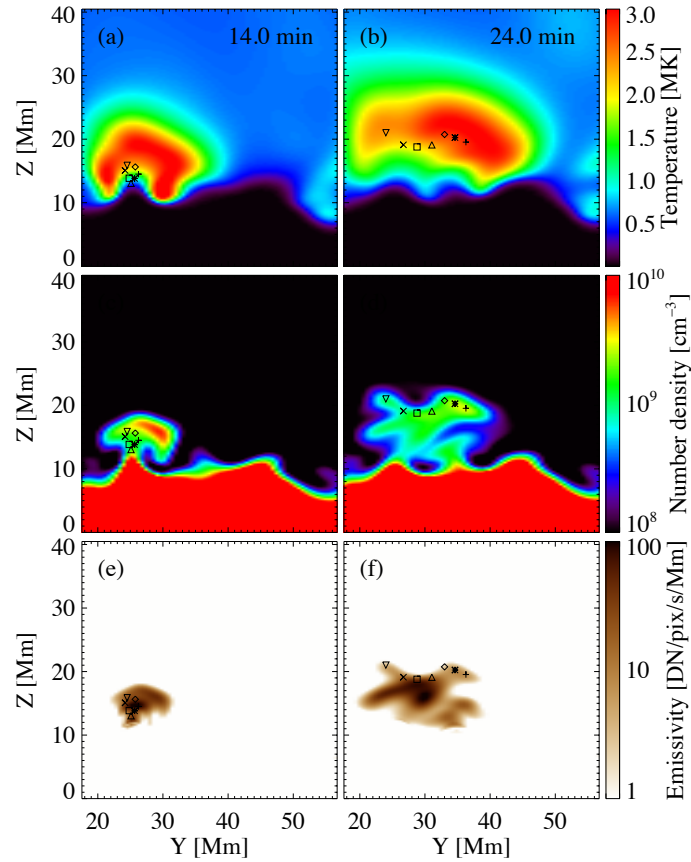


Figure 4.8: Temperature, density and synthesized AIA 193 Å emission in a vertical mid-plane between the loop footpoints (cut at $x=73$ Mm). The left and right column show snapshots 10 min apart at the times indicated in the top panels. In the temperature plots green roughly represents the temperature of maximum contribution to the 193 Å channel. The black symbols indicate the cross section of the magnetic tube discussed in Sect. 4.4.1 and Fig. 4.7. The field of view roughly matches the black square in dashed line in Fig. 4.6. See Sect. 4.4.2.

(same plane as discussed above, cf. Fig. 4.6). The fragmentation of the loop is visible in the coronal emission emerging from this plane (bottom row of Fig. 4.8). At the later stage (Fig. 4.8f) individual patches of AIA 193 Å emission have formed that would correspond to individual strands of the larger envelope.

To understand this EUV loop fragmentation we have to investigate the temperature and density structure in the vertical plane. For this we show in Fig. 4.8 also the temperature (top) and density (middle) in the vertical midplane. During the 10 min between the two snapshots shown in the left and right column, the temperature and density structures move upward, and expand horizontally. The density structure looks less smooth than the temperature which is in part because of the draining and filling of the corona.

The 193 Å emissivity (bottom row) is the product of the density squared and the temperature response function for that channel (Boerner et al. 2012). The latter largely (but not only) reflects the contribution function of Fe XII, which is strongly peaked with a maximum near 1.5 MK. In effect, the strong 193 Å emission originates from locations where the density is high and the temperature is near the peak of the response function for this particular channel. Consequently, the 193 Å emission pattern is neither cospatial with the density nor with the temperature structure, as is also clear from comparing the panels in the right column of Fig. 4.8 at the later time. The emission structure appears to be much more fragmented than both the temperature and density structure. This is simply because the density and temperature structures are not cospatial, and thus the convolution of the (smooth) density and temperature structures leads to the more clumpy coronal 193 Å emission. The same is also true for the other AIA coronal channels, which we do not show here.

We note that we find in this work a temperature gradient perpendicular to the loop spine with an increasing temperature with height (from about $z=14$ Mm to 22 Mm). This is similar to the model of Peter and Bingert (2012) who proposed a new mechanism to explain the constant cross section of coronal loops. Thus some parts of the high density structure at higher temperatures are cut off by the temperature response (or contribution) function, and in EUV emission the loops look as if having a constant cross section, even though the plasma loop, i.e., the density structure, expands along the loop, or more precisely, with the magnetic tube. Even though we do not investigate this further in detail here, the 193 Å loop shown in Fig. 4.2 from the side has roughly constant cross section. This is based on the same process as outlined by Peter and Bingert (2012).

4.5 What triggers the loop formation?

The appearance of the model corona is compatible with EUV observations in the sense that a clearly distinguishable loop forms in the synthesized images. The question remains why the loop forms at that particular time and position. We investigate this by checking the energy input into the loop which is given through the Poynting flux, $\tilde{\mathbf{S}} = (\eta\mathbf{j} - \mathbf{u} \times \mathbf{B}/\mu_0) \times \mathbf{B}$. Near the bottom boundary, the driving by the photospheric convective motions from the flux-emergence model induces strong currents, which are mainly confined to the bottom layers. The amplitude of the resistive term, $\eta\mathbf{j}$ drops very fast with height and becomes much smaller than the $\mathbf{u} \times \mathbf{B}/\mu_0$ term, in particular in the area near the simulated spots. Thus when studying the energy input into the coronal part

of the loop it is sufficient to investigate the $\mathbf{u} \times \mathbf{B}$ part alone,

$$\mathbf{S} = -\frac{1}{\mu_0} (\mathbf{u} \times \mathbf{B}) \times \mathbf{B} . \quad (4.6)$$

In Fig. 4.9 we show the vertical component of the Poynting flux \mathbf{S} in horizontal slices at three heights, from the photosphere ($z=0.32$ Mm) to the coronal base ($z=2.02$ Mm). There is a clear enhancement of the upward-directed Poynting flux surrounding the sunspot areas forming sort of a ring around the sunspot (green in Fig. 4.9 for $z=0.32$ Mm). This enhancement is at least a factor of five to ten with respect to the surrounding quiet Sun area or the center of the sunspot. In the former the magnetic field is too weak, in the latter the strong magnetic field suppresses the horizontal motions, so that in these regions no considerable upward directed Poynting flux can be found. This is consistent with the widely known observational fact that coronal loops in EUV and X-rays do not originate from the center of sunspots where the magnetic field is the strongest, but from the periphery of sunspots, i.e., the outer parts of the penumbra. In our model this is reflected by the fact that only in the periphery is the upward Poynting flux significantly enough to power coronal loops.

At the *coronal base* ($z=2.02$ Mm) the Poynting flux has the strongest enhancement near both footpoints of the loop, being typically another factor of about three higher than in the already enhanced region in the sunspot periphery. In Fig. 4.9, this shows up as the red spots in the panel for $z=2.02$ Mm. However, in the photosphere ($z=0.32$ Mm) only the right footpoint shows an enhancement of the Poynting flux, but not the left one. A closer inspection at the bottom boundary shows that this enhancement near the right footpoint in the *photosphere* is due to small magnetic flux elements which are advected by the convective motions into the strong magnetic field of the sunspot. These magnetic flux elements have sizes of ≈ 3 Mm, which is the scale of energy input into the loop and is not too far from the smallest resolvable scale in this model.

We miss a lot of the small-scale motions and fine magnetic structures in the photosphere when we map the original flux-emergence simulation to the grid of the coronal simulation (see Sect. 3.2.3). This can have two consequences. First, the energy input into the corona in our model is reduced, because we miss the Poynting flux on these smaller scales, at most this is a factor of two. Because the temperature scales with the energy input to the power of $2/7$ (Rosner et al. 1978), this would have only a minor impact on the temperature, but it might be that the coronal density in our model is too low by up to a factor of 2 in some places. Second, the higher spatial resolution in the photosphere, properly resolving granulation, will give rise to finer structures in the corona, too. These conclusions are supported by the preliminary results from a high-resolution numerical experiment.

To further investigate the vertical Poynting flux at the footpoints of the loop we study the temporal variation of the vertical Poynting flux in different heights along the loop. We do this in terms of averages in a small horizontal section around the loop as indicated by the rectangles in Fig. 4.9. The sizes of the rectangles are slightly different for the left and right footpoints and for different heights in order to best capture the Poynting flux enhancement. The positions of the rectangles are fixed in time. The resulting averages as a function of time are plotted in Fig. 4.10.

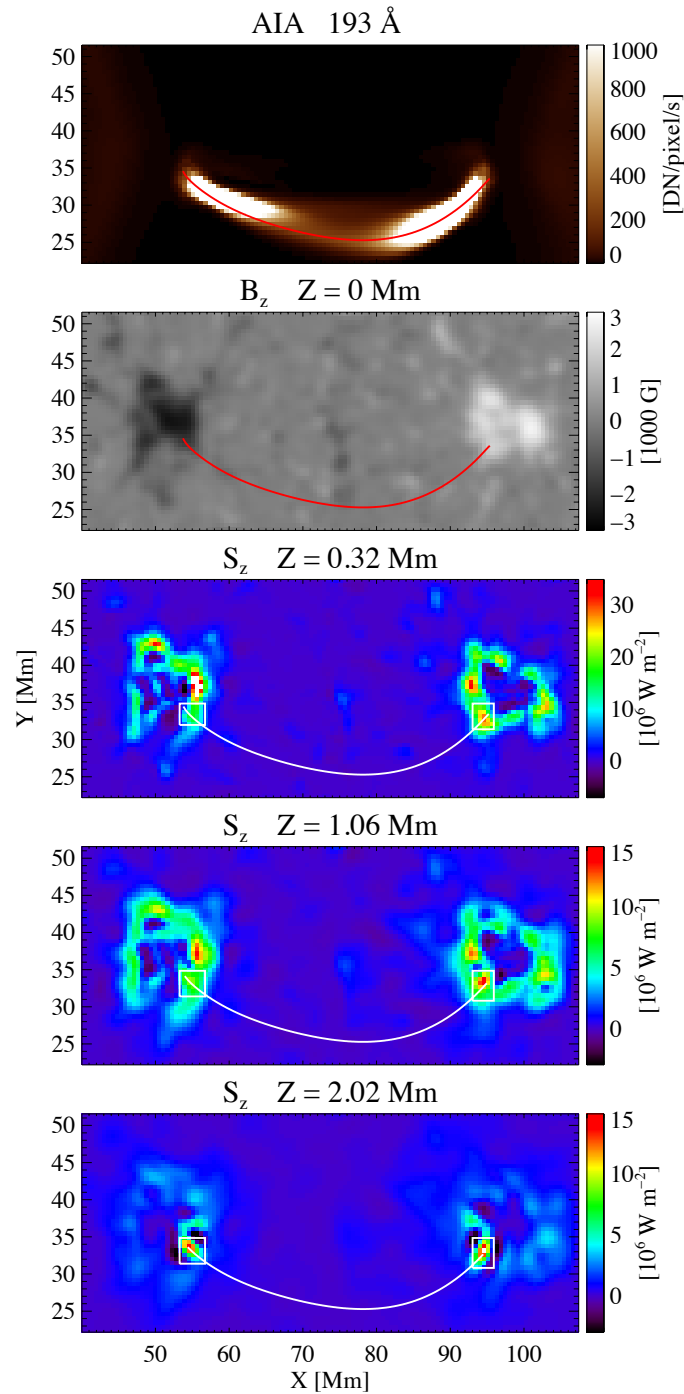


Figure 4.9: Zoom into the emerging active region at $t=14$ min. The top two panels show the synthesized AIA 193 \AA emission integrated along the vertical and the magnetic field, B_z , at the bottom boundary. The lower three panels show the vertical component of the Poynting flux, S_z , at three heights. The red and white lines indicate the same magnetic fieldline at the spine of the loop as shown in Figs. 4.2. The white boxes around both footpoints in the lower panels indicate the regions where we calculate the average vertical Poynting flux in Fig. 4.10.

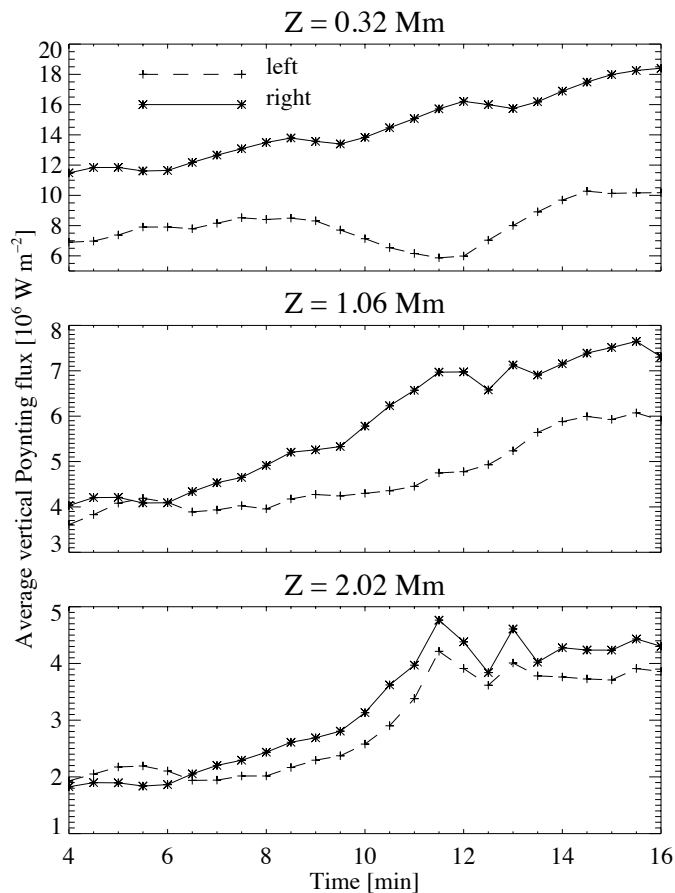


Figure 4.10: Temporal evolution of the vertical Poynting flux at the loop footpoints at three different height from the surface (top panel) to the coronal base (bottom panel). Here we show the averages in horizontal regions around the fieldline indicated in Fig. 4.9 by the respective boxes. The dashed lines are for the left footpoint, and solid lines are for the right footpoint.

At $z=0.32$ Mm, the vertical Poynting flux at the right footpoint (solid) increases significantly by more than 6 MW/m^2 during the 12 min shown in the plot around the time the loop appears (Fig. 4.10). A Fourier analysis clearly shows that this increase is modulated with a timescale of about 4 min, which is close to the 5-minutes oscillations in the photosphere and close to the lifetime of granules. In contrast, the left footpoint shows no significant increase over time, but only the granulation modulation. That the left and the right footpoint show a different behavior in the *photosphere* is not surprising, because in the flux emergence simulation these two footpoint regions, which are located in the different sunspots, evolve independently.

The situation is different higher up in the atmosphere. At $z=1$ Mm and 2 Mm both footpoints show a significant increase, with the the right footpoint preceding the rise of the left footpoint at both heights.

Based on the timing shown in Fig. 4.10 one can sketch the following scenario. At the *right* footpoint in the low photosphere the upward Poynting flux is increasing because of

the near-surface convection driven by the flux emergence simulation. This disturbance of the field then travels upward through the high-plasma- β region and can be seen in the upper photosphere near $z=1$ Mm and further propagates upward to the coronal base at $z=2$ Mm, where plasma- β is below unity. Here we can see a steeper rise after the magnetic stresses have been built up slowly from below. We also see a clear rise on the *left* footpoint at the coronal base at $z=2$ Mm. However, this increase lags behind the rise in the *right* footpoint by some 30 s, which is close to the Alfvén crossing time (with a loop length above $z=2$ Mm of about 40 Mm and an average Alfvén speed of about 2000 km/s in the coronal part). This underlines that the magnetic disturbance travels from the right coronal base to the left coronal base and triggers there a perturbation, that in the end leads to an increased Poynting flux also on the left side. From the left footpoint at $z=1$ Mm we can see that this disturbance can penetrate a bit into the high- β region, but cannot reach all the way down into the photosphere (to $z=1$ Mm). This is also because of the strong density stratification.

In conclusion, the time profiles of the Poynting flux at different heights imply that the enhancement at one (right) footpoint near the bottom induces the increase of Poynting flux in higher layers on the same side. This also induces an increase of the Poynting flux on other side of the loop at the coronal base, but not down to the photosphere. As a consequence of the similarly increased Poynting fluxes on *both* sides at the coronal base, the heat input into the loop is comparably symmetric as already discussed in Sect. 4.3.2.

Other loops that form later show similar features. A further numerical experiment with increased spatial resolution will have to show if this result can be substantiated. In particular, this will have to investigate to what extent the small-scale evolution of the (inter-)granular magnetic fields can make their way up into the corona and thus alter the spatio-temporal evolution of the Poynting flux in both loop footpoints at the coronal base.

4.6 Summary

In this paper, we presented a coronal model of an emerging active region driven by a simulation of magnetic flux emergence from the convection zone through the photosphere. The magnetic field expands into the corona, while a pair of simulated spots forms in the photosphere. Ohmic dissipation heats the coronal plasma, while heat conduction along magnetic fieldlines, radiative losses through optically thin radiation, and flows carry away the energy input. The treatment of the full energy balance ensures that the coronal pressure is set self-consistently and allows us to synthesize the EUV emission from the model corona.

Once sufficient magnetic flux was emerged through the surface and the coalescence of small-scale magnetic patches formed large-scale magnetic patches turning into sunspots, the first EUV coronal loops form within minutes. The EUV loop rises upwards, expands significantly in the horizontal direction, and, most importantly, fragments into several individual EUV structures, i.e., the changing heat input produces new strands in a growing envelope.

The energy input is driven by the advection of the magnetic field in the photosphere, i.e., by the horizontal convective motions. Connected by magnetic fieldlines through the corona, the regions of enhanced Poynting flux at one end induce an increase of the

Poynting flux at the other end at the coronal base. The upward directed Poynting flux leads to an increased energy input giving rise to the heating of the coronal plasma and the enhancement of the pressure due to the evaporative upflows. The emerging magnetic field hosting the forming loop rises into the ambient magnetic field and currents also build up near the upper part. These contribute to the Ohmic heating in the top part of the loop leading to a nearly constant heat input along the loop.

In its early evolution the coronal loop behaves (at least concerning the energy budget) similarly as a conventional 1D loop model would predict if we would prescribe the energy input. However, in the later stages the loop shows its true 3D nature. The horizontal magnetic expansion and in particular the fragmentation of the EUV emission are a clear indication that a 1D model would not be sufficient to describe a newly forming emerging loop. In the cross-sectional cut perpendicular to the EUV loop, the temperature and the density structure are comparably smooth but not exactly cospatial. This gives rise to the fragmented appearance of the loop in EUV emission with threads (or loop-fragments, or strands) with diameters much smaller than the typical spatial structures in temperature or density.

Our model of the formation and evolution of a EUV coronal loop in an emerging active region sheds new light on our understanding of coronal loop formation. A further analysis of this and more advanced numerical experiments will have to investigate the differences (and similarities) of the evolution of coronal loops seen in different wavelength bands, in particular towards X-rays, and how the forming loops would appear in spectroscopic observations. Of particular interest will be the further investigation of the evolution of the magnetic field structure in relation to the spatial structure of the synthesized coronal emission.

5 Relation of EUV loops to magnetic field lines

* Sect. 5.1, Sect. 5.2.3, Sect. 5.3.2.1, Sect. 5.3.6 and Sect. 5.4 are taken from the main text of the article *Magnetic jam in the corona of the Sun* by F. Chen, H. Peter, S. Bingert and M. C. M. Cheung, published in *Nature Physics* 11, 492–495 (2015), DOI: 10.1038/nphys3315. Sect. 5.2 (except Sect. 5.2.3) and Sect. 5.3 (except Sect. 5.3.2.1 and Sect. 5.3.6) are taken from the supplementary materials of the same article.

5.1 Introduction

The dominance of the magnetic field in the corona gives rise to the sharp appearance of coronal loops seen in EUV or X-rays (see Fig. 5.1): if energy is deposited on a magnetic fieldline, heat conduction in the ionised gas will redistribute that energy efficiently along only that fieldline (but not across). Consequently, the plasma along that fieldline becomes visible in EUV and X-rays: the coronal emission shows the magnetic field in a similar way as iron filings are used in school to show fieldlines of a magnet.

Because direct measurements of the coronal magnetic field are notoriously difficult (Peter et al. 2012), mainly extrapolations of the observed magnetic field at the surface provide the magnetic information in the corona (De Rosa et al. 2009). Stereoscopic observations can provide the three-dimensional (3D) structure of coronal loops (Aschwanden et al. 2008). Comparing EUV images and extrapolations reveals that loops seen in EUV indeed outline fieldlines (Feng et al. 2007). This paradigm underlies both one-dimensional modeling (Rosner et al. 1978, Mariska et al. 1982, Priest 2014), where the thermodynamics of the coronal plasma is often treated in detail along assumed static fieldlines, and magnetofrictional modeling (Yang et al. 1986, Cheung and DeRosa 2012), where an instantaneous thermal equilibrium is often assumed along dynamic fieldlines. On the real Sun we will not find these extreme cases, but a changing magnetic field hosting plasma with an evolving thermal structure, as described by the full equations of magnetohydrodynamics (MHD, Priest 2014).

Models accounting for this 3D structure and evolution of the solar corona point to a mismatch between magnetic and thermal structure (Mok et al. 2008), which plays an important role to understand the cross section of coronal loops (Peter and Bingert 2012). The thermal evolution, i.e., when plasma gets heated and when a loop becomes visible in EUV, is coupled in a much more subtle time-dependent way to fieldlines and heat input than often assumed. Thus, in general the appearance of coronal loops depends not just on the instantaneous position and shape of fieldlines but also on their evolution.

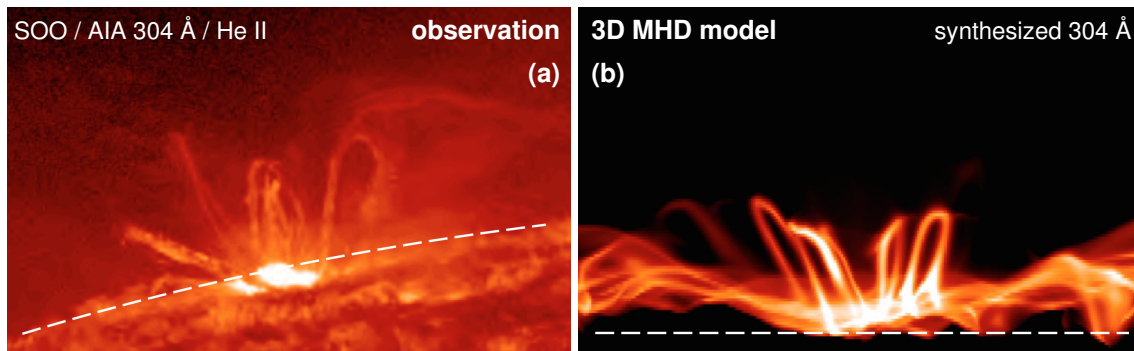


Figure 5.1: The upper atmosphere of the Sun seen in light emitted by about 100 000 K hot plasma. Panel (a) shows an observation from space with the Solar Dynamics Observatory (SDO) taken in the 304 Å band dominated by emission from singly ionised He. The limb of the Sun is indicated by the dashed line. Coronal loops are mostly seen edge-on rising some 40 000 km above the limb. Panel (b) shows a numerical simulation as described in this paper. It shows the synthesised emission in the same 304 Å channel integrated horizontally through the computational box of a numerical experiment. Similar to the real Sun, loops arch above the surface (dashed line).

We show that such scenarios are realistic for situations on the Sun, and thus our understanding of the structure and evolution of the solar corona, and ultimately the heating processes, will have to fully acknowledge the intimate interaction of the thermal evolution of coronal loops and the changing magnetic structure. In a similar way, the thermal evolution of coronal loops (in flares) has long been recognized to be caused by an interaction with a time-dependent magnetic structure (Forbes and Acton 1996, Priest 2014).

To investigate the corona above a solar active region we conduct a 3D numerical experiment. For this we solve the problem of MHD in which the induction equation describing the magnetic field is coupled to the conservation of mass, momentum and energy of the plasma. In the energy balance we account for heat conduction along the magnetic field, optically thin radiative losses and heating through Ohmic dissipation. Our model follows the philosophy of previous studies where the magnetic field is driven at the surface of the Sun, which is the lower boundary of the model (Gudiksen and Nordlund 2002, Bingert and Peter 2011, Bourdin et al. 2013). In contrast to earlier models, we drive our system by a separate model of an emerging sunspot pair (Rempel and Cheung 2014). This way coronal loops form in the emerging active region in response to the enhanced Poynting flux into the corona at locations where magnetic field is pushed around, similar to flux braiding (Parker 1972) or flux-tube tectonics (Priest et al. 2002). This new study on the evolution of thermal and magnetic properties is based on the same simulation as used before to investigate the formation of active region loops (Chen et al. 2014).

5.2 Following (a bundle of) magnetic field lines and an EUV loop in time

Conventionally, it is agreed that coronal loops seen in the EUV and X-ray images approximately indicate the magnetic field lines. This is because the magnetic energy is dominating in the corona, the emitting plasma is confined by magnetic field, and the heat conduction is very sufficient along magnetic field lines. Stereoscopic observations (Feng et al. 2007) and 3D simulations (Gudiksen and Nordlund 2005a,b, Bingert and Peter 2011) of active regions with a gradual evolution of the (photospheric) magnetic field support this concept. However, if the magnetic field would be dynamic, for example, during the formation of an active region, this concept has to be questioned, in particular if the timescales of the magnetic evolution and the thermal evolution of the plasma would be different.

To investigate the spatial relation between coronal loops and magnetic field lines, we need to follow the field lines in time. For this we assume that plasma elements are frozen-in to the magnetic field lines, which is true if the magnetic Reynolds number is large, and which is the case in most of the corona. Then we follow the motion of a selected plasma element and calculate the magnetic field line through the plasma element at each instant time. In our numerical model, we have to employ a certain magnetic diffusivity, which unfortunately allows plasma to move across the magnetic field lines. However, the average diffusion speed across 10 Mm is of the order of 1 km/s. This is much smaller than the typical perpendicular velocity (of well above 10 km/s) due to the expansion of the magnetic field, as will be detailed below.

The snapshot cadence of the numerical simulation is 30 s, which sufficiently captures the evolution of MHD variables in our simulation. When we follow the field lines as outlined above, the selected plasma element might move across several grid points in one time step. However, because the evolution of the MHD variables is smooth, we can safely use a cubic spline method to interpolate the snapshots to a sufficiently high cadence of 1 s and use this to follow the gas packages on the fieldlines. We tested this interpolation for part of the time series by writing snapshots with 1 s cadence and found the same results.

5.2.1 Axis of a magnetic tube

To follow the magnetic field, we select twelve points in the vertical middle plane of the simulation box as seeds. This plane is in the middle between the two sunspots in the photosphere and perpendicular to the connecting line between the spots. Thus it is also roughly perpendicular to the EUV loops that form and connect the opposite polarities of the emerging active region. Of these seeds, eleven form a circle of roughly 2 Mm in diameter and the twelfth is in the middle of that circle. The initial selection of these twelve points is chosen so that at some time ($t=130$ s) these points roughly encircle the EUV loop that forms. Basically the 11 points define a magnetic tube and the twelfth point is on the axis of that tube.

We follow these fieldlines in time (backwards and forwards). First we trace each fieldline from each of the initial points. Then we follow the fieldline in time by assuming that the fieldlines are frozen-in with the gas. In practice, we follow the gas parcel near the apex of the fieldline using the plasma velocity at that location, and then use the new

location of that gas parcel at the next time step as the new point for tracing the fieldline at that next time step. This is done forward and backward in time until the time period of interest is covered. The electric conductivity in the model is sufficiently high so that the (numerical) diffusion speed of the plasma through the magnetic field is small compared to the actual speed of the rising magnetic field lines. For each of the fieldlines we calculate the positions of their respective intersections with the middle plain, \mathbf{r}_i , where i is the index from 1 to 12. The position of the center of the magnetic tube in the middle plan, \mathbf{c}_{mag} , we define as

$$\mathbf{c}_{\text{mag}} = \frac{1}{12} \sum_{i=1}^{12} \mathbf{r}_i .$$

Tracing the field line for each time step from this point provides us with the fieldline of the axis of the magnetic tube. We chose this procedure because the magnetic tube will change its shape while expanding. In general, a tube with a circular cross section will get deformed into a more elongated (or even more strangely shaped) cross section (Chen et al. 2014). By using the axis of the magnetic tube we get a better representation of the evolution of the magnetic tube independent of the shape of the cross section of the tube. The center fieldlines plotted in red color in Fig. 5.2 and its attached movie, as well as in Fig. 5.7 are these axis of the magnetic tube.

The vertical speed associated with the upward expansion of the apex of the fieldline is about 30 km/s, as can be seen by inspection of the movie attached to Fig. 5.2 (or in Fig. 5.7).

5.2.2 Axis of an EUV loop

To follow (the axis of) the EUV loop we use the emission synthesised in the 193 Å band as it would be observed with AIA (Lemen et al. 2012). This shows plasma at temperatures of about 1.5 MK. We calculate the center-of-gravity of the emission in the vertical midplane and calculate the magnetic fieldline through this point.

If the emission at each gridpoint in the midplane is ε_i , and the position of that gridpoint is \mathbf{r}_i , then the center-of-gravity of the emission is

$$\mathbf{c}_{\text{emiss}} = \frac{\sum_i \varepsilon_i \mathbf{r}_i}{\sum_i \varepsilon_i} .$$

For convenience (with no impact on the result) we carry out the summations only over those gridpoints with an emissivity above a certain threshold (20 DN/pixel/s/Mm).

For each timestep we now calculate this center position of the EUV loop in the mid-plane and follow the magnetic fieldline through it. This fieldline we define as the axis of the EUV loop (plotted in blue color in Fig. 5.2 and its attached movie, as well as in Fig. 5.7).

5.2.3 Evolution of the EUV loop and fieldlines

In Fig. 5.2 we show the synthesised 193 Å observation when integrating horizontally through the computational domain. This snapshot reveals a coronal loop hosting 1.5 MK hot plasma. Following the temporal evolution in the movie (further snapshots in Fig. 5.7

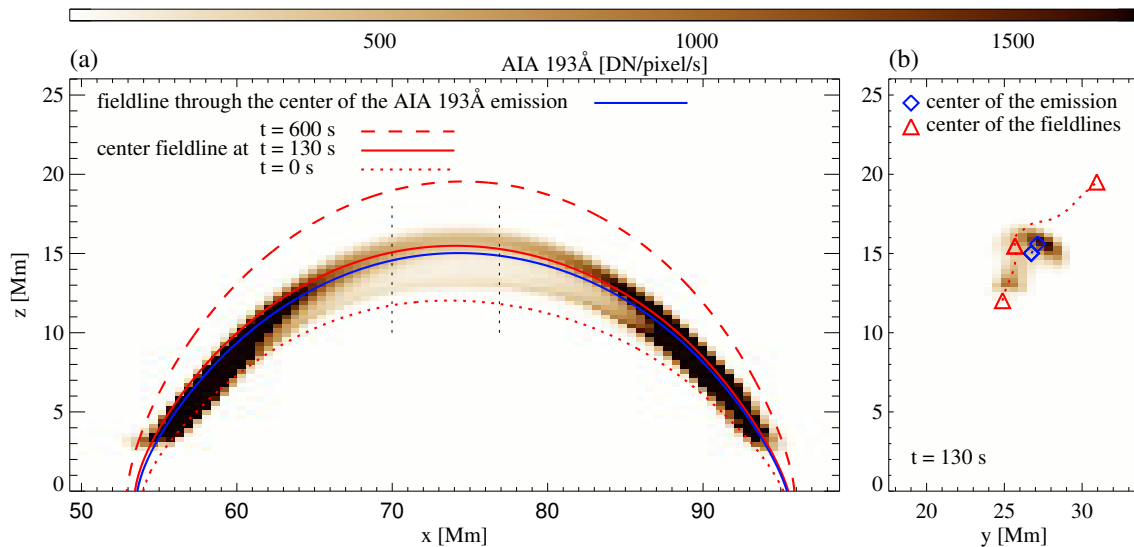


Figure 5.2: Snapshot of the coronal loop in the numerical simulation. This shows synthesised emission as seen in a wavelength band at 193 \AA dominated by Fe xii forming near 1.5 MK. Panel (a) displays the loop from the side with the emission integrated through the computational box at time 130 s. The emission pattern remains more or less at the same place (cf. Fig. 5.7 in Sect. 5.3.5). In contrast, the fieldlines expand, here indicated by the *same* fieldline shown at three different times (0 s, 130 s, and 600 s). For comparison the blue line shows the fieldline through the center of the emission structure at 130 s (see Sect. 5.2 for a more precise definition of the red and blue lines). To get a better impression of the 3D structure, panel (b) shows the middle part of the loop integrated along the loop (from $x=70$ Mm to 77 Mm as indicated by the dotted lines in panel a). Here the image shows again the 193 \AA channel emission, the blue diamond the center of the EUV loop and the red triangles the position of the fieldline in the $x=74$ Mm plane at the same three times as in panel (a). These plots cover only part of the computational domain ($\approx 150 \times 75 \times 50 \text{ Mm}^3$ in the x , y , and z directions).

in Sect. 5.3.5) it is evident that the EUV loop forms, becomes bright and then starts fading over the course of a good fraction of an hour. Most importantly, the EUV loop, i.e., the pattern visible in the 193 \AA channel, remains at more or less the same place. In particular the EUV loop is *not* expanding upwards.

This is in contrast to the evolution of the magnetic field. Also in Fig. 5.2, we overplot *one single* fieldline at different times. This fieldline moves upwards while the active region is emerging. In Fig. 5.2 (and the movie) we also show the coronal emission in a vertical slab in the middle of the loop (and perpendicular to the loop) to emphasise how differently the pattern of the EUV emission evolves compared to the magnetic structure. There is no mass flow across fieldlines. We emphasise that at each snapshot the EUV loop is roughly following a fieldline, but at each time it is a different fieldline that is aligned with the EUV loop.

5.3 Thermal evolution and coronal emission along individual fieldlines

In order to understand the difference in temporal evolution of the EUV structures and the magnetic field lines we first investigate the actual heat input on individual fieldlines. For this we use the fieldlines mentioned in Sect. 5.2. We then study how this heat input establishes the density and temperature structure along the fieldlines. Eventually, this sets the EUV emission along the fieldlines. Finally by relating the evolution of the fieldlines to the Poynting flux at the coronal base we can understand what causes the magnetic field to apparently move through the EUV loop.

For the study of the temporal evolution we choose an arbitrary zero time, $t=0$. At this time the loop as seen in EUV is just about to form. We use this zero time throughout the manuscript, so negative times refer to the temporal evolution before the EUV loop formed. All the times given in figures and movies are with respect to this zero time.

5.3.1 Heat input for individual fieldlines

The density and temperature structure along each fieldline is set by the heat input. To describe the temporal evolution of the heat input we investigate two aspects, the volumetric heat input due to Ohmic dissipation near the loop apex, and the flux of magnetic energy into the loop at the coronal base.

For the volumetric heating we investigate the Ohmic heating of the crossing point of the respective fieldline with the vertical midplane between the two sunspots. Because the setup is quite symmetric it is close (but not identical) to the heat input at the apex of the fieldline. Following the fieldline in time as outlined in Sect. 5.2 we find the time variation of the heat input near the apex for that particular fieldline. In Fig. 5.3a we show this for the twelve fieldlines discussed in Sect. 5.2 that coincide with the bright EUV loop at $t \approx 130$ s. It is clear that each fieldline is heated for some 50 s, with all the fieldlines defining the magnetic tube of roughly 2 Mm diameter peaking over times from $t \approx 130$ s to 160 s.

To investigate the flux of magnetic energy into the coronal part of the fieldline we study the vertical Poynting flux at the base of the corona for each fieldline. For simplicity we use the height of $z=2.9$ Mm, which is the average height where the temperature rises above 10^5 K. In general the Poynting flux is defined as $S = \eta j \times B - (v \times B) \times B / \mu_0$, with the current j , the magnetic field B , velocity v , magnetic resistivity η , and the magnetic permeability μ_0 . At the base of the corona, where the magnetic energy density already dominates the thermal energy density, the first term involving the currents is negligible. The $(v \times B) \times B$ term contains the contribution from emerging horizontal fields and (almost) vertical fields being shifted around, e.g., following the concept of braiding (Parker 1972) or the tectonics (Priest et al. 2002). Because we consider only the energy input into the fieldlines reaching coronal heights, we consider only the latter part. Finally, we are left with the contribution to the vertical Poynting flux involving the velocity v_{\perp} perpendicular to the magnetic field. So in terms of the components along the horizontal x - and y -directions and the vertical z -direction the vertical Poynting flux is

$$S_z = - \frac{1}{\mu_0} (v_{\perp x} B_x + v_{\perp y} B_y) B_z. \quad (5.1)$$

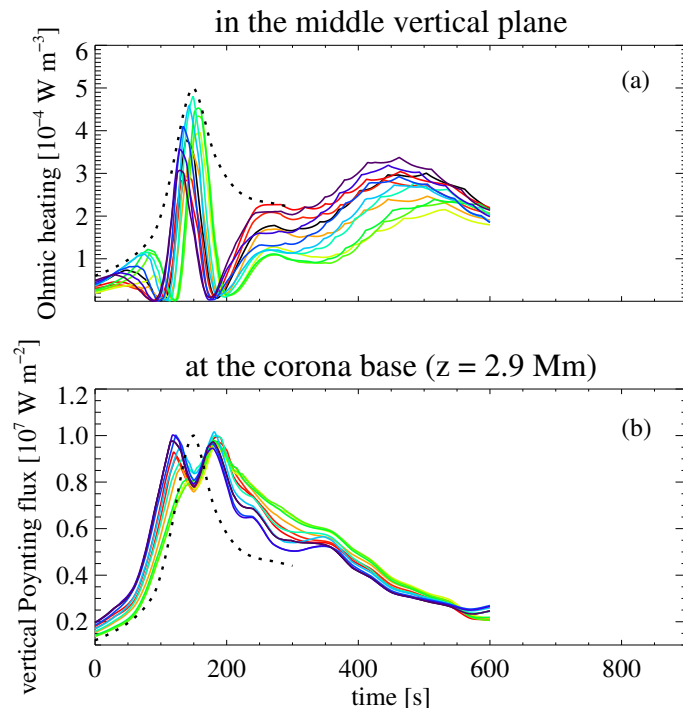


Figure 5.3: Heating along individual field lines. The coloured lines show the temporal variation of the heating for the twelve fieldlines as defined in Sect. 5.2. Panel (a) shows the volumetric energy deposition due to Ohmic dissipation at the cross section of the respective field line and the vertical midplane between the footpoints. This is close to the apex of the respective fieldline. The dotted line displays an envelope for the heat input. Panel (b) shows the magnetic energy flux into the loop, viz. the vertical component of the Poynting flux as defined in Eq. (5.1), at the base of the corona. For comparison the dotted envelope from panel (a) is plotted in panel (b), too, just scaled to roughly match the peak of the Poynting flux.

We evaluate this quantity for each of the fieldlines at the base of the corona (at each of its legs). The temporal evolution of this quantity (for the “right” leg at $x \approx 95 \text{ Mm}$; cf. Fig. 5.5) is shown in Fig. 5.3b for the set of twelve fieldlines. Just as the Ohmic heating at the apex of the fieldlines, this energy input shows a clear (double) peak in time. Comparing the two panels of Fig. 5.3 shows that the energy input at the base of the corona precedes the heating rate at the apex by about 30 s (the dotted lines in both panels). For a typical Alfvén speed of some 500 km/s this is the time delay expected for the magnetic disturbances traveling up the half loop length of some 15 Mm from the coronal base.

5.3.2 Hot spot of Energy input

The discussion above shows clearly the increase and subsequent decrease of the heat input on individual expanding fieldlines. To investigate the cause for this transient heating on a fieldline, we follow the footpoints of the fieldlines at the base of the corona and relate it

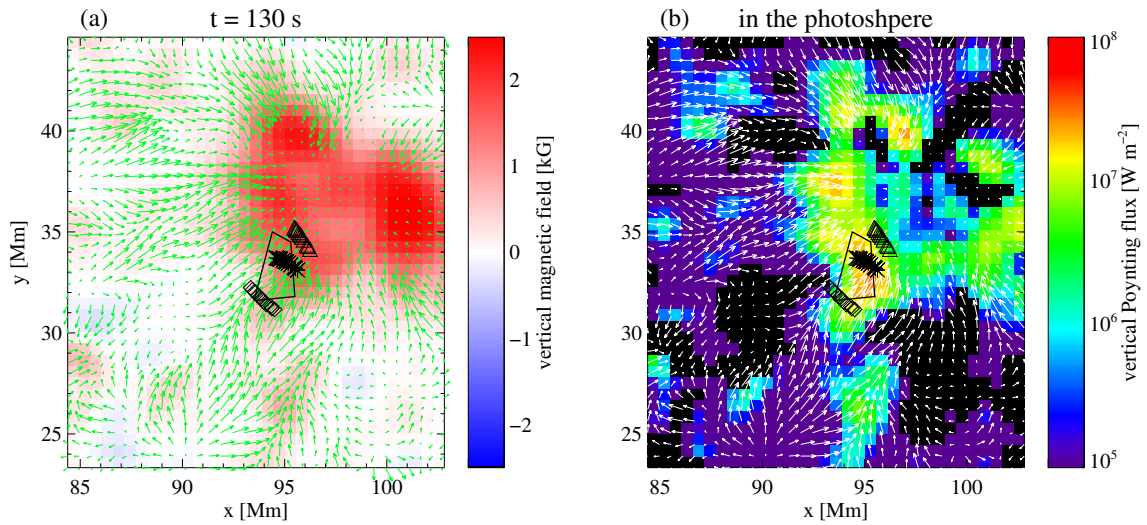


Figure 5.4: Evolution at the solar surface while the coronal loop forms. Panel (a) shows the vertical magnetic field and panel (b) the vertical component of the Poynting flux, both in the photosphere. These snapshots are taken at the time $t=130$ s. The concentration of magnetic field in panel (a), seen in red, shows the location of one of the two sunspots that form the active region in this simulation. For the time $t=-600$ s we indicate a number of positions by the diamonds that are located at the footpoints of fieldlines that transverse the bright coronal loop later. The asterisks and triangles show the position of these locations at later times $t=+130$ s, and $+1200$ s, when they are carried with the coalescent flow forming the sunspot. The field-of-view covers only a small fraction of the whole computational domain ($\approx 150 \times 75$ Mm² in the horizontal directions).

to the vertical Poynting flux at the base of the corona as defined in Eq. (5.1).

5.3.2.1 Magnetic braiding in the photosphere

The cause for the transient enhancement of the heating of individual fieldlines is found at their roots. The coalescent flow that forms the sunspot drives magnetic patches towards the strong magnetic field of the sunspot (Rempel and Cheung 2014, Cheung et al. 2010). This is illustrated by the arrows in Fig. 5.4 that display the horizontal flows in the photosphere. At the outer edge of the spot there will be a region of enhanced (vertical) Poynting flux, i.e., of upward directed flux of magnetic energy. This is similar to the flux-tube-tectonics model (Priest et al. 2002) where (horizontal) shuffling of magnetic patches leads to an upward directed flux of magnetic energy, which is then available to heat the coronal plasma. Because each fieldline is pushed into the spot and thus transverse the region of the enhanced Poynting flux, the heat input into the corona along individual fieldlines is transient (see detailed discussion in Sect. 5.3.2.2 and movie attached to Fig. 5.5). Thus EUV loops will show up wherever strong (horizontal) gradients of the magnetic field are present at the footpoints, similar to the tectonics model (Priest et al. 2002).

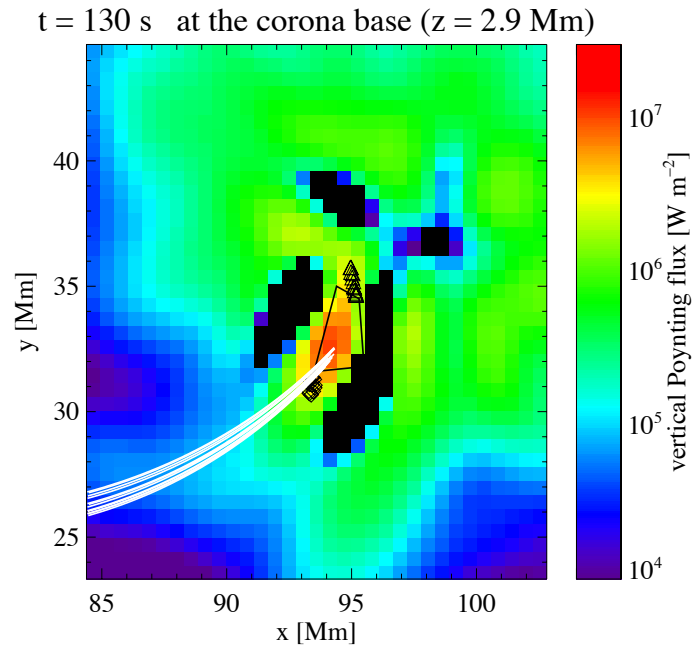


Figure 5.5: Hot spot of Poynting flux at the base of the corona. The image shows the vertical Poynting flux at the base of the corona as defined in Eq. (5.1). The red region in the middle of the image shows the location of the enhanced Poynting flux. This is the hot spot of energy flux into the corona. The white lines show the projection of the magnetic fieldlines of the magnetic tube defined in Sect. 5.2 at time $t=130 \text{ s}$. The diamonds and the triangles indicate the position of the footpoints of these fieldlines at times $t=0 \text{ s}$ and 600 s . The pattern of the Poynting flux remains rather stable over 10 minutes. The field-view and the polygon roughly encircling the hot spot are the same as in Fig. 5.4.

5.3.2.2 Hot spot at the coronal base

In Fig. 5.5 we display the vertical Poynting flux at the time $t=130 \text{ s}$ along with the projection of the twelve selected field lines as defined before in Sect. 5.2. The pattern of the vertical Poynting flux is relatively stable over the course of more than 10 minutes (cf. the movie attached to Fig. 5.5). In particular, the increased Poynting flux in the middle of the panel remains roughly at the same position forming some sort of *hot spot*. This hot spot at the base of the corona is roughly co-spatial with the increased Poynting flux at the solar surface (the black polygon in Fig. 5.5 is at the same position as the polygon in Fig. 5.4 showing the Poynting flux at the surface).

While the fieldlines evolve and rise into the atmosphere they move (roughly) horizontally at low heights. Thus at the base of the corona they transverse the hot spot of the Poynting flux. This is evident by inspection of the movie attached to Fig. 5.5. Of course, while the fieldline transverse the hot spot, the Poynting flux at the coronal base changes slowly. This is the reason why a dip is seen between two peaks of the Poynting flux in Fig. 5.3b. However, it is not the temporal change of the Poynting flux at the base of the corona that is responsible for the increase of the heating. Instead, the main effect for this is the footpoint of the fieldline transversing a hot spot of Poynting flux at the base of the

corona.

5.3.3 Temperature and density along individual fieldlines

While a fieldline is rising upwards through the lower atmosphere (with up to 10 km/s to 30 km/s vertically), the density decreases continuously (before time $t \approx 130$ s; Fig. 5.6a). This is because the rising fieldline is lifting up the cool material and the upwards directed pressure gradient is no longer able to counteract gravity. Thus the plasma drains downwards along the fieldline. In part, the loss of mass for individual fieldlines is also due to numerical imperfections of the simulation: (hyper) diffusion that is needed to smooth out numerical instabilities allows the plasma also to diffuse across fieldlines. In this early phase, when the fieldlines rise through the chromosphere, this can account for up to about half of the mass loss of individual fieldlines. However, this might not be too unrealistic considering that on the real Sun in the cool chromosphere there will be significant cross-field diffusion of mass, because the plasma is only partially ionised there. Once the temperature on the fieldline starts to rise (around $t \approx 130$ s) the cross-field mass diffusion no longer plays a role.

After the heating on the fieldline sets in, the temperature will rise (for the set of fieldlines considered here, this happens at $t \approx 130$ s; see Fig. 5.6b). The draining of the mass from the fieldline and the increase of the heating rate together leads to a very strong increase of the heating *per particle*, which is responsible for the very sharp increase in temperature. Within some 50 s the peak temperature along the expanding fieldline is rising from basically chromospheric temperature to well above 1 MK, eventually reaching some 3 MK.

In response to the heating of the plasma along the fieldline, heat conduction back to the surface together with the enhanced energy input in the low parts of the atmosphere leads to heating and evaporation of cool plasma into the upper atmosphere. The resulting upflows cause a gradual increase of the density (from time $t \approx 130$ s to 250 s; Fig. 5.6a).

Once the heating on that fieldline ceases (around $t \approx 200$ s; Fig. 5.3), the temperature remains high, because the coronal cooling time is of the order of the better part of an hour. However, the density starts dropping soon after the heating stopped (from time $t \approx 250$ s onwards; Fig. 5.6a). This can be illustrated with the help of long-known equilibrium considerations, even though the variability in the modelled system is more complex. The temperature T and the pressure p (and thus the density ρ) are basically set by the heat input H ; under equilibrium conditions they follow power laws (Rosner et al. 1978), $T \propto H^{2/7}$, $\rho \propto H^{4/7}$, i.e., the density is more sensitive to changes of the heat input than the temperature. Therefore the density adjusts faster to the drop of the heat input after $t \approx 200$ s. (The density drop for each individual fieldline occurs after the temperature passed through the temperature of maximum response of the EUV passband and is thus not of major relevance for the phenomenon described here; see below).

This filling and draining along fieldlines has been described earlier for this 3D model (Chen et al. 2014), and the average rate of change of the mass in the top 20 Mm of the fieldline is consistent with the (mostly vertical) mass flow across the chromosphere-corona boundary. In Fig. 3 of our previous study (Chen et al. 2014) the mass exchange is summarised: increased heating causes an evaporative upflow in the bottom part, and later when the fieldline expanded further, the velocity pattern in the upper part reverses and

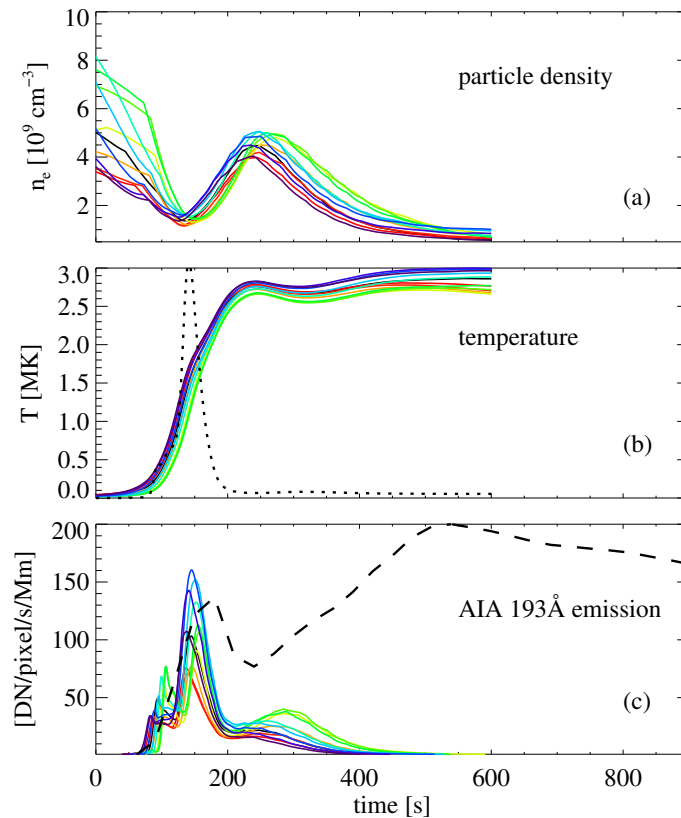


Figure 5.6: Temporal evolution at the apex of fieldlines. Panels (a) and (b) show the temporal variation of the temperature and density near the apex of each of the evolving fieldlines. These are the same fieldlines as in Fig. 5.3 with the same color coding. Panel (c) displays the synthesised emission, also at the intersection of the respective fieldline with the vertical midplane. The normalised temperature response curve (for the central fieldline) of the AIA 193 Å channel dominated by Fe xii is overplotted as a dotted line in panel (b). The emission of the whole EUV loop (integrated over the vertical midplane) is shown as a dashed line in panel (c).

the loop starts draining. (Note that the velocity in that Fig 3 is along the loop, e.g., red on the left side and blue on the right side does not imply a siphon flow, but evaporation into the corona). In addition to this, the lower transition region is pushed down due to the increase in pressure following the heating in the upper layers, similar to what has been found in quiet Sun network model (Hansteen et al. 2010). Together with the expansion of the fieldlines, this would produce a pattern of net redshifts in the transition region and blueshifts in the hotter regions as found in observations (Peter and Judge 1999).

This behaviour of the temperature and density along the fieldline is consistent with one-dimensional models of coronal loops with variable prescribed heating rates (Mariska 1987). However, here we self-consistently describe the heat input along each fieldline in the 3D model as determined by the fieldlines being moved across the hot spot of Poynting flux at the base of the corona.

5.3.4 EUV emission along individual fieldlines

What we see of the corona is neither the temperature nor the density, but the photons that are emitted by the plasma. Thus we synthesise the emission from the model as it would be seen by an EUV instrument. Here we concentrate on the 193 Å channel of AIA/SDO that images emission from mainly Fe xii forming at about 1.5 MK. For this we use the same procedures as outlined before (Peter and Bingert 2012, Boerner et al. 2012), implicitly assuming ionisation equilibrium.

The 193 Å channel has a temperature response function $G(T)$ that peaks sharply at about 1.5 MK. Consequently, when following an individual fieldline that is heated in time, the contribution to the 193 Å channel will be significant just during the time the fieldline is at the matching temperature (cf. Fig. 5.6b). The actual emission is then given by $n^2 G(T)$, where n is the (electron) density. To characterize the emission from any given fieldline, we show the emission at the intersection of the fieldline with the midplane used before in Fig. 5.6c. This reflects the emission near the apex of the fieldline.

The increase of the coronal emission on an individual fieldline peaks sharply (Fig. 5.6c) when the temperature is close to the peak of the contribution function $G(T)$. The timescale for the brightening of an individual fieldline is thus determined by the rise time of the temperature, and is of the order of 50 s. Figure 5.6 shows that the peak of the coronal emission for each individual fieldline is during the phase of rising density, well before the density drops because the heating for the respective fieldline ceased. Thus the temporal variability of the coronal emission for each individual fieldline is mainly governed by the evolution of the temperature: Each fieldline brightens shortly after it was heated and its temperature rose quickly.

So ultimately each of the expanding fieldlines is brightening according to the time when the footpoint of the fieldline transverses the hot spot of the Poynting flux at the base of the corona causing the enhanced heat input. Consequently the fieldlines lighten up in succession according to their expansion. This is evident from the set of fieldlines shown color coded in Figs. 5.3 and 5.6c for the heat input and emission.

The above discussion concentrates on the results relating to EUV instruments, e.g., the Atmospheric Imaging Assembly (AIA, Lemen et al. 2012). Currently EUV imaging provides the highest spatial resolution in the corona, significantly higher than X-ray observations, e.g. with the recent XRT instrument (Golub et al. 2007). However, the response in temperature for X-ray instruments is quite different than EUV instruments. The EUV bands typically show plasma over a temperature range of 0.3 in $\log_{10} T$ [K] (FWHM of the response function, Boerner et al. 2012), i.e. a factor of 2. In contrast, the X-ray instruments typically image plasma at higher temperature over wider range of temperature (peak of response function near 8 MK, covering a factor of 4 in temperature, Golub et al. 2007). This different response might change the situation quite a bit, in particular because the temperatures in the model loop discussed here reach peak temperatures of about 3 MK. Work including the synthesis of X-ray emission to discuss this in more detail is underway.

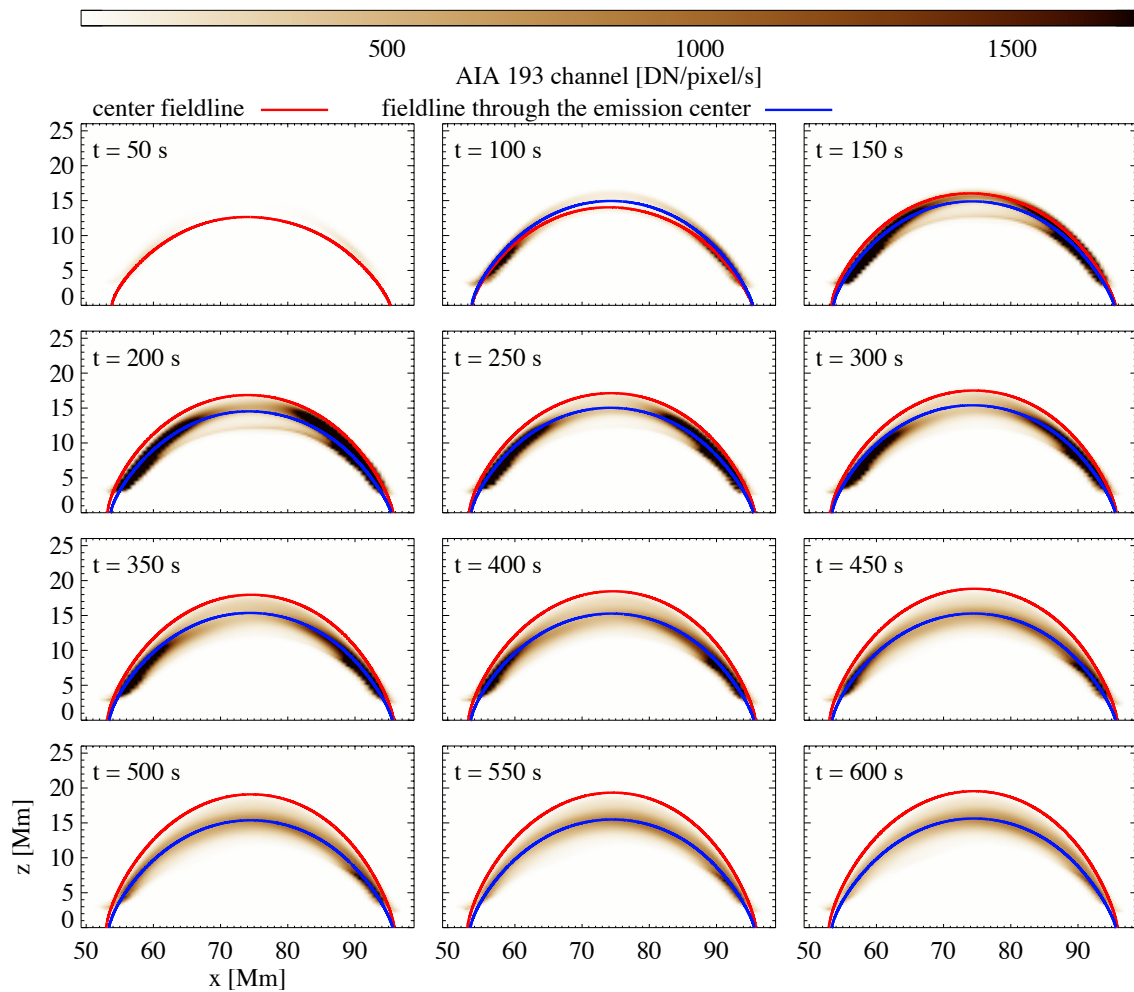


Figure 5.7: Magnetic fieldline moving through EUV loop. This image sequence shows the evolution of the synthesized EUV emission in the 193 Å band of AIA dominated by plasma at 1.5 MK radiating in Fe XII. The red line shows the fieldline in the expanding magnetic field, the blue line the fieldline through the center of the EUV emission pattern at each snapshot. This is similar to panel (a) in Fig. 5.2.

5.3.5 Magnetic fieldlines moving through stationary EUV loop

In Fig. 5.7 we show the temporal evolution of the resulting EUV loop when seen from the side together with the position of the center fieldline of the magnetic tube selected in Sect. 5.2. The magnetic tube is constantly moving upwards, from an apex height of ≈ 12.5 Mm at $t=50$ s to ≈ 17 Mm at 200 s corresponding to a speed of 30 km/s. The expansion of the fieldlines slows down at greater heights because they are now running into the fieldlines that emerged before. Until the end of the time series shown in Fig. 5.7 at $t=600$ s the magnetic tube expanded only another 2.5 Mm, corresponding to an average speed of about 5 km/s.

While each individual fieldline brightens up for only some 50 s to 100 s the successive brightening of the expanding fieldlines causes a comparably stationary bright loop visible in coronal EUV emission (Fig. 5.7). In particular the apex height of the center of the EUV

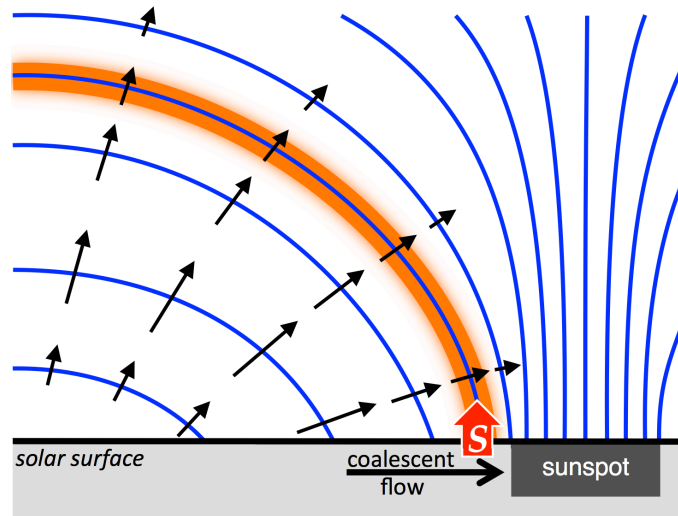


Figure 5.8: Cartoon showing the interplay between magnetic field expansion and the EUV loop. A coalescent flow forming the sunspot drags the magnetic field in the photosphere near the solar surface into the sunspot. In response a hot spot of enhanced upward directed Poynting flux, S , forms (red arrow). The expanding fieldlines (blue) move upwards and to the side. When they transverse the hot spot of Poynting flux, the plasma on that fieldline gets heated and brightens up. As the fieldline expands further, it leaves the hot spot and gets darker again. In consequence a bright coronal EUV loop forms (orange) and remains rather stable while the successively heated fieldlines move through.

loop (blue line in Fig. 5.7) varies only slightly between $z \approx 14.5$ Mm and ≈ 15.5 Mm, while over the same time the magnetic tube rose by more than 7 Mm.

The EUV loop formed by the expanding fieldlines shows some variability of its brightness at the apex, but it remains bright for well over 10 min (dashed line in Fig. 5.6c). However, after about $t \approx 550$ s the loop starts fading away because the hot spot of the Poynting flux at the base of the corona gets weaker.

5.3.6 Summary of the mechanism

This mechanism is illustrated by the cartoon in Fig. 5.8. During the emergence of magnetic flux forming a sunspot pair the field is pushed upwards and to the sides. In sunspots the magnetic field is very strong and convection is suppressed. Thus the flow driving the coalescence of the magnetic field come to a halt. Whenever a fieldline is crossing the region of enhanced Poynting flux, energy is deposited along that fieldline and the plasma on it is heated. Consequently this fieldline becomes visible in EUV for a short time. With successive fieldlines passing the hot spot of Poynting flux, they all brighten roughly at the same place, creating the illusion of a static emission pattern forming a loop, while the magnetic field is moving. Future work will have to show to what extent this scenario also holds for X-ray emission that typically forms over a broader range of temperatures than the EUV bands.

5.4 Conclusions

In our 3D numerical experiment we find that the temporal evolution of the magnetic field in the corona can be radically different from that of the patterns seen in the coronal emission. This implies that modeling the *temporal evolution* of EUV loops as 1D structures following a static fieldline is a problematic concept in regions where the magnetic field is evolving, i.e. whenever the Sun gets dynamic — and interesting. Thus many of the time-dependent 1D loop models that have been used as the workhorse in coronal studies over the last two decades need to be reconsidered. In cases where one can reasonably assume a static magnetic structure confining the plasma, a 1D model might describe the loop sufficiently well. In principle, a model combining several 1D models could account for changes in loop length (Martens and Kuin 1983) or magnetic connectivity (López Fuentes and Klimchuk 2010) to mimic the emergence process, but such a multiple-1D-model would suffer from the lack of self-consistency. Only if treated in (2D or) 3D, the photospheric motions that drive the magnetic changes will lead to a self-consistent interaction of the neighbouring fieldlines that result in a (variable) spatial pattern of heat input. Still, at any given snapshot the coronal EUV loops in our 3D model outline magnetic field lines. Therefore EUV observations should provide useful information when implemented into procedures to recover a snapshot of the coronal magnetic field through extrapolation methods (Malanushenko et al. 2014). In summary, the magnetic and thermal evolution of the corona should be treated as a coupled system in a single problem — this requires to have a more holistic view of the magnetic and thermal properties of the corona when addressing the question of the structure, dynamics and heating of the corona.

6 Oscillation of the coronal loop in a realistic coronal model

* Sect. 6.1 is Sect. 1 in the first submitted version of the article *Using coronal seismology to estimate the magnetic field strength in a realistic coronal model* by F. Chen and H. Peter, published in *Astronomy & Astrophysics*, 581, A137 (2015), DOI: 10.1051/0004-6361/201526237. Sect. 6.2 to Sect. 6.5 are Sect. 3 to Sect. 6 in the first submitted version of the same article. Reproduced with permission from *Astronomy & Astrophysics*, © ESO

6.1 Introduction

Waves in the corona are extensively studied in numerous theoretical analysis and observations by all means (e.g. see reviews by Nakariakov and Verwichte 2005, Banerjee et al. 2007, Wang 2011, De Moortel and Nakariakov 2012). Oscillations of coronal loops, which is essentially a signature of the waves in the corona, can be a mean to diagnose the properties of corona loops, for example, the magnetic field strength. This was proposed as coronal seismology by Uchida (1970) and Roberts et al. (1984). In addition to the plasma properties that usually have to be assumed or deduced in various ways, for example the spectroscopic diagnostics (Mariska 1992), the key of coronal seismology is to determine the mode of the oscillation and the phase speed of the corresponding wave. In practice in the last two decades, the oscillations of coronal loops were mainly measured either by the displacements and disturbances in extreme ultraviolet (EUV) images (Aschwanden et al. 1999, Nakariakov et al. 1999, De Moortel et al. 2000, Nakariakov and Ofman 2001, Aschwanden and Schrijver 2011, Yuan and Nakariakov 2012, Verwichte et al. 2013b, Guo et al. 2015), or by the periodic patterns in the Doppler velocity obtained from EUV spectrometers (Ofman and Wang 2002, Wang et al. 2003, 2007, Van Doorselaere et al. 2008, Erdélyi and Taroyan 2008, Ofman and Wang 2008, Mariska and Muglach 2010, Tian et al. 2012). The deduced magnetic field strength is typically between 10 G and 100 G, which is generally consistent with that derived from extrapolations on the coronal magnetic field (Schrijver et al. 2006, Wiegmann and Sakurai 2012).

Meanwhile, a lot of theoretical efforts are also made to explore the impacts of the complexities of real coronal loops, such as the curved geometry, density stratification, and non-uniform cross section (Van Doorselaere et al. 2004, Verwichte et al. 2006, Erdélyi and Verth 2007, Arregui et al. 2007, Goossens et al. 2009, Ruderman and Erdélyi 2009, Selwa et al. 2011). De Moortel and Pascoe (2009) tested the estimate of the magnetic field strength by coronal seismology in a three-dimensional (3D) model, in which the magnetic

field strength and number density along the target coronal loop are constant (Pascoe et al. 2009). This configuration prescribed a single and definite reference value, and the authors did find a difference between the reference and the deduced magnetic field strength. In the real corona the magnetic field strength varies along the loop, so does the number density, despite of the large density scale height in the corona. Aschwanden and Schrijver (2011) and Verwichte et al. (2013a) compared the magnetic field strength deduced by coronal seismology with that obtained from a potential or force-free extrapolation on the coronal magnetic field. Because of the limitation of the assumptions (i.e. potential or force-free), it is uncertain if the extrapolated magnetic fieldline actually matches the observed loop. Promising examples were presented by Feng et al. (2007). They showed that the magnetic fieldlines in a linear-force-free extrapolation do follow the loop structures reconstructed from stereoscopic observations.

Given all the difficulties of clinching the reference values from observations, it is indeed helpful to test coronal seismology in a model corona, which has realistic plasma properties and a magnetic field configuration similar to that of a real active region. Recent forward coronal models (Gudiksen and Nordlund 2005a,b, Bingert and Peter 2011) account for the cooling through the optically thin radiation and the highly anisotropic heat conduction along magnetic fieldlines. The horizontal motions in the model photosphere braid the magnetic fieldlines. The Ohmic dissipation of the currents induced along the coronal magnetic fieldlines is sufficient to heat the coronal plasma to over one million K. The energy distribution in this type of model is well consistent with the expectation of the nanoflare mechanism (Bingert and Peter 2013). The proper treatment on the energy balance allows these models to resemble the plasma properties in the real corona, so that the synthesised emission from these models can be directly compared with real observations. These model successfully explain some basic features of coronal loops (e.g. the non-expanding cross section by Peter and Bingert 2012). A one-to-one data driven simulation can reproduce the appearance and dynamics in the particular solar active region that drives the simulation (Bourdin et al. 2013).

Being successful in modelling the plasma properties and general dynamics of the corona, a further challenge is how well the loop oscillation in a realistic model resembles that on the real Sun. We analyse the synthetic observations, in which we clearly see some loop oscillations, as an observer, and estimate the magnetic field strength from the oscillation parameters. The model has a magnetic field configuration of a typical bipole active region. This give us a chance to compare the magnetic field strength derived by coronal seismology with the actually value in the model, which varies along the coronal loop as in the reality. This comparison is a complementary to the previous numerical experiment (De Moortel and Pascoe 2009) and observations (Aschwanden and Schrijver 2011, Verwichte et al. 2013a), and helps us to understand the implication of the derived field strength, when coronal seismology is applied to actual observations.

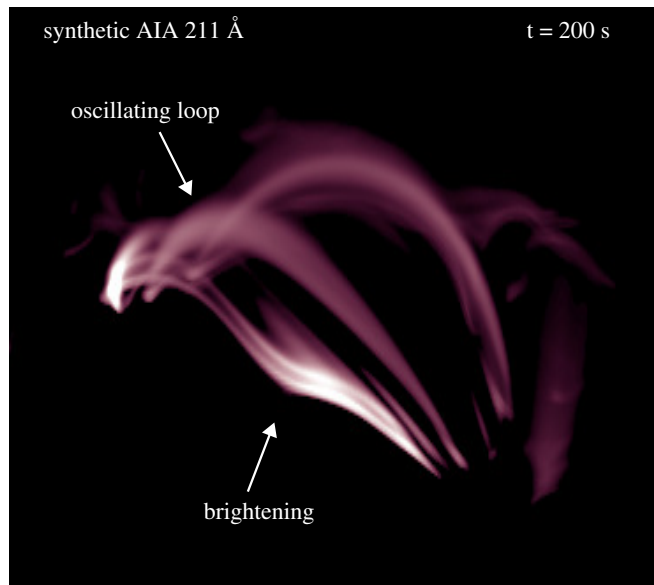


Figure 6.1: System of coronal loops synthesised from a 3D MHD model. This shows how the model corona would appear in the AIA 211 Å channel that is dominated by Fe XIII observing plasma at mainly 2 MK. The distance between the two footpoints of the loops is about 35 Mm. The lower arrow indicates the position where the brightening happens (more details in Sect. 6.2.1). The upper arrow points to the oscillating loop we analyse in detail (Sect. 6.2.3).

6.2 Oscillation in the synthetic observation

6.2.1 Trigger of the oscillation

In addition to the continuous evolution of the coronal loops, some loops start to oscillate when a brightening happens in the lower left part of the active region (see the lower arrow in Fig. 6.1) at $t \approx 200$ s (for convenience, time is related to 4350 s after the start of the simulation).

The brightening is due to an enhancement of the Ohmic heating along the fieldlines at the flank of the active region. The cool plasma is quickly heated to a temperature at which the response function of the AIA 211 Å channel peaks. The increase of the Ohmic heating comes from the increase of the currents, which is due to some forced reconfiguration of the coronal magnetic field. The increase of the currents also results in a transient increase of the Lorentz force, which drives a kick perpendicular to the fieldlines. The disturbance can propagate from the brightening site across the active region and trigger the transverse oscillation of other loops. The oscillation is clear, albeit not violent, in the associated animation of Fig. 6.1.

For a rough estimate, given a length scale (distance from the brightening site to the farthest visible loop) of about 25 Mm and a wave speed of 2000 km s^{-1} , the travel time across the active region is about 12 s. With the cadence of the animation (Fig. 6.1), the oscillation starts almost at the same time as the brightening.

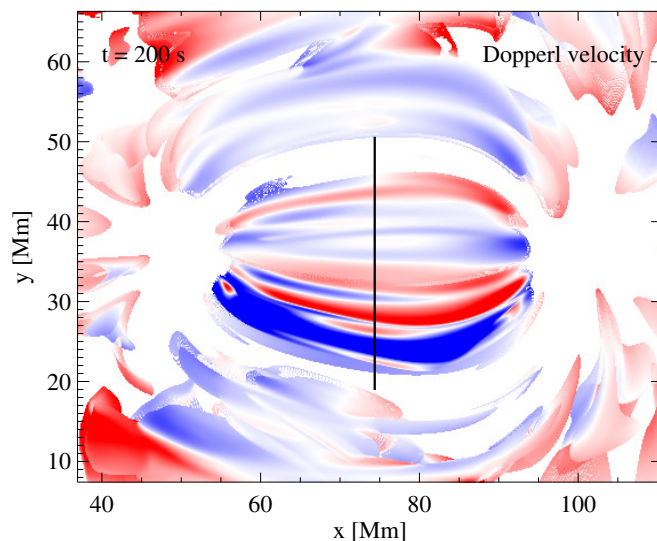


Figure 6.2: Map of the Doppler velocity obtained by fitting the synthetic Fe XIII 202 Å line as observed from the top of the active region. The black solid line show the position of the slit, along which we get a time series of the Doppler velocity (Sect. 6.2.2). This time series is equivalent to the data from a sit-and-stare observation (Sect. 6.2.2).

The oscillation, which is mainly in the normal direction of the loop, lasts for about 300 s, and decays gradually. It appears very similar to the transverse oscillations, which are widely found in the EUV observations and usually interpreted as the standing, fast kink mode (Nakariakov and Verwichte 2005). Our model allows us to conduct a twofold experiment, in which we, as an observer, measure the oscillation from the synthetic observation instead of the original variables of the model, and then compare the magnetic field strength deduced from coronal seismology with the actually value we already know from the model.

6.2.2 Synthetic spectral and the sit-and-stare observation

Although the loop oscillation is very clear in the animation for the eyes, its quantification is difficult because the oscillation amplitude is not significantly larger than the width of the coronal loop. The alternative is to measure the velocity disturbances from synthetic spectroscopic observations. For this purpose, we simulate an observation from the top of the active region, i.e. as if we observe an active region at the solar disk center. With the procedure described by Peter et al. (2004, 2006), we use the temperature, density, and vertical velocity in our model to synthesise the Fe XIII 202 Å line.

The line profiles are typically single peak Gaussians whose width is determined by the local plasma temperature and the distribution of the line-of-sight (vertical in this case) velocities. By fitting the spectral lines, we obtain the line intensity and the Doppler velocity in the model active region. The Doppler velocity map in Fig. 6.2 shows the flows in the active region. The ideal way to identify the periodic velocity disturbance corresponding to the oscillation is the sit-and-stare observation mode. In such a mode, the

Table 6.1: Parameters of the synthetic oscillating loop

parameter	symbol	value	derived by
coronal loop length	L	45 Mm	
oscillation period	P	52.5 s	Eq. (6.1)
damping time	τ	125 s	Eq. (6.1)
temperature	T	1.5 MK	
internal density	n_i	$5.7 \times 10^8 \text{ cm}^{-3}$	
density ratio	n_e/n_i	0.12	
kink mode speed	c_k	1730 km/s	Eq. (6.3)
inverted $ B $	B_{kink}	79 G	Eq. (6.4)
average $ B $	$\langle B \rangle$	92 G	Eq. (6.5)

spectrometer will obtain a time series of the spectra at a fixed location. For the synthetic observations, we choose a artificial slit along the y direction located at the center of the field of view (solid line in Fig. 6.2). We extract the line intensity and the Doppler velocity along this slit with a 10 s time cadence. This time series can be considered as the data from a sit-and-stare observation focusing on the apex of an oscillating loop.

6.2.3 Measurement of the transverse loop oscillation

Similar to what is applied on real sit-and-stare observations (e.g. Wang et al. 2009, Mariska and Muglach 2010), we produce a time-space diagram from the synthetic spectroscopic observation. In the diagram the horizontal dimension is the time, and the vertical dimension is the position along the slit. Panel (a) and (b) in Fig. 6.3 show the time-space diagram for the line intensity and the Doppler velocity along the part of the slit covering the oscillating loop.

The line intensity does not show any clear oscillation in the y direction. This is consistent with the impression from the synthetic AIA images that the oscillation (at the loop apex) is predominately in the z direction (i.e. along the line-of-sight). The oscillation in the Doppler velocity is much more evident. It starts at around $t=200$ s, which is similar to the timing in the synthetic AIA images.

We use a black box to mark the location of the bright loop in the intensity map in Fig. 6.3 (a), and extract the Doppler velocity in the same black box in Fig. 6.3 (b). By averaging in the y direction, we obtain the mean Doppler velocity in the loop as a function of time, which is shown by the black symbols in Fig. 6.3 (c). They show a clearly damped oscillation.

We fit this oscillation by

$$f(t) = A_0 \exp\left(-\frac{t-t_0}{\tau}\right) \sin\left[\frac{2\pi}{P}(t-t_0)\right] + A_1 t + A_2, \quad (6.1)$$

where t is time, P the period, τ the damping time-scale, t_0 the initial time, and A_0 the amplitude. In addition, A_1 and A_2 account for a linear background. By fitting the curve

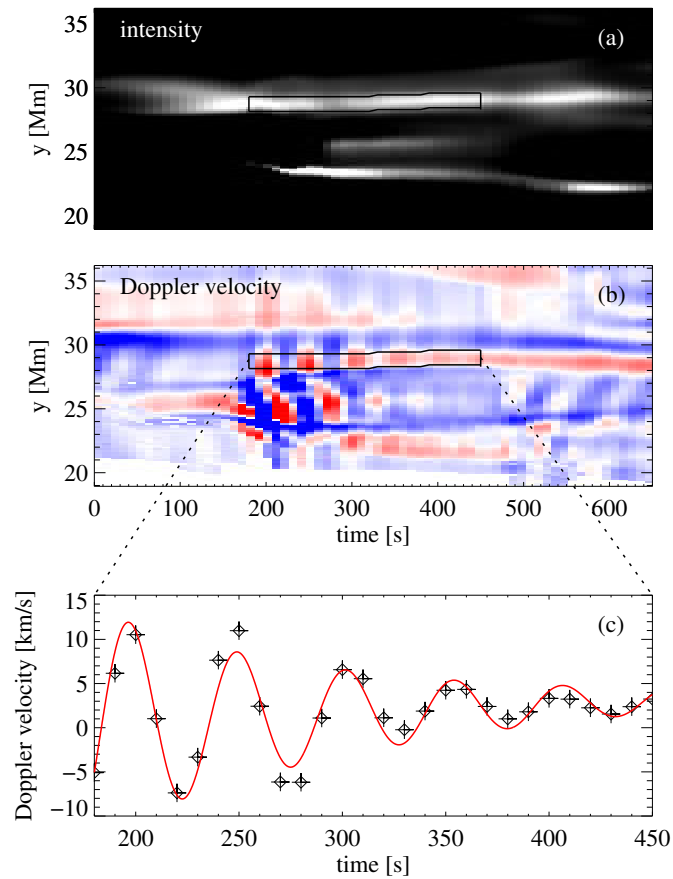


Figure 6.3: Results from the synthetic spectroscopic observation in a sit-and-stare mode and the fitting to the oscillation in the synthetic spectral data. (a): The time-space diagram of the line intensity along part of the slit in Fig. 6.2. (b): The time-space diagram of the Doppler velocity along the same slit. The black boxes are identical in both panels. They show the location of oscillating bright loop, and the time during which the oscillation is evident. (c): The average Doppler velocity in the bright loop as a function of time. This is an average between $y=28$ Mm and $y=29.5$ Mm (i.e. in the y direction of the black box). The red line is the fit with a damped sinusoidal function, Eq. (6.1).

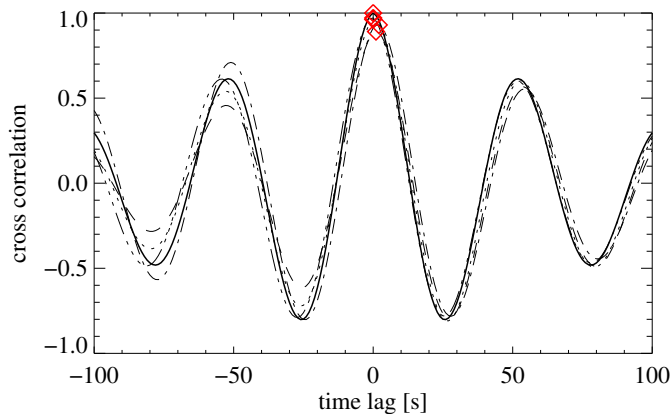


Figure 6.4: The cross correlations between the oscillation measured at the loop apex (i.e. in the slit in Fig. 6.2) and those measured at other four different positions along the same loop, which includes two at the midway from the apex to footpoints, and two close to the footpoints. The solid line shows the self-correlation of the oscillation at the loop apex. The time lag spans from -100 to $+100$ s, which is about four times of the oscillation period (52.5 s at the loop apex). The red diamonds indicate the peaks of the cross correlation functions. See Sect. 6.2.3 for details.

with a uniform weight, we obtain a period of $P=52.5$ s and a damping time of $\tau=125$ s.

We apply the same analysis on some other slit positions. When the slits are located in the midway from the loop apex to the loop feet, the average Doppler perturbation in the loop appears very similar to that at the apex (except the amplitude). Fitting with Eq. (6.1) also yields a period and a damping time consistent with the results at the loop apex.

Particularly when we put the slit close to the footpoints, the actually velocity perturbation projected into the vertical direction is considerably reduced, and the oscillatory pattern is also contaminated by flows along the magnetic field. Therefore, for these slits we first use a curve fit to remove the smoothly varying contribution due to the parallel flows, then fit the oscillation with Eq. (6.1). The oscillation periods measured near the footpoints are still consistent with that at the apex, albeit the damping time at these places may not be reliable.

In addition to the measurement of the oscillation parameters, the identification of the corresponding wave mode is equally important. In the synthetic EUV images the loop oscillates primarily in the transverse direction without any visible stationary node along the loop. This implies that the oscillation is very likely to be a fundamental kink mode. The phase difference of the velocity disturbance measured at different positions along the loop is helpful to strengthen this point, because for a fundamental kink mode, the phase difference should vanish.

To estimate the phase difference, we use the cross correlations of the oscillation, i.e. the best fitting function to the average Doppler velocity, at five positions to that at the apex (Fig. 6.4). The time-lag is between -100 and $+100$ s, which is sufficiently larger than the oscillation period. In Fig. 6.4 it is clear that all cross correlation functions peak at about zero time-lag. This confirms that the oscillations at different positions have no

phase difference. Moreover, the peak values of the correlations are close to unity, which also confirms that the oscillations are very similar at different positions.

The missing phase difference in the normal velocity disturbances at different positions of the loop also confirms that the loop oscillates as a whole. From the animation associated to Fig. 6.1, we find that oscillation behaves like a kink model oscillation, and the footpoints appear to be the nodes of oscillation¹. These "observational" properties suggest that the oscillation is a fundamental kink mode oscillation.

6.3 Estimate of the magnetic field strength

As derived by Edwin and Roberts (1983) the phase speed of the kink mode (c_k) in a slender magnetic flux tube with uniform density is related to the internal and external Alfvén speed (v_{Ai} and v_{Ae}) by

$$c_k = \left(\frac{\rho_i v_{Ai}^2 + \rho_e v_{Ae}^2}{\rho_i + \rho_e} \right)^{1/2}, \quad (6.2)$$

where ρ is density, and subscripts i and e refer to internal and external, respectively. In observations of coronal loop oscillations it is a common practice to estimate c_k as

$$c_k^{\text{obs}} = \frac{2L}{P}, \quad (6.3)$$

where L is the loop length and P the oscillation period (e.g Nakariakov et al. 1999).

By further assuming that the internal and external magnetic field of the loop are about equal and applying the effective Alfvén speed in Eq. (6.2), we obtain

$$c_k = \frac{|B|}{\sqrt{\mu_0 \rho_i}} \left(\frac{2}{1 + \rho_e/\rho_i} \right)^{1/2} \left(\frac{f_{Ai} + f_{Ae}}{2} \right)^{1/2}. \quad (6.4)$$

To derive plasma properties for the magnetic field estimate, we choose a group of magnetic fieldlines within the cross section of the oscillating loop for the internal properties and another group of magnetic fieldlines in the ambient corona outside the cross section of the loop for the external properties. We extract the density and temperature along the magnetic fieldlines, and get the average profiles for each group of magnetic fieldlines, respectively. In Fig. 6.5 (a), we plot the number density and temperature profiles along the loop, as well as those outside the oscillating loop.

Because most of the theoretical models and observations only consider the coronal part of the loop, we drop the cool part for this study. We define this as the part where the temperature is below 1 MK, which is marked in Fig. 6.5 by the gray background. It is clear in Fig. 6.5 that the temperature and density profiles in the coronal part are flat. This is also expected in the real corona, because of the highly efficient heat conduction and the large density scale height at such high temperatures.

¹The amplitude of the normal velocity disturbance along the loop would make this statement more solid (Yuan, D., private communication). However, such information is often not available in real observations. Here, we intent to focus on the information that is available in typical observations

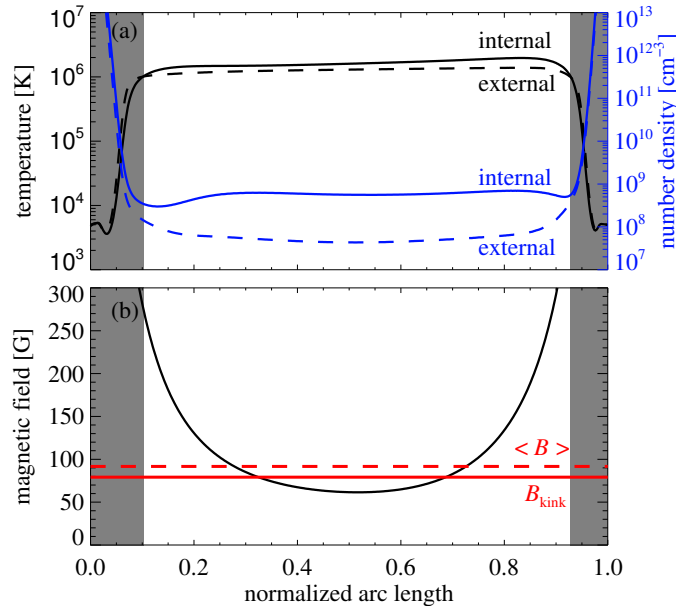


Figure 6.5: Plasma parameters and magnetic field strength along the loop as functions of normalized arc length. (a): Solid lines show the temperature (black) and number density (blue) in the oscillating coronal loop (i.e. internal). Dashed lines show the temperature (black) and number density (blue) in the ambient corona (i.e. external). (b): the magnetic field strength along the loop. The red solid line indicates the derived coronal magnetic field strength, B_{kink} , and the red dashed line the average magnetic field strength, $\langle B \rangle$ defined by Eq. (6.5). The position along the loop is normalized by the total loop length (53 Mm). The position 0.0 and 1.0 are the two footpoints at the photosphere. The grey areas are the lower atmosphere, where $T < 1$ MK. The loop length in the coronal part of the loop is about 45 Mm. See Sect. 6.2.3.

We calculate the average density in the coronal part inside and outside the loop, and obtain $\rho_i = 3.8 \times 10^{-12} \text{ kg m}^{-3}$ ($n_i = 5.7 \times 10^8 \text{ cm}^{-3}$) and $\rho_e = 4.4 \times 10^{-13} \text{ kg m}^{-3}$ ($n_e = 6.5 \times 10^7 \text{ cm}^{-3}$). Therefore the density ratio (ρ_e/ρ_i) is about 0.12, which is similar to the typical assumptions applied for tube models and for the inversion of observations (e.g. 0.1 by Nakariakov and Ofman 2001). The loop length in the coronal part is roughly 45 Mm. Together with the oscillation period from the fitting (Sect. 6.2.3), we obtain $c_k^{\text{obs}} = 1730 \text{ km s}^{-1}$ from Eq. (6.3). Finally a coronal magnetic field strength of $B_{\text{kink}} = 79 \text{ G}$ is estimated from Eq. (6.4).

6.4 Comparison with the actual magnetic field strength

The magnetic field strength varies along the coronal loop in both the real corona and our numerical model. Therefore, the value deduced from coronal seismology does not necessarily represent the field strength at any particular position of the loop, but is an average through the coronal part of the loop. The profile of the magnetic field strength along the loop in our model is plotted in Fig. 6.5 (b).

The arithmetic mean of the magnetic field strength along the loop is 120 G. However, this mean value does not provide much physical meaning. The reason is that coronal seismology estimates the magnetic field strength from the observed average wave speed defined as Eq. (6.3), and the actual wave speed is (usually) not a constant through the loop. Therefore the derived magnetic field strength is an average related to local wave speed (or say, wave travel time).

Aschwanden and Schrijver (2011) defined

$$\langle B \rangle = L \left[\int_0^L \frac{ds}{B(s)} \right]^{-1}, \quad (6.5)$$

where s is the coordinate along the arc of the loop. This definition corresponds to a flux tube with a uniform field strength that has the same oscillation period. In our model, $\langle B \rangle$ is 92 G, as indicated by the red dashed line in Fig. 6.5 (b). The arithmetic mean is clearly larger than $\langle B \rangle$, because the upper part of the loop, where the local magnetic field is weaker (i.e. lower local wave speed and larger local wave travel time), contributes more to $\langle B \rangle$ than the lower part of the loop does. On the other hand, $\langle B \rangle$ shows a much better match with B_{kink} . This is in line with the concept that the magnetic field strength estimated by coronal seismology represent the average magnetic field related to the average wave speed.

The magnetic field strength inverted from the loop oscillation, B_{kink} , is still 14% smaller than $\langle B \rangle$, which implies that the actual wave speed is slightly underestimated from the theoretical value. The complexities of actual coronal loops (as well as the loop in our model) could lead to such a deviation. One possible explanation might be the aspect ratio (i.e. width/length) of the loop. For the loop analysed in this paper, the aspect ratio of 0.045 is about three times larger than typical observations for long loops (e.g. taking a loop width of 2 Mm and a loop length of about 150 Mm). Edwin and Roberts (1983) noted that the actual kink mode speed is equal to c_k defined by Eq. (6.2) only when the width of the flux tube is significantly smaller than the wavelength of the disturbance. Otherwise, it decreases with an increasing aspect ratio, which is in line with the trend found in our model.

6.5 Discussion and summary

In this paper we present the loop oscillation found in a realistic coronal model driven by magnetic flux emergence through the photosphere (i.e. the bottom boundary). The treatment of the energy balance in the model allows us to produce a synthetic spectroscopic observation, in which the transverse loop oscillation can be clearly observed. The oscillation is further identified as the fundamental fast kink mode. The oscillation patterns found in the EUV corona synthesised from our 3D MHD model can be used for a direct comparison to the parameters of the oscillations seen in the solar observations. In contrast to the Sun, in our model we can directly check the plasma parameters and the magnetic field strength in the oscillating loop.

Damping is commonly found in transverse loop oscillations. The damping time is particularly important, because it reflects the rate at which the wave energy is converted into another form. Using a scaling relation derived from numerical models, Nakariakov et al.

(1999) found that the magnetic Reynold number deduced from the observed damping time may be about nine orders of magnitude smaller than the classical value (e.g. 10^{14}). Ofman and Aschwanden (2002) analysed the scaling relation of damping time to loop parameters and estimated an anomalous large viscosity of $10^{9.2\pm 3.5} \text{ m}^2 \text{ s}^{-1}$, which yields a Reynolds number at least five orders of magnitude smaller than the classical value. These results imply that the wave energy could be converted into heat much more efficiently. However, Goossens et al. (2002) showed that the observed fast damping of transverse loop oscillations can be explained by the damping of quasi-mode kink oscillations, whose rate is independent of the dissipation. Thus, they suggested that there is no need for the anomalously large viscosity.

More recently Verwichte et al. (2013b) analysed 52 observed loop oscillations and found that the damping time is related to the oscillation period by $\tau = \alpha P^\gamma$, where $\log_{10}\alpha = 0.44 \pm 0.31$ and $\gamma = 0.94 \pm 0.12$. The period ($T = 52.5 \text{ s}$) and damping time ($\tau = 125 \text{ s}$) of the oscillation in our model fit this scaling relation very well. It may suggest that the loop oscillation and its damping resemble the actual observations to some extent. The viscosity and resistivity in our typical models is of the order of $10^{10} \text{ m}^2 \text{ s}^{-1}$ (Bingert and Peter 2011), which is essentially determined by the grid spacing in the numerical models (in the present study we use $5 \times 10^9 \text{ m}^2 \text{ s}^{-1}$). This value happens to be in line with range found by Ofman and Aschwanden (2002) in a sample of 11 observed loop oscillations. The earlier study of one single case by Nakariakov et al. (1999) gave a value in the lower end of the range given by Ofman and Aschwanden (2002). From this we conclude that the value of the diffusivity in our model ($10^{9.7} \text{ m}^2 \text{ s}^{-1}$) is consistent with the average from observations ($10^{9.2} \text{ m}^2 \text{ s}^{-1}$) looking at a wide range of oscillation loops. If we take the loop half width ($w \approx 1 \text{ Mm}$) as the length scale, the dissipation time would be about 100 s, which is close to the damping of the oscillation in our model. It implies that in our model the dissipation is the dominant damping agent for the oscillation.

We apply the coronal seismology method to the observations synthesised from our model corona in the same way as done for observations. From this we obtain an average magnetic field strength of $B_{\text{kink}} = 79 \text{ G}$. The actual magnetic field strength in the model varies significantly through the loop. The value at the coronal base is about five times larger than that at the loop apex and B_{kink} is more close to the latter one. Furthermore we find B_{kink} to be about 14% smaller than the average magnetic field, which would give an identical total wave travel time through the loop (Aschwanden and Schrijver 2011). This may be due to the complexity of the coronal loop. We conclude that the magnetic field strength deduced by coronal seismology can be a good representative of that in the upper part of a coronal loop, while the magnetic field strength varies significantly along the loop, in our model and most probably also on the real Sun.

7 Summary and outlook

In this work we present a realistic coronal model that is driven by magnetic flux emergence at the bottom boundary. The modelling strategy of the coronal model is based on a series of numerical experiments (Gudiksen and Nordlund 2002, 2005a,b, Bingert and Peter 2011, Bourdin et al. 2013) that accounts for the optically thin radiation, highly anisotropic heat conduction, and heating by the Ohmic dissipation of the currents induced in the corona by the braiding of magnetic fieldlines in the photosphere. To drive the coronal model with magnetic flux emergence, we use the output from a realistic MHD simulation, which properly solves the radiative transfer and considers a realistic equation of state in the solar photosphere. Such simulations can resemble observed photospheric plasma and magnetic features very well. The output of the flux emergence simulation, which describes a fully self-consistent evolution of the plasma properties, velocity and magnetic field, can be considered as the data from an actual observation if such observations could be done.

The proper treatment on the energy balance in the coronal simulation allows us to synthesise coronal EUV emission from the density and temperature in the model. We find that loop-like EUV structures similar to real coronal EUV loops become visible during the formation of strong magnetic flux concentrations through the coalescence of small-scale magnetic elements in the photosphere.

The analysis of the energy input to the corona shows that the coronal loops are formed at places where enhanced upward Poynting flux is produced by the interaction of the flows and the magnetic structures in the photosphere (in the form of coalescent flows moving into the forming sunspot), as proposed by the fieldline braiding (Parker 1983) or flux-tube tectonics (Priest et al. 2002) mechanisms. The energy flux provides the free magnetic energy that can heat the coronal plasma through the Ohmic dissipation.

When the Ohmic heating is increased in the corona, the heat conduction transports the energy deposited in the corona along the magnetic fieldline to the dense lower atmosphere, i.e. the footpoint of the magnetic fieldline. Consequently, the pressure at the footpoint increases and drives an evaporation flow that takes hot plasma into the corona. This gives rise to the a coronal loop that is bright in EUV observation. The scenario is consistent with the results in traditional 1D loop models with a prescribed heating rate.

In the vertical plane in the middle of the simulation domain we find that neither temperature structure nor the density structure is co-spatial with the EUV structure (e.g. the cross section of the EUV loop), because the EUV loop is a convolution of the local plasma density and temperature. And the cross section of the EUV loop can change in a time scale of minutes according to the variations of the density and temperature. The investigation on the cross section profile of EUV loops is essentially beyond the ability of traditional 1D models, and can only be done in multi-dimensional models.

In the model we are able to deepen our understanding on the relation of EUV loops to magnetic fieldlines by following their evolution. In each snapshot of the model coronal, the EUV loops are nicely in line with the magnetic fieldlines. This is consistent with the relation that is commonly expected (c.f. Sect. 2.3) and is supported by observations (Feng et al. 2007). However, the evolution of the EUV loops and the magnetic fieldlines could be different in an emergence active region. When the magnetic fieldlines continuously emerge and expand upward, the apparent EUV structure (i.e. the EUV loop) remains roughly at the same height.

We find a hot spot, which is a small area of enhanced energy input, at the outer edge of the sunspot. The footpoints of emerging magnetic fieldlines are advected into this hotspot consecutively by the coalescent flow into the sunspot. These fieldlines get heated one after another. As a result, each fieldline is bright in a certain EUV passband (e.g. the AIA 193 Å channel) for only a short period of time. Thus, the EUV loop seen at different moments in time is contributed by the plasma in different magnetic fieldlines. This creates an apparently static EUV structure, while the actual magnetic fieldlines are continuously expanding upward. This scenario suggests the importance of treating the magnetic field together with the plasma, particularly when the magnetic field is evolving significantly.

Moreover, we analysis the transverse loop oscillations in the model. The loop oscillation can be clearly identified and measured from the synthetic observation. This shows the power of realistic models on reproducing observational properties. We further estimate the (average) magnetic field strength from the oscillation parameters, employing the technique of coronal seismology that is extensively applied to observed loop oscillations. The deduce (average) magnetic field strength represents the field strength in the upper part of the corona loop, when the magnetic field strength varies along the loop as in the real corona. This helps us to better understand what the result means, when the this technique is applied to estimate the magnetic field strength in real coronal loops.

This work presents a series of investigations on the formation and evolution of the coronal plasma and magnetic field in an emerging active region, which are barely touched by previous models. It also highlights the strong power of realistic 3D simulations on the coronal modelling.

The coupling of two models both following the realistic modelling strategy makes one step forward to the comprehensive picture of the dynamical coupling of the solar atmosphere. As the next step, this work can be continued to further deepen our understanding of the corona dynamics.

Coronal dynamics driven by the emergence of twisted flux tube

In this work we use the emergence of a flux tube that has no imposed twist. This flux tube creates a magnetic field quiet symmetric in respect to the middle vertical plane of the domain. The most evident overall flow pattern in the photosphere is the coalescent flow pointing to the sunspots. While in observations, the asymmetry in the magnetic field topology is very common. Apparent rotation of the sunspots and shearing flows in the active region often give rise to the transverse magnetic field in between the sunspots. These features may be modelled by the emergence of a flux tube containing a certain amount of twist. Cheung et al. (2010) gave an example of the significant rotation of the forming sunspots, when a (an unrealistically) strongly twisted flux tube breaks into the

photosphere (see also Fig. 2.6).

A meaningful improvement to present model is to drive coronal simulations with the emergence of flux tubes that contain different amount of twist. This series of the models will be able to better represent the diverse situations on the Sun. The build-up of coronal features in response to the different photosphere dynamics can bring us more insights on the dynamical coupling between different layers in the solar atmosphere.

Detailed comparison between realistic models and observations

Modern high resolution and high time cadence imaging and spectroscopic observations help us to explore the solar corona in unprecedented detail. At the same time, the development in computing powers allows people to conduct realistic simulations that can be directly comparable to observations of the corona. In this work we have shown that the general features in the synthetic observations are well in line with actual observations. A more comprehensive comparison between the model and observations can better exploit the power of realistic models.

A comprehensive comparison would list as many as possible fundamental observational characteristics of the corona, and compare them with the corresponding model synthetics. If the model could reproduce a particular observational feature, this gives us an opportunity to reveal the physical process underlying the appearance. When the model fails to reproduce a certain feature, it leads to the question of what is missing in the model. It may be that a particular model setup is not appropriate for the comparison with this observational property, or the fundamental physics responsible for this feature is missing. Then this can at least provide us a hint on what needs to be improved in the model. In this way, these comparisons would help us to review where we are standing and which direction we should head to.

Bibliography

- Abbett, W. P.: 2007, *ApJ* **665**, 1469
- Abbett, W. P. and Fisher, G. H.: 2003, *ApJ* **582**, 475
- Alfvén, H.: 1941, *Arkiv för Matematik, Astronomi och Fysik (Band 27A)* **25**, 1
- Archontis, V., Moreno-Insertis, F., Galsgaard, K., Hood, A., and O’Shea, E.: 2004, *A&A* **426**, 1047
- Arregui, I., Terradas, J., Oliver, R., and Ballester, J. L.: 2007, *A&A* **466**, 1145
- Aschwanden, M. J.: 2004, *Physics of the Solar Corona. An Introduction*, Praxis Publishing Ltd
- Aschwanden, M. J., Fletcher, L., Schrijver, C. J., and Alexander, D.: 1999, *ApJ* **520**, 880
- Aschwanden, M. J. and Schrijver, C. J.: 2011, *ApJ* **736**, 102
- Aschwanden, M. J., Wülser, J.-P., Nitta, N. V., and Lemen, J. R.: 2008, *ApJ* **679**, 827
- Banerjee, D., Erdélyi, R., Oliver, R., and O’Shea, E.: 2007, *Sol. Phys.* **246**, 3
- Bingert, S. and Peter, H.: 2011, *A&A* **530**, A112
- Bingert, S. and Peter, H.: 2013, *A&A* **550**, A30
- Boerner, P., Edwards, C., Lemen, J., Rausch, A., Schrijver, C., Shine, R., Shing, L., Stern, R., Tarbell, T., Title, A., Wolfson, C. J., Soufli, R., Spiller, E., Gullikson, E., McKenzie, D., Windt, D., Golub, L., Podgorski, W., Testa, P., and Weber, M.: 2012, *Sol. Phys.* **275**, 41
- Boris, J. P. and Mariska, J. T.: 1982, *ApJ* **258**, L49
- Bourdin, P.-A., Bingert, S., and Peter, H.: 2013, *A&A* **555**, A123
- Brandenburg, A., Kemel, K., Kleeorin, N., and Rogachevskii, I.: 2012, *ApJ* **749**, 179
- Bray, R. J., Cram, L. E., Durrant, C., and Loughhead, R. E.: 1991, *Plasma Loops in the Solar Corona*, Cambridge University Press
- Chen, F., Peter, H., Bingert, S., and Cheung, M. C. M.: 2014, *A&A* **564**, A12
- Cheung, M. C. M. and DeRosa, M. L.: 2012, *ApJ* **757**, 147

- Cheung, M. C. M. and Isobe, H.: 2014, *Living Reviews in Solar Physics* **11**, 3
- Cheung, M. C. M., Rempel, M., Title, A. M., and Schüssler, M.: 2010, *ApJ* **720**, 233
- Cirtain, J. W., Golub, L., Winebarger, A. R., de Pontieu, B., Kobayashi, K., Moore, R. L., Walsh, R. W., Korreck, K. E., Weber, M., McCauley, P., Title, A., Kuzin, S., and Deforest, C. E.: 2013, *Nature* **493**, 501
- Cook, J. W., Cheng, C.-C., Jacobs, V. L., and Antiochos, S. K.: 1989, *ApJ* **338**, 1176
- De Moortel, I., Ireland, J., and Walsh, R. W.: 2000, *A&A* **355**, L23
- De Moortel, I. and Nakariakov, V. M.: 2012, *Royal Society of London Philosophical Transactions Series A* **370**, 3193
- De Moortel, I. and Pascoe, D. J.: 2009, *ApJ* **699**, L72
- De Pontieu, B., McIntosh, S. W., Carlsson, M., Hansteen, V. H., Tarbell, T. D., Boerner, P., Martinez-Sykora, J., Schrijver, C. J., and Title, A. M.: 2011, *Science* **331**, 55
- De Rosa, M. L., Schrijver, C. J., Barnes, G., Leka, K. D., Lites, B. W., Aschwanden, M. J., Amari, T., Canou, A., McTiernan, J. M., Régnier, S., Thalmann, J. K., Valori, G., Wheatland, M. S., Wiegmann, T., Cheung, M. C. M., Conlon, P. A., Fuhrmann, M., Inhester, B., and Tadesse, T.: 2009, *ApJ* **696**, 1780
- Doschek, G. A., Warren, H. P., Mariska, J. T., Muglach, K., Culhane, J. L., Hara, H., and Watanabe, T.: 2008, *ApJ* **686**, 1362
- Edlén, B.: 1943, *Zeitschrift für Astrophysik* **22**, 30
- Edwin, P. M. and Roberts, B.: 1983, *Sol. Phys.* **88**, 179
- Erdélyi, R. and Taroyan, Y.: 2008, *A&A* **489**, L49
- Erdélyi, R. and Verth, G.: 2007, *A&A* **462**, 743
- Fan, Y.: 2001, *ApJ* **554**, L111
- Fan, Y.: 2009, *Living Reviews in Solar Physics* **6**, 4
- Fang, F., Manchester, W., Abnett, W. P., and van der Holst, B.: 2010, *ApJ* **714**, 1649
- Fang, F., Manchester, IV, W., Abnett, W. P., and van der Holst, B.: 2012, *ApJ* **745**, 37
- Feng, L., Inhester, B., Solanki, S. K., Wiegmann, T., Podlipnik, B., Howard, R. A., and Wuelser, J.-P.: 2007, *ApJ* **671**, L205
- Forbes, T. G. and Acton, L. W.: 1996, *ApJ* **459**, 330
- Galsgaard, K. and Nordlund, Å.: 1996, *J. Geophys. Res.* **101**, 13445
- Golub, L., Deluca, E., Austin, G., et al.: 2007, *Sol. Phys.* **243**, 63

- Goossens, M., Andries, J., and Aschwanden, M. J.: 2002, *A&A* **394**, L39
- Goossens, M., Terradas, J., Andries, J., Arregui, I., and Ballester, J. L.: 2009, *A&A* **503**, 213
- Grotian, W.: 1939, *Naturwissenschaften* **27**, 214
- Gudiksen, B. V., Carlsson, M., Hansteen, V. H., Hayek, W., Leenaarts, J., and Martínez-Sykora, J.: 2011, *A&A* **531**, A154
- Gudiksen, B. V. and Nordlund, Å.: 2002, *ApJ* **572**, L113
- Gudiksen, B. V. and Nordlund, Å.: 2005a, *ApJ* **618**, 1020
- Gudiksen, B. V. and Nordlund, Å.: 2005b, *ApJ* **618**, 1031
- Guo, Y., Erdélyi, R., Srivastava, A. K., Hao, Q., Cheng, X., Chen, P. F., Ding, M. D., and Dwivedi, B. N.: 2015, *ApJ* **799**, 151
- Hansteen, V. H.: 1993, *ApJ* **402**, 741
- Hansteen, V. H., Hara, H., De Pontieu, B., and Carlsson, M.: 2010, *ApJ* **718**, 1070
- Heinemann, T., Nordlund, Å., Scharmer, G. B., and Spruit, H. C.: 2007, *ApJ* **669**, 1390
- Hendrix, D. L., van Hoven, G., Mikic, Z., and Schnack, D. D.: 1996, *ApJ* **470**, 1192
- Heyvaerts, J. and Priest, E. R.: 1983, *A&A* **117**, 220
- Hurlburt, N. E., Alexander, D., and Rucklidge, A. M.: 2002, *ApJ* **577**, 993
- Ionson, J. A.: 1978, *ApJ* **226**, 650
- Kleorin, N. and Rogachevskii, I.: 1994, *Phys. Rev. E* **50**, 2716
- Klimchuk, J. A.: 2006, *Sol. Phys.* **234**, 41
- Lemen, J., Title, A. M., Akin, D. J., et al.: 2012, *Sol. Phys.* **275**, 14
- Lionello, R., Winebarger, A. R., Mok, Y., Linker, J. A., and Mikić, Z.: 2013, *ApJ* **773**, 134
- López Fuentes, M. C. and Klimchuk, J. A.: 2010, *ApJ* **719**, 591
- Magara, T.: 2006, *ApJ* **653**, 1499
- Malanushenko, A. and Schrijver, C. J.: 2013, *ApJ* **775**, 120
- Malanushenko, A., Schrijver, C. J., DeRosa, M. L., and Wheatland, M. S.: 2014, *ApJ* **783**, 102
- Manchester, IV, W., Gombosi, T., DeZeeuw, D., and Fan, Y.: 2004, *ApJ* **610**, 588
- Mariska, J. T.: 1987, *ApJ* **319**, 465

- Mariska, J. T.: 1992, *The solar transition region*, Cambridge Univ. Press, Cambridge
- Mariska, J. T. and Boris, J. P.: 1983, *ApJ* **267**, 409
- Mariska, J. T., Boris, J. P., Oran, E. S., Young, T. R., and Doschek, G. A.: 1982, *ApJ* **255**, 783
- Mariska, J. T. and Muglach, K.: 2010, *ApJ* **713**, 573
- Martens, P. C. H. and Kuin, N. P. M.: 1983, *A&A* **123**, 216
- Martínez-Sykora, J., Hansteen, V., and Carlsson, M.: 2008, *ApJ* **679**, 871
- Martínez-Sykora, J., Hansteen, V., and Carlsson, M.: 2009, *ApJ* **702**, 129
- Meyer, C. D., Balsara, D. S., and Aslam, T. D.: 2012, *MNRAS* **422**, 2102
- Mikić, Z., Lionello, R., Mok, Y., Linker, J. A., and Winebarger, A. R.: 2013, *ApJ* **773**, 94
- Mok, Y., Mikić, Z., Lionello, R., and Linker, J. A.: 2008, *ApJ* **679**, L161
- Müller, D. A. N., Hansteen, V. H., and Peter, H.: 2003, *A&A* **411**, 605
- Müller, D. A. N., Peter, H., and Hansteen, V. H.: 2004, *A&A* **424**, 289
- Nakariakov, V. M. and Ofman, L.: 2001, *A&A* **372**, L53
- Nakariakov, V. M., Ofman, L., Deluca, E. E., Roberts, B., and Davila, J. M.: 1999, *Science* **285**, 862
- Nakariakov, V. M. and Verwichte, E.: 2005, *Living Reviews in Solar Physics* **2**, 3
- Ofman, L. and Aschwanden, M. J.: 2002, *ApJ* **576**, L153
- Ofman, L. and Wang, T.: 2002, *ApJ* **580**, L85
- Ofman, L. and Wang, T. J.: 2008, *A&A* **482**, L9
- Parker, E. N.: 1972, *ApJ* **174**, 499
- Parker, E. N.: 1983, *ApJ* **264**, 642
- Parker, E. N.: 1988, *ApJ* **330**, 474
- Pascoe, D. J., de Moortel, I., and McLaughlin, J. A.: 2009, *A&A* **505**, 319
- Peter, H.: 1999, *ApJ* **516**, 490
- Peter, H., Abbo, L., Andretta, V., Auchère, F., Bemporad, A., Berrilli, F., Bommier, V., Braukhane, A., Casini, R., Curdt, W., Davila, J., Dittus, H., Fineschi, S., Fludra, A., Gandorfer, A., Griffin, D., Inhester, B., Lagg, A., Degl'Innocenti, E. L., Maiwald, V., Sainz, R. M., Pillet, V. M., Matthews, S., Moses, D., Parenti, S., Pietarila, A., Quantius, D., Raouafi, N.-E., Raymond, J., Rochus, P., Romberg, O., Schlotterer, M., Schühle, U., Solanki, S., Spadaro, D., Teriaca, L., Tomczyk, S., Bueno, J. T., and Vial, J.-C.: 2012, *Experimental Astronomy* **33**, 271

- Peter, H. and Bingert, S.: 2012, *A&A* **548**, A1
- Peter, H. and Dwivedi, B. N.: 2014, *Frontiers Astron. Space Sci.* **1**, 2
- Peter, H., Gudiksen, B. V., and Nordlund, Å.: 2004, *ApJ* **617**, L85
- Peter, H., Gudiksen, B. V., and Nordlund, Å.: 2006, *ApJ* **638**, 1086
- Peter, H. and Judge, P. G.: 1999, *ApJ* **522**, 1148
- Priest, E.: 2014, *Magnetohydrodynamics of the Sun*, Cambridge University Press
- Priest, E. R., Heyvaerts, J. F., and Title, A. M.: 2002, *ApJ* **576**, 533
- Rappazzo, A. F., Velli, M., Einaudi, G., and Dahlburg, R. B.: 2008, *ApJ* **677**, 1348
- Reale, F.: 2010, *Living Reviews in Solar Physics* **7**, 5
- Reale, F.: 2014, *Living Reviews in Solar Physics* **11**, 4
- Rempel, M. and Cheung, M. C. M.: 2014, *ArXiv e-prints*
- Rempel, M., Schüssler, M., Cameron, R. H., and Knölker, M.: 2009a, *Science* **325**, 171
- Rempel, M., Schüssler, M., and Knölker, M.: 2009b, *ApJ* **691**, 640
- Roberts, B., Edwin, P. M., and Benz, A. O.: 1984, *ApJ* **279**, 857
- Rosner, R., Tucker, W. H., and Vaiana, G. S.: 1978, *ApJ* **220**, 643
- Ruderman, M. S. and Erdélyi, R.: 2009, *Space Sci. Rev.* **149**, 199
- Schrijver, C. J., De Rosa, M. L., Metcalf, T. R., Liu, Y., McTiernan, J., Régnier, S., Valori, G., Wheatland, M. S., and Wiegmann, T.: 2006, *Sol. Phys.* **235**, 161
- Schrijver, C. J. and Zwaan, C.: 2000, *Solar and Stellar Magnetic Activity*, Cambridge University Press
- Selwa, M., Ofman, L., and Solanki, S. K.: 2011, *ApJ* **726**, 42
- Spadaro, D., Lanza, A. F., Karpen, J. T., and Antiochos, S. K.: 2006, *ApJ* **642**, 579
- Spitzer, L.: 1962, *Physics of Fully Ionized Gases*, Interscience, New York (2nd edition)
- Strauss, H. R.: 1976, *Physics of Fluids* **19**, 134
- Tian, H., McIntosh, S. W., Wang, T., Ofman, L., De Pontieu, B., Innes, D. E., and Peter, H.: 2012, *ApJ* **759**, 144
- Tomczyk, S., McIntosh, S. W., Keil, S. L., Judge, P. G., Schad, T., Seeley, D. H., and Edmondson, J.: 2007, *Science* **317**, 1192
- Uchida, Y.: 1970, *PASJ* **22**, 341

- van Ballegooijen, A. A.: 1986, *ApJ* **311**, 1001
- van Ballegooijen, A. A., Asgari-Targhi, M., and Berger, M. A.: 2014, *ApJ* **787**, 87
- van Ballegooijen, A. A., Asgari-Targhi, M., Cranmer, S. R., and DeLuca, E. E.: 2011, *ApJ* **736**, 3
- Van Doorselaere, T., Debosscher, A., Andries, J., and Poedts, S.: 2004, *A&A* **424**, 1065
- Van Doorselaere, T., Nakariakov, V. M., Young, P. R., and Verwichte, E.: 2008, *A&A* **487**, L17
- van Wettum, T., Bingert, S., and Peter, H.: 2013, *A&A* **554**, A39
- Vernazza, J. E., Avrett, E. H., and Loeser, R.: 1981, *ApJS* **45**, 635
- Verwichte, E., Foullon, C., and Nakariakov, V. M.: 2006, *A&A* **452**, 615
- Verwichte, E., Van Doorselaere, T., Foullon, C., and White, R. S.: 2013a, *ApJ* **767**, 16
- Verwichte, E., Van Doorselaere, T., White, R. S., and Antolin, P.: 2013b, *A&A* **552**, A138
- Vögler, A., Shelyag, S., Schüssler, M., Cattaneo, F., Emonet, T., and Linde, T.: 2005, *A&A* **429**, 335
- Wang, T.: 2011, *Space Sci. Rev.* **158**, 397
- Wang, T., Innes, D. E., and Qiu, J.: 2007, *ApJ* **656**, 598
- Wang, T. J., Ofman, L., and Davila, J. M.: 2009, *ApJ* **696**, 1448
- Wang, T. J., Solanki, S. K., Curdt, W., Innes, D. E., Dammasch, I. E., and Kliem, B.: 2003, *A&A* **406**, 1105
- Warnecke, J., Losada, I. R., Brandenburg, A., Kleeorin, N., and Rogachevskii, I.: 2013, *ApJ* **777**, L37
- Wiegmann, T. and Sakurai, T.: 2012, *Living Reviews in Solar Physics* **9**, 5
- Williamson, J. H.: 1980, *Journal of Computational Physics* **35**, 48
- Withbroe, G. L. and Noyes, R. W.: 1977, *ARA&A* **15**, 363
- Yang, W. H., Sturrock, P. A., and Antiochos, S. K.: 1986, *ApJ* **309**, 383
- Yuan, D. and Nakariakov, V. M.: 2012, *A&A* **543**, A9

Acknowledgements

My sincere thanks to

- my supervisor Prof. Dr. Hardi Peter for the encouragement and advices on my research, as well as the other countless helps through these years
- my advisor committee, Prof. Dr. Manfred Schüssler and Prof. Dr. Ansgar Reiners, who always kindly arrange time for my requests on discussions and meetings
- Dr. Robert Cameron for always sharing his talent and sense of humour with us, and Dr. Mark Cheung for many helps throughout my doctoral study
- the coronal dynamics team members: Dr. Sven Bingert, Dr. Philippe Bourdin, Dr. Tijmen van Wettum, Dr. Jörn Warnecke, Mr. Krzysztof Barczynski
- Jörn for many helpful comments on the thesis, and Dr. Nai-Hwa Chen, Dr. Li Feng, Dr. Lijia Guo for reading part of the thesis and "Tu Cao" (informal Chinese for "commenting"), and Dr. Leping Li for very productive discussions in the lunch queue.
- Prof. Dr. Mingde Ding, Prof. Dr. Pengfei Chen, and Prof. Dr. Cheng Fang in Nanjing University for the generous support on my visits to Nanjing and many constructive discussions
- folks in the IMPRS who always make the school active, and the coordinators, Dr. Dieter Schmitt and Dr. Sonja Schuh for their great efforts to keep the school well organised.
- the Chinese community at MPS for all the fun in our get-togethers
- Dr. Siyi Feng, Mr. Ruoyu Liu, Mr. Shiwei Wu at MPIA (Heidelberg), Mr. Shi Shao at MPA (Garching) and my friends in the US for kindly treating me during my visit
- my parents and parents-in-law for their support and encouragement.

Thanks for Nanjing and Göttingen
that bring me my wife,
Heng Cui,
who is the light of my life.

Publications

Articles published in peer-reviewed journals that are included in this thesis

- **F. Chen** and H. Peter, *Using coronal seismology to estimate the magnetic field strength in a realistic coronal model*, 2015 A&A, 581, A137
- **F. Chen**, H. Peter, S. Bingert, and M. C. M. Cheung, *Magnetic jam in the solar corona*, 2015 Nature Physics, 11, 492
- **F. Chen**, H. Peter, S. Bingert, and M. C. M. Cheung, *A model for the formation of the active region corona driven by magnetic flux emergence*, 2014 A&A, 564, A12

Contributions in peer-reviewed articles that are not included in this thesis

- L. M. Yan, H. Peter, J. S. He, H. Tian, L. D. Xia, L. H. Wang, C. Y. Tu, L. Zhang, **F. Chen**, K. Barczynski, *Self-absorption in the solar transition region*, 2015 ApJ, 811, 48
- M. C. M. Cheung, P. Boerner, C. J. Schrijver, P. Testa, **F. Chen**, H. Peter, and A. Malanushenko, *Thermal Diagnostics with SDO/AIA: A Validated Method for DEMs*, 2015 ApJ, 807, 143
- J. Zhang, B. Zhang, T. Li, S. H. Yang, Y. Z. Zhang, L. P. Li, **F. Chen**, and H. Peter, *Coronal heating by the interaction between emerging active regions and the quiet Sun observed by SDO*, 2015 ApJL, 799, L27
- L. P. Li, H. Peter, **F. Chen**, and J. Zhang, *Conversion from mutual helicity to self-helicity observed with IRIS*, 2014 A&A, 570, A93

Curriculum vitae

Name : Feng Chen
Date of birth : 29.06.1986
Place of birth : Shandong, China
Date of Marriage : 11.08.2014
Spouse : Heng Cui
Nationality : Chinese

Education

09/2002 – 06/2005 High School Affiliated to Shandong Normal University, Jinan

09/2005 – 06/2009 Bachelor of Science
Department of Astronomy, Nanjing University, Nanjing

09/2009 – 12/2011 Master of Science
Department of Astronomy, Nanjing University, Nanjing
Thesis title : *Spectroscopic analysis
of coronal extreme ultraviolet waves*

02/2012 – 04/2015 Doctoral student
IMPRS at the University of Göttingen and
Max Planck Institute for Solar System Research, Göttingen